North Carolina Agricultural and Technical State University

## Aggie Digital Collections and Scholarship

2013

# Wind Climatology And Relations With Sst And Sea Ice In The Chukchi-Beaufort Seas Region

Steve T. Stegall
*North Carolina Agricultural and Technical State University*

Follow this and additional works at: https://digital.library.ncat.edu/dissertations

Wind Climatology and Relations with SST and Sea Ice in the Chukchi-Beaufort Seas Region

Steve T. Stegall

North Carolina A&T State University

A dissertation submitted to the graduate faculty

in partial fulfillment of the requirements for the degree of

DOCTOR OF PHILOSOPHY

Department: Energy and Environmental Systems

Major: Atmospheric Science

Major Professor: Dr. Jing Zhang

Greensboro, North Carolina

2013

The Graduate School
North Carolina Agricultural and Technical State University
This is to certify that the Doctoral Dissertation of


Steve T. Stegall



has met the dissertation requirements of
North Carolina Agricultural and Technical State University


Greensboro, North Carolina
2013


Approved by:



_____          _____

Dr. Jing Zhang                                   Dr. Xiangdong Zhang
Major Professor                                  Committee Member



_____          _____

Dr. Yuh-LangLin                                  Dr. Ademe Mekonnen
Committee Member                                 Committee Member



_____          _____

Dr. Keith Schimmel                               Dr. Yevginiy A. Rstigeyev
Department Chair                                  Committee Member



_____

Dr. Sanjiv Sarin
Dean, The Graduate School

Biographical Sketch

Steve T. Stegall

Steve T. Stegall was born on June 20th, 1976 in Denver Colorado. He spent most of his childhood in Lakewood, CO, a western suburb of Denver. A majority of the time was spent golfing, hiking, and bike riding. In 1994 he graduated from Alameda High School. In 1996 he started his undergraduate work at Metropolitan State College of Denver (MSCD) majoring in Meteorology. He was fortunate enough to work for the Environmental Protection Agency's National Enforcement Investigations Lab (NEIC). In the summer of 2003, he met and worked with Dr. Eric Betterton who would eventually become a mentor and recruited him to the University of Arizona. Steve T. Stegall graduated from MSCD in 2000 with his B.S. in Meteorology and a B.S. in Applied Math from MSCD in 2004. Also in 2004 he started his Master's of Science at the University of Arizona in Atmospheric Science. He was able to work with Dr. Xubin Zeng who is also a mentor to him. He graduated from the University of Arizona with his M.S in Atmospheric Science in 2006. He was given the opportunity to begin a Ph.D. on surface wind analysis/climatology at the University of Alaska Fairbanks (UAF) in Fairbanks AK in 2009 with Dr. Jing Zhang. In 2010, mainly due to budget cuts at UAF/ARSC a new opportunity for Jing, he was able to continue my Ph.D. at NC A & T. He was given an opportunity to continue his Ph.D. at North Carolina A & T State University (NC A & T) with his current advisor on the same project and make new friends. The summer of 2012, he met Amanda Leary and knew then and there she was the one. They have spent many days doing fun things like hiking, going to wineries, country drives, and going to the beach. In 2013 he got engaged to the love of his life Amanda Leary, and they plan to marry in 2014.

## Acknowledgements

I would like to acknowledge all those who have influenced me while working on this dissertation and Ph.D. and throughout my life. In particular to those that have helped me throughout my college and graduate school years. I could not have completed the dissertation and Ph.D. without your support.

First, I would like to thank my beautiful fiancé Amanda Leary and her family. The last year has been the best and you have been a huge support for me. I have had a wonderful time getting to know you and your family who have been very supportive. You have changed my life forever and for the best. It makes me very happy to spend the rest of my life with you and to be finishing my Ph.D. with you at my side! I love you very much my Lemon!

Secondly I would like to thank my parents. My mom, dad and Jim have been very supportive and loving all of my life. The camping trips with my mom and Jim were very fun especially when we were able to spend time at their property in southern Colorado. I see this very pretty real estate and my mom and Jim far to seldom. I also want to thank my childhood friends such as Tony, Buddy, my stepbrothers, and my cousin Luc. They made growing up lots of fun and very memorable.

In particular, I want to acknowledge my late dad, Tom Stegall. He passed away in 2007. I miss him dearly and not a single day goes by that I don't think of him. My dad was also one of my best friends. We played golf at least twice a week growing up. In fact most vacation time I had growing up we would play as much golf as possible. We always had wonderful conversations, especially about the weather and thunderstorms and if we would get any tornadoes or blizzards. He is and will always be greatly missed and I wish he could be here to celebrate my Ph.D.

references.  I also want to thank the many other professors I learned from at the University of

Arizona with the many Graduate classes I had the pleasure of taking.

I also want to thank Dr. Xubin Zeng as my advisor during my tenure at the University of

Arizona.  It was a privilege working with him.  I enjoyed his enthusiasm and passion for his

many research interests.  That passion and enthusiasm definitely rubbed off onto me and has

stayed with me to this day.  I really enjoyed our monthly group lunches and meetings.  He could

be tough with lots of questions when I would present at the group meetings but it really helped

me with my research and "thicken" my skin when it comes to tough questions and concern when

it comes to my research.  That constructive criticism made my research much better overall.  I

want to thank him for giving me positive references.

Next I want to thank the many friends I made at the University of Arizona.  Friends like

Alex, Israel, Jen, Mike, Stephen, and Matt among many others I had the pleasure of meeting

while at the University.  Alex, Mike, Israel, and Matt were roommates and made me feel like

being a part of a family, whether we were living in La Aldea or the nice house in Oro Valley.

Those were fun times and I don't think I would have survived Graduate school there without

them and I will remember it fondly.

I want to turn my acknowledgments to Dr. Jing Zhang who gave me an opportunity to

attend the University of Alaska Fairbanks to do my Ph.D. work.  At this time in my life I was

between jobs and really needed the opportunity.  I am very grateful that she me as an excellent

candidate to become a researcher.  I will always be grateful to Jing for giving me the opportunity

to do my Ph.D. work with her.

Fairbanks, Alaska was one of my favorite and unique times of my life.  Experiencing the

Interior Alaska climate is a challenge, but one that I absolutely loved.  The cold winters were

very special and enjoyable with cross-country skiing several days a week, especially in the -40F to -50F temperatures. My research in Alaska was very important to me, personally and professionally. I appreciate and will never forget the professors and lively scientific discussions we had during class.

In Alaska I made some great friends that are like family to me. I especially enjoyed the road trips I took with John Mayfield. Our trip north on the Dalton Highway was probably the best road trip I ever took. We got to see the Yukon River, the Brooks Range, and the Arctic Ocean as well as the North Slope and tons of wildlife. John also made doing research at UAF a pleasure and was there for me if I had questions or was just plain stressed out. Jeanne and Dan Talbot are also great friends and made my experience in Alaska unforgettable. Our game nights were especially wonderful. I also want to thank my very close friend Oceana Francis. I still miss our conversations and especially when they included Russian Standard Vodka! Watching your success at UAF and afterwards provides me with inspiration and I thank you for your support over the years with my work and especially with my Dad and my cousin Kimm. You're a great friend!

As can happen in life sometimes your stay at one place can be cut short. This happened with UAF. Due to budget cuts and the fact that Dr Jing Zhang my advisor accepted a professorship at North Carolina A & T State University I decided to transfer there to continue working with her. It was a tough choice considering that UAF is an outstanding university. However Jing took a chance on me when I needed it to start my Ph.D. so I felt I owed her loyalty to take a chance at transferring to a new school. Secondly, I really have enjoyed the research project and wanted to continue with it until the end and get my Ph.D. using this research.

Here at NC A & T I have enjoyed continuing my research and am thankful for the opportunity to meet and make new friends such as Cristina, Quentin, James, Galen, Gian, Jose, Adrian and others. I have also enjoyed taking more classes and learning from great professors such as Dr. Lin and others. I would also like to thank Dr. Xiangdong Zhang for very helpful scientific advice and feedback but also for funding through UAF this summer. I want to thank Jeremy Krieger, Fuhong Liu, and Wei Tao for help with figures and advise. I also want to thank my Ph.D. Committee Dr. Jing Zhang, Dr. Xiangdong Zhang, Dr. Lin, and Dr. Mekonnen for their input and scientific advice and input for this dissertation. I would also like to thank Dr. Keith Schimmel and the Energy and Environmental Systems Department and NOAA ISET for partial funding of this research.

I want to also mention family and friends that have been here for me and given me general support not mentioned above. I would like to thank my Aunt Annette and Uncle Jim Burkhalter, my Aunt and Uncle Sue and Rob Rainguet, my cousin Mikael Velutich, and Aunt Susan and Uncle Ed O'Conner.

I would also like to acknowledge that the Bureau of Ocean Energy Management, Regulation, and Enforcement (BOEMRE) (previous Minerals Management Service (MMS)) of the U.S. Department of the Interior under contract M06PC00018 also supported this work. The computing resources were provided by the Arctic Region Supercomputing Center at the University of Alaska Fairbanks. I appreciate Xiangdong Zhang for his insightful comments and fruitful discussions. Appreciation also goes to Jeremy Krieger and Martha Shulski for the observational data collection and quality control, and Wei Tao for helping with some figure plots.

Table of Contents

List of Figures

## List of Tables

Abstract

Wind is a fundamental parameter linking dynamical processes among different components of climate systems. This dissertation demonstrates researches describing climatological state, variability, long-term changes, and extremes of surface wind and associated surface properties for the Chukchi/Beaufort Seas and Alaskan North Slope region. Three different reanalysis datasets are used for this study, including the 3-hourly, 32-km resolution NARR reanalysis, 6-hourly, 0.75° X 0.75° lat/lon resolution ERA-Interim reanalysis, and a newly developed 1-hourly, 10-km CBHAR reanalysis. These three datasets capture similar seasonality of the region's surface winds with weak winds in spring and strong winds in autumn. NARR shows the strongest winds in October, while peak winds in CBHAR and ERA-I are in November. All three datasets show the greatest increasing trend of areal averaged monthly mean and $95^{th}$ percentile wind speeds in October. The anomalous mesoscale winds over mountains are all captured by the three datasets; however, CBHAR demonstrates the best capability in detailing the mesoscale features. Investigation of wind-SST-ice relations in the study area demonstrates a negative correlation between surface wind and SST over open water and less-ice covered areas and a positive correlation over more-ice covered areas. Synoptic-scale storm plays an important role in forming the correlative relation between wind-SST-sea ice. Warmer SST associated with strong winds over weak solar forcing areas is the result of enhanced longwave radiation brought by storms. Colder SST over relatively strong solar forcing areas where less ice is present is caused by strong cold air advection and reduced solar radiation due to storm clouds.

**CHAPTER 1**

**Introduction and Literature Review**

The Arctic region is one of two regions in the world that include land, sea, and sea ice. This region is subject to recent and projected climate changes, (ACIA 2005; Johannessen et al. 2004). The region has also been subject to dramatic sea ice loss (Jahn et al. 2012; Zhang and Walsh, 2006), especially is the last decade or so and are projected to continue to decreased sea ice extent (Stroeve et al. 2012; Wang and Overland, 2012). A major source of variance in the Arctic is the Arctic Oscillation, AO (Thompson and Wallace, 1998), which can be interpreted as the surface signature in strength of the polar vortex aloft in the stratosphere. However Zhang et al., (2008) document a major and rapid change in the last decade or so to a structure that varies more between the Eurasian Arctic and the North Pacific. These rapid changes can influence the wind field, influencing solar radiation and albedo-feedback, which can further explain dramatic sea ice loss. Further analysis of these changes with a specific focus on the surface wind field is needed. The changes in the wind field can also have an impact on other variables such as Ekman pumping and ocean circulation. Changes in sea level pressure (SLP) variability and trends have also been studied (Moore, 2013) which focused on the Beaufort Sea High. Studies however have been done of the overall characteristics of the Beaufort Sea region (Overland, 2009) and of the Beaufort Sea High (Serreze and Barrett, 2011). From Overland 2009, the SLP pattern indicates that the Beaufort high is strongest in winter and is persistent during the spring and fall months as well. During the summer the Beaufort high weakens substantially and can be replaced by a general lower pressure area with the center located over the North Pole.

Surface wind speeds are connected to Sea level pressure (SLP) patterns. Such patterns that can cause extreme wind events are cyclones in the Chukchi/Beaufort Seas, strong Aleutian

Low cyclones, and Strong Beaufort Highs or ridges (Lynch et al. 2004). Of course a strong cyclone moving into the Chukchi/Beaufort Sea whether from the Bering Sea or from elsewhere in the Arctic region will increase wind speeds at the surface. However if the Aleutian Low and or the Beaufort High are strong then there is a strong zonally oriented SLP gradient in the Chukchi/Beaufort Seas region that will drive stronger wind speeds.

The specific region of interest for this study is the Chukchi/Beaufort Seas, which is located on the edge of the Arctic region on the north coasts of Alaska and eastern Siberia below (Figure 1).
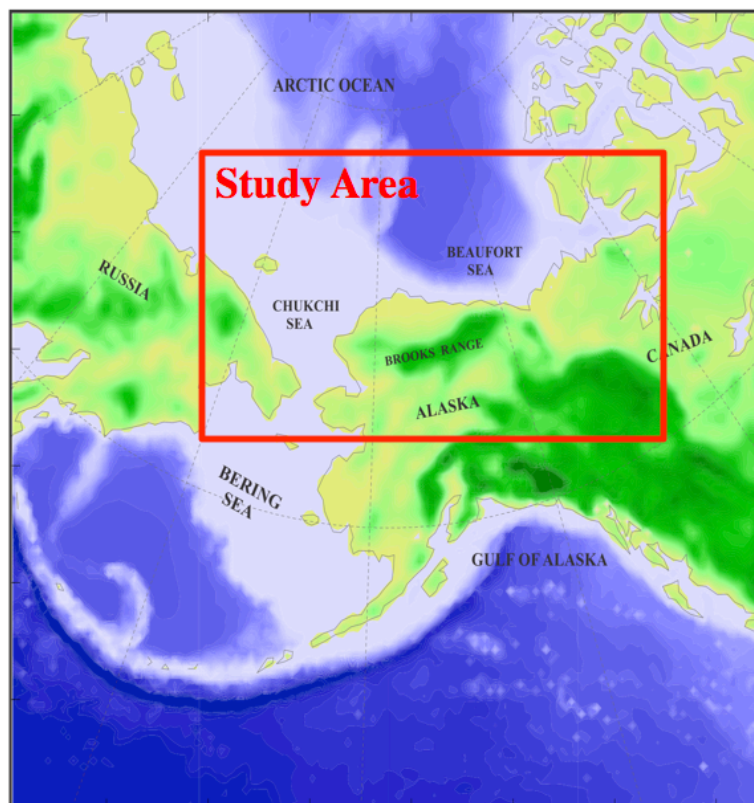


*Figure 1*. The Chukchi/Beaufort Seas geographic study region, shown by the red rectangle.

This region is also significant since it experiences seasonal changes in sea ice extent. With such changes this region will have both open ocean and sea ice, including areas of partially covered

sea ice, occurring mainly in the summer/fall seasons.  A region that has these physical features is known as a Marginal Ice Zone (MIZ).

The Chukchi/Beaufort Seas region has been particularly affected by the changing Arctic Climate (Lindsay and Zhang, 2005; Mahajan et al. 2011).   The Chukchi/Beaufort Seas region is an area of the Arctic with the greatest thinning rate of sea ice along with the Canadian and Greenland areas (Lindsay and Zhang, 2005).  Lindsay and Zhang, (2005) also show that the fall 2-m air temperature has changed the greatest in the Chukchi/Beaufort Seas, where is it warmer. The thinner sea ice could be responsible for more heat from the open ocean, higher amounts of absorbed solar flux, and reduction in sea ice from the ice-albedo feedback.   In turn this reduced sea ice extent is negatively correlated to higher wind speeds (Stegall and Zhang, 2012).

The observation of extreme wind events in the Chukchi/Beaufort Seas has been observed and studied in the past (Lynch et al. 2003; Lynch et al. 2004; Small et al. 2011) as well as by locals in the region who notice long term changes in the environment such as changes in sea ice, leads and open water areas, and mammals not previously found in the region.  Lynch et al. (2003) the main focus is on a couple of case studies of extreme wind events.  The two extreme storm cases did track into the Chukchi/Beaufort Region and impact Barrow Alaska and surrounding areas.   Their main focus for the two cases is storm development processes and documenting that the two cases were extreme events. However in Lynch et al. (2004) the study is focused on Barrow Alaska for their long-term studies.  They document temperature increases as well as changes in storm frequency and intensity.  In turn they report wind speed increases, especially in August and September.  Lynch et al. (2004) show the daily average maximum wind speeds as well as highest sustained wind speed, the highest observation reported for the season, and the highest sustained wind speed for the season broken into 3-month seasons, i.e., DJF,

MAM, JJA, and SON from 1945-2001. Overall the lowest wind speeds occur in JJA and the highest occur in SON and DJF. Throughout each season there are numerous extreme storm events but in the overall sense the Fall/winter months appear to have the highest winds speeds on average. Small et al. (2011) studies the climatology of wind speeds at Tuktoyaktuk (located in the Mackenzie River Delta and valley) along the Beaufort Sea in the Northwest Territories of Canada. They concluded that there are extreme wind events in both the late summer/fall and in winter. However they find the variability of extreme events to be higher in winter. There are also studies of individual storm events in Beaufort Sea (Lynch et al. 2003; Pickart et al. 2010; Swail et al. 2007). These studies give insight into the conditions of each of the particular storms but will not give any long-term climatological surface wind characteristics.

As mentioned above, the Chukchi/Beaufort Seas is a region, mainly during the summer/fall months that has both open ocean and sea ice (MIZ). In this region sea ice, SST (ocean surface) and surface wind speeds interact.

The Objective of this study is to provide a detailed climatology including trends, changes, and extremes in the Chukchi/Beaufort Seas of surface winds over a 31-year period, specifically 1979-2009. This study will also give a detailed climatology and trends of 2m-air temperature, SST, and sea ice concentration and sea ice extent in the Chukchi/Beaufort Seas. The focus will be given to mesoscale features (both ocean and land) that are not typically captured with global reanalysis datasets. In this way a very detail oriented, long-term climatology can be achieved in this region for use in climate research, especially Arctic, and Chukchi/Beaufort Seas related climate studies. Since studies are done at one geographic location over land (i.e. Lynch et al. 2004) it is difficult to extract the results to the overall region. The characteristics of the seasonality of the wind speeds might be very different over the open ocean versus land and

versus sea ice.  The intent of this study is to use gridded reanalysis data that assimilate the

observations done at locations in the regions and produce a gridded 31 year climatology that

show the overall characteristics of the surface wind speeds and wind direction but also of the

extreme wind events as well for each month of the year.

This dissertation will give a detailed climatology, including trends, of the 10m surface

wind field in the Chukchi/Beaufort Seas region using several different data sets.  Trends of other

variables such as sea ice, 2m temperature, and SST will also be done.  This analysis will include

detailed analysis of mesoscale features and physical explanations.  There will also be a study of

relationships of wind speed and SST in the region and physical explanations of the relationship.

These physical relationships can include temperature advection, net long and net short wave

radiation, and cloud cover as well as other meteorological variables.

**CHAPTER 2**

**Data and Methodology**

**2.1 Data**

Three reanalysis data sets are used in this study.  The first of which is the North

American Regional Reanalysis (NARR), (Mesinger et al. 2006).  The NARR data is available at

3-hourly output intervals and here is used from 1979-2009.  There are 45 layers in the vertical

and the horizontal grid spacing is at 32km.

The second data set used is the European Centre for Medium-Range Weather Forecasts

(ECMWF) Reanalysis, ERA-Interim (ERA-I) global data set.  The ERA-I data is from 1979-

2011 and is available at 6-hourly output intervals.  The Horizontal grid spacing is 0.75° X 0.75°,

and 60 layers (model levels) in the vertical (Dee et al. 2011).

A third data set used is the Chukchi/Beaufort High-resolution Atmospheric Reanalysis

(CBHAR).  This 31-year reanalysis is from 1979-2009 and is being made public by the Bureau

of Ocean Energy Management (BOEM).  The horizontal grid spacing is 10km at 1-hour output

intervals and 49 vertical levels (Zhang et al. 2013).

The observational database utilized in CBHAR includes Meteorological data from 262

stations in the Beaufort and Chukchi Seas region of the Arctic that were gathered.  These

locations include land-based locations (both inland and near-shore) as well as offshore data from

buoys, ships, exploration camps, and an ice camp.  Observed variables collected and used

include surface air temperature (°C), dew point temperature (°C), relative humidity (%), wind

speed (m s$^{-1}$), wind direction (degrees), station pressure (hPa), sea level pressure (hPa), altimeter

(in Hg), shortwave radiation (W m$^{-2}$), longwave radiation (W m$^{-2}$), 1-hr accumulated

precipitation (mm), 6-hr precipitation (mm), 24-hr precipitation (mm), and snow depth (cm). All data collected are from 1979-2009 with most stations reporting on an hourly or sub-hourly basis. Few stations possess data spanning the entire 31-year period; most stations possess records of less than 10 years. The observation data was subject to quality control described in detail in Zhang et al. (2013). Upper-air data is also utilized in CBHAR from the Integrated Global Radiosonde Archive through the National Climatic Data Center (NCDC) and can be found at: (http://www.ncdc.noaa.gov/oa/climate/igra). Twice-daily data at 0000 UTC and 1200 UTC are available for the period 1979 to 2009, though the Russian stations only have records through 1999 and Barter Island only through 1988. The stations with upper-air data include Barrow, Barter Island, Inuvik, Kotzebue, Mys Shmidta, Mys Uelen, and Ostrov Vrangelja, all of which are also long-term surface observing stations.

Here a brief description of the final model setup and data production will be discussed and adopted from Zhang et al. (2013), which can be referenced for a full description of the model setup and a detailed discussion of the CBHAR dataset.

The three-dimensional initial and lateral boundary conditions as well as gridded analysis that the Weather Research and Forecasting (WRF) model (Skamarock et al. 2008) is spectrally nudged and are forced by ERA-I reanalysis dataset. For the land-use data, the Moderate Resolution Imaging Spectroradiometer (MODIS) 20-category land-cover classification is used as part of the final CBHAR configuration. Seasonal sea ice cover characterizes the study area over the ocean and seasonal snow cover over land. Thus careful preparation was made for the specification of sea surface temperatures (SST), sea ice concentration (SIC) and thickness (SIT), snow depth, and snow water equivalent (SWE). To maintain consistency with the atmospheric fields, SST was taken from ERA-I for use with the CBHAR reanalysis. To provide sea ice

conditions, the NASA Bootstrap sea ice concentration derived from the Scanning Multichannel

Microwave Radiometer (SMMR) on board the Nimbus-7 satellite and the Special Sensor

Microwave/Imager (SSM/I) instrument on Defense Meteorological Satellite Program (DMSP)

satellites was acquired from the National Snow and Ice Data Center (NSIDC). These data are

available at a grid spacing of 25 km, and at a daily frequency since July 1987 and semi-daily

prior to that. SIT was taken from the 6-hourly Climate Forecast System Reanalysis (CFSR), a

recently developed reanalysis product produced by the National Centers for Environmental

Prediction (NCEP) at a 0.5° grid spacing. Due to the unavoidable discrepancies between the

selected SIT and SIC datasets, the SIC distribution was treated as the true areal coverage, and for

points where SIC was available and SIT was not, the SIT value was set to the closest available

value in the CFSR dataset.  Snow depth on land was acquired from the 32-km NARR reanalysis,

which in turn was taken from the 47-km daily U.S. Air Force Weather Agency (AFWA) snow

depth analysis.  The AFWA analysis is not produced over sea ice, and so snow data (SWE) on

ice were taken from the CFSR reanalysis. Since the AFWA analysis only provides snow depth,

and CFSR only provides SWE, another data source of snow density was required in order to

calculate SWE over land and snow depth over sea ice. The daily global Canadian Meteorological

Centre (CMC) snow depth analysis provided by NSIDC, which includes SWE as calculated from

snow density climatological lookup tables, was used for this purpose.

     The final configuration of WRF is briefly summarized here.  Physical parameterization

options for the production of the final CBHAR reanalysis are: Morrison microphysics (Morrison

et al. 2009), RRTMG longwave and shortwave radiation (Iacono et al. 2008), Grell-3D cumulus

(Grell and Devenyi, 2002), MYJ PBL and surface layer (Janjic, 2002; Mellor and Yamada,

1982), and the Noah LSM (Chen and Dudhia, 2001). A new thermodynamic sea ice model was

also coupled with WRF and selected Polar WRF (Bromwich et al. 2009; Hines and Bromwich 2008; Hines et al. 2011) options were adopted as well, namely the use of variable sea ice thickness data and a more realistic bottom sea ice temperature.

The WRF Data Assimilation (WRFDA) was configured to assimilate in situ surface station and radiosonde observations of temperature, dew point, wind vectors, and pressure (geopotential height for radiosondes), satellite-derived Quick Scatterometer (QuikSCAT) ocean-surface winds, polar winds derived from MODIS and Advanced Very High Resolution Radiometer (AVHRR) measurements, and selected temperature and moisture profiles retrieved from MODIS data. A customized model background error file created specifically for the CBHAR domain was included in the CBHAR reanalysis configuration. Spectral nudging to the input ERA-I reanalysis was also utilized with a horizontal wavenumber of 3.

The production of CBHAR is done through a parallelized, iterative process whereby a series of 54-hour runs, initialized every tow days throughout the 31-yr period are produced. Within each of these runs WRF is first initialized at 12 UTC and observations within 30 minutes of the initialization time are assimilated. The model is integrated for an hour, and then stopped and more observations are assimilated at 13 UTC. This process is repeated for the entire 54-hour cycle, with the first 6 output times discarded, having only been used to spin up the model. The remaining 48 hourly output (the output of each assimilation cycle) are kept in order to be part of the final product, resulting in the final CBHAR reanalysis.

**2.2 Methodology**

The following is a detailed description of the methodology used throughout this study. Monthly average, maximum, and 95th percentile wind speeds are calculated at each grid point for the study area discussed in Chapter 1. The monthly average wind speeds are calculated by

averaging all times (i.e. hourly, 3-hourly, 6-hourly) surface winds for each month for the 31-year period. The monthly maximum wind speeds are determined by selecting the maximum wind speed from the number of times for the winds for each month over the 31-year period. To calculate the percentile wind speeds the speeds are sorted from least to greatest at each grid point. The rank, $R_k$ then can be calculated as follows:

$$R_k = ((N/100)*P + 0.5),$$

where N is the total number of values and P is the percentile (90 or 95 here). Let $P_{90}$ and $P_{95}$ represent the 90th and 95th percentiles respectively. Thus:

$$P_{95} = R_{dec}*(A(R_{whole}+1) - A(R_{whole})) + A(R_{whole}),$$

where $R_{dec}$ and $R_{whole}$ are the whole part of rank and the decimal part of rank, and A is the sorted array at each grid point.

The trends of monthly average and 95th percentile wind speeds for the entire 31-year period are also analyzed with linear regression coefficients, in which a positive value indicates an increase in wind speed and a negative value represents a decrease over the 31-year period. To investigate the variations of extreme wind events we define the extreme wind event as a wind speed greater than the monthly 95th percentile wind speed over the entire 31-year period. Then the occurrence frequency of the extreme wind events expressed as a percentage is calculated over a time period. The 31-year domain averaged 3-hourly winds are calculated to represent the diurnal variation of wind speeds on each day of the month. The calculations are broken into land-

only and ocean-only areas so that the diurnal cycles between the land and ocean winds can be compared.

For the wind direction climatology, we first divide all the directions into quadrants between 0-90° representing the winds from northeast, 90-180° from southeast, 180-270° from southwest, and 270-360° from northwest. Then the monthly frequency of wind directions in each quadrant is calculated for each month for the 31-year period.

To investigate the relationships of SST, sea ice, clouds, stability, and wind speed the method of binned scatter plots of a dependent variable based on binned independent variable, i.e. binned wind speed anomalies dependent on binned SST anomalies. In this way an exceptionally large amount of data is represented with only a handful of meaning full data points.

To study areal relationships further without necessarily assuming a linear relationship, composites are created following Schweiger et al. (2008). This methods takes a variable $V(i,y,x)$, where i is the time. Let $\{V(y,x)\}$ be the temporal mean of variable V, and $\sigma(y,x)$ be temporal standard deviation. A collection of times, $i_+$ corresponding to the times that satisfy $V(i_+,y,x) > \{V(y,x)\} + b*\sigma(y,x)$ and $N_+$ is the number of times in the collection. Similarly $V(i_-,y,x) < \{V(y,x)\} - b*\sigma(y,x)$, where $N_-$ is the number of times in this collection. The parameter, b, is a way to measure the sensitivity of variable V to changes in variable V's standard deviation, i.e. changes in the standard deviation of wind speed anomalies. With these positive and negative composites defined, positive and negative anomalies are constructed such that:

$$V1(i_+,y,x) > \{V1(y,x)\} + b*\sigma(y,x) \text{ then}$$

$$V1'(i_+,y,x) = V1(i_+,y,x) - \{V1(y,x)\}; \quad V2'(i_+,y,x) = V2(i_+,y,x) - \{V2(y,x)\}$$

and similarly:

$$V1(i_-,y,x) < \{V1(y,x)\} - b*\sigma(y,x) \text{ then}$$

$$V1'(i_-,y,x) = V1(i_-,y,x) - \{V1(y,x)\}; \quad V2'(i_-,y,x) = V2(i_-,y,x) - \{V2(y,x)\}$$

In this way $V'(i_+,y,x)$ are the positive anomalies associated with the positive composite times and $V'(i_-,y,x)$ are the negative anomalies associated with the negative composite times. After these anomaly composites are created they are summed up as: $1/N_+ \, \Sigma_{i+} V'(i_+,y,x)$ for the positive anomalies and $1/N_- \Sigma_{i-} V'(i_-,y,x)$ for the negative anomalies.

To explore possible relationships between two variables, corresponding composites are generated as above for the 2 variables. In this way the positive and negative anomaly composites of variable V2 correspond to positive and negative composites of variable V1, i.e. positive wind speed anomalies corresponding to negative sea ice anomalies. These composites can thus give areal information about these relationships.

**CHAPTER 3**

**Wind Field Climatology, Changes, and Extremes in the Chukchi-Beaufort Seas and Alaska North Slope during 1979-2009**

**Abstract**

Wind field climatology, changes, and extreme at ~32km resolution were analyzed for the Chukchi-Beaufort Seas and Alaska North Slope region using 3-hourly North American Regional Reanalysis (NARR) from 1979 to 2009. The monthly average winds show a clear seasonal cycle with a minimum of 2-4 ms-1 in May and a maximum up to 9 ms-1 in October. The 95th percentile winds show a similar seasonality with a maximum up to 15 ms-1. The 31-yr domain averaged 3-hourly wind speeds display a clear diurnal cycle over land and sea ice areas during the warm seasons. Weaker radiation during winter and larger heat capacity over open water reduce the diurnal signal in the wind field diurnal variations. There were increasing trends of areal averaged monthly mean and 95th percentile wind speeds for July through November. The strongest increase in the areal averaged 95th percentile winds speeds occurred in October from 7 ms-1 in 1979 to 10.5 ms-1 in 2009. The frequency of extreme wind events (speed above the 95th percentile winds) shows an increasing trend in all months, with the greatest increase occurring in October, showing 8% more extreme wind events in 2009 comparing to 1979. The prevailing wind direction was northeast with a frequency of 40%-60% for most of the year. The frequency for southwest and northwest winds was small (<20%) except for two anomalous areas along the Brooks Range in Alaska and the Chukotka Mountains in easternmost Russia where the frequency has increased to 35%-50% during the cold season months.

**3.1 Introduction**

The Chukchi-Beaufort Seas and the adjacent continental region (Figure 2) is a prominent geographical feature, whish is largely covered by sea ice on a seasonal basis over the ocean and bounded by the Brooks Range in the south on land. The complex orographic dynamics and seasonally changed surface conditions significantly complicate the mesoscale weather systems and the associated surface winds (Kozo 1979, 1980; Lynch et al. 2003, 2004). In addition, substantial environmental changes have occurred in the Arctic over the past several decades, including an increased storm invasion (e.g., Zhang et al. 2004), a large fluctuation in the surface pressure pattern (e.g., Thompson and Wallace 1998; Overland et al. 2008; Zhang et al. 2008), a conspicuous warming of surface air and ocean water temperatures (e.g. ,Comiso 2006; Shimada et al. 2006), and a drastic retreat of sea ice (e.g., Comiso et al. 2008; Polyakov et al. 2012). These great changes and variability in the Arctic sea ice, atmosphere, and ocean will definitely further complicate the atmospheric circulation and associated wind field in the Chukchi-Beaufort Seas region. Significant modeling and data analysis efforts have been inspired to better represent, understand, and predict these changes (e.g., Bromwich et al. 2009, 2010; Zhang and Zhang 2010; Cassano et al. 2011).
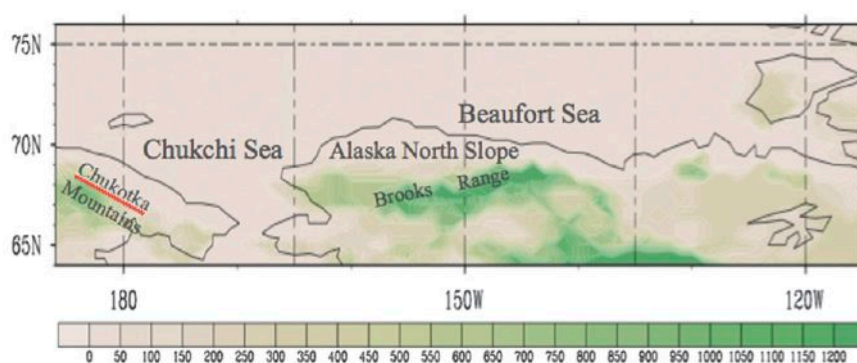


*Figure 2.* Topography (m) of study domain.

Meanwhile ongoing oil development in the Chukchi-Beaufort Seas is always potentially accompanies by the threat of oil spills. As the recent event in the Gulf of Mexico has unfortunately demonstrated, such spills have an extraordinary impact on the sensitive ecosystems in surrounding regions. In the event of such a spill, timing is of the essence in directing mitigation, cleanup, and recovery efforts, and thus improving the prediction of oil spill transport is of great importance to all concerned. As the surface wind field is the primary factor is driving upper ocean currents, and thus the dispersal of oil spills, understanding and accurately modeling the region's surface winds is essential in assessing and enhancing the prediction of oil spill transport.

High wind events at Barrow along the northern coast of Alaska have been extensively studied by Lynch et al. (2003, 2004) and it is reported that the strong sustained winds of 25 ms$^{-1}$ occurred at Barrow, Alaska, on October 3-5 1963 and August 10-11 2000. How often did the extreme wind events like this occur in the Chukchi-Beaufort Seas and the Alaska North Slope? What are the climatological features of the surface wind field in this area? All of these have not been well documented, and are essential information for accurate oil spill transport assessment and modeling. This study will describe the wind field climatology and analyze wind extremes for the Chukchi-Beaufort Seas and the Alaska North Slope region with a long-term reanalysis data. The data we used for this study and analysis methodology are described is section 3.2. Section 3.3 compares the reanalysis winds with the in situ measurements for the study area. Then the wind speed and direction climatology are analyzed in sections 3.4 and 3.5. Finally a summary of this study is given is section 3.6.

**3.2 Data and Methodology**

The data we used for this study are the 3-hourly, 10-m surface winds and sea level pressure from North American Region Reanalysis (NARR; Mesinger et al. 2006) at ~32km resolution for the 31-yr period of 1979-2009.  First the monthly average, maximum, and 95th percentile wind speeds were calculated at each NARR grid point for the study area covering the Chukchi-Beaufort Seas, Alaskan North Slope, and the adjacent Brooks Range, as well as northwestern Yukon and easternmost Russia.  The monthly average wind speeds were calculated averaging all the 3-hourly NARR surface winds for each month for the 31-yr period.  The monthly maximum wind speeds were determined by selecting the maximum wind speed from the 3-hourly NARR winds for each month over the 31-yr period.  Sorting the 3-h NARR winds over the 31-year period from the lowest to highest for each month and then locating the 95th percentile values determined the monthly 95th percentile winds.

The trends of monthly average and 95th percentile wind speeds for the entire 31-yr period were also analyzed with linear regression coefficients, in which a positive value indicates an increase in wind speed and a negative value represents a decrease over the 31-yr period.  To investigate the variations of extreme wind events we define the extreme wind event as a wind speed greater than the monthly 95th percentile wind speed over the entire 31-yr period.  Then the occurrence frequency of the extreme win events expressed as a percentage is calculated over a time period.  The 31-yr domain averaged 3-hourly winds were calculated to represent the diurnal variation of wind speeds on each day of the month.  The calculations were broken into land-only and ocean-only areas so that the diurnal cycles between land and ocean winds can be compared.

For the wind direction climatology, we first divided all the directions into quadrants between 0° and 90° representing the winds from the north-northeast (NNE), north-east (NE), and

east-northeast (ENE); 90°-180° from the east-southeast (ESE), southeast (SE), and south-southeast (SSE); 180°-270° from the south-southwest (SSW), southwest (SW), and west-southwest (WSW); and 270°-360° from the west-northwest (WNW), northwest (NW), and north-northwest (NNW). Then the monthly frequency of wind directions in each quadrant was calculated for each month for the 31-yr period.

## 3.3 Comparison of NARR Surface Winds with Observation

A comparison of the NARR reanalysis surface winds with the *in-situ* measurements was conducted. A total of 194 surface stations data were collected from different data networks including the National Climate Data Center (NCDC; 103 stations), Remote Automated Weather Stations (RAWS; 32 stations), Water Environmental Research Center (WERC) at the University of Alaska Fairbanks (UAF; 28 stations), Bureau of Ocean Energy Management, Regulation, and Enforcement (BOEMRE; previously Minerals Management Service; 5 stations), the Atmospheric Radiation Measurement (ARM) network (2 stations), the National Data Buoy Center Coastal-Marine Automated Network (C-MAN) program (2 stations), the industry well sites and coastal measurements, and some short-term offshore measurements by UAF and Shell company (22 stations). All of these collected data have been quality controlled with three quality control (QC) procedures (Shulski and You 2011). These procedures check for instances of an observation falling outside of the normal range, consecutive values that have too large of a difference, and instances of too high or too low variability in the observations. Criteria for the quality control were defined based on a stations' climatology.

The NARR reanalysis winds were interpolated to the locations of these stations for a direct comparison with the observational data. The Taylor diagram (Taylor 2001) was first used for this evaluation analysis (Figure 3). Standard deviation was calculated based on wind

persistence following Farrugia and Micallef (2006) and then normalized by the observed value. The correlation of wind direction was calculated following the method introduced by Crosby et al. (1993) in which the wind vector correlation was calculated with a formula in terms of the orthogonal components of two vectors. The data were grouped into inland and coastal stations (Figure 3 top) and four seasons (March-May for spring, June-August for summer, September-November for autumn, and December-February for winter) (Figure 3 bottom). The coastal stations are those where measurements were taken offshore or onshore but within a distance of 30 km from shoreline.
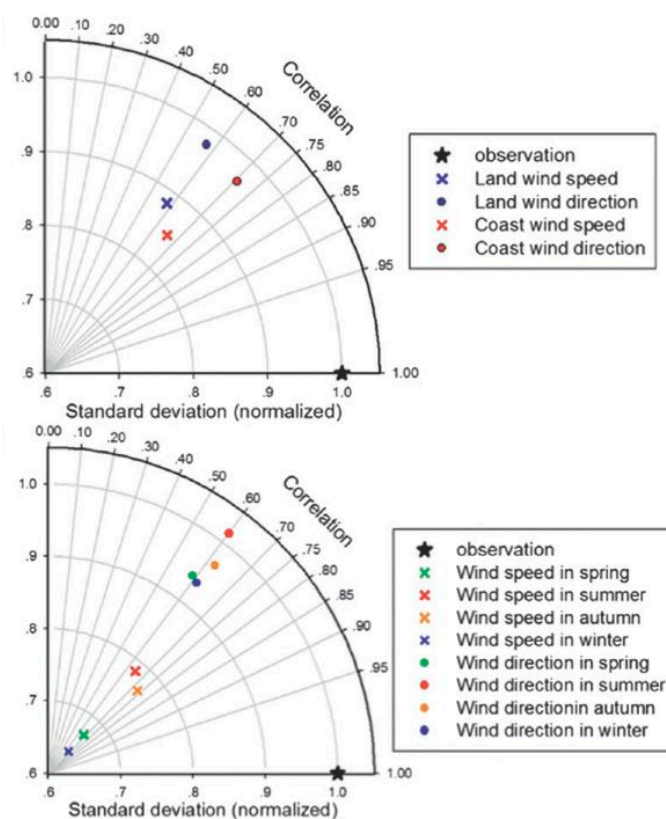


*Figure 3.* Taylor diagram of wind speed (cross) and direction (dots) variances and correlations between (top) NARR reanalysis winds and station measurements for land (blue) and coast stations and (bottom) four seasons spring (green), summer (red), autumn (orange), and winter (blue).

The inland stations include those where measurements were taken onshore 30 km away from the shoreline.  In total ther4e are 59 coastal stations and 81 inland stations available in this comparison analysis when the data requirement is applied that the number of valid hourly measurements within each month be larger than 360 for the 30-yr study period.

The NARR reanalysis winds show a better correlation with the coastal observations.  The averaged correlation coefficients are 0.71 for direction and 0.66 for wind speed along the coast, and 0.57 for direction and 0.58 for wind speed inland (Figure 3 top).  The normalized standard deviations of the NARR wind direction are as high as 0.97 along the coast and 0.98 inland (Figure 3 top), suggesting that the variance pattern of NARR wind direction is very close to the observed one.  The variance of NARR wind sped is slightly off from the observed pattern.  The normalized standard deviations of the NARR wind speed are 0.88 inland and 0.85 along the coast.

In terms of the performance of NARR winds in each season, it is shown that the variance patterns of summer and autumn winds are closer to the observations than the winter and spring winds, especially for wind speed (Figure 3 bottom).  The correlation between the reanalysis and the observed winds does not vary very much across each season, although a better correlation occurs in autumn with correlation coefficients of 0.73 for wind speed and 0.63 or wind direction. Overall the NARR winds have a reasonable agreement with the in situ observations for the study area, especially over the coastal region, which can be further shown from geographical distribution of wind vector correlation between the NARR reanalysis and the observation (Figure 4 top).  To have an estimate of the reanalysis error for the offshore area, all the collected offshore observations regardless of he length of the measurement period, at a total of 22 stations, were

also included in this analysis as shown by the cross in Figure 4 top. The correlations are generally better alongshore and offshore than inland. It is also noticeable hat the NARR winds have a relatively poor correlation with the observations at some stations. The correlations for a total of 13 stations are smaller than 0.5; among them are 9 stations from WERC network. When applying the QC procedures to all the collected observations, it has been found that the flagged number of questionable data is the highest in the WERC data (Shulski and You 2011). More strict QC procedures can be applied to the observational data, but this can significantly limit the quantity of valid data (Shulski and You 2011). The wind speed bias analysis (Figure 4 bottom) shows that the NARR reanalysis teds to have negative biases alongshore and offshore and positive biases inland. The positive bias inland can be attributed to the coarse resolution in NARR.
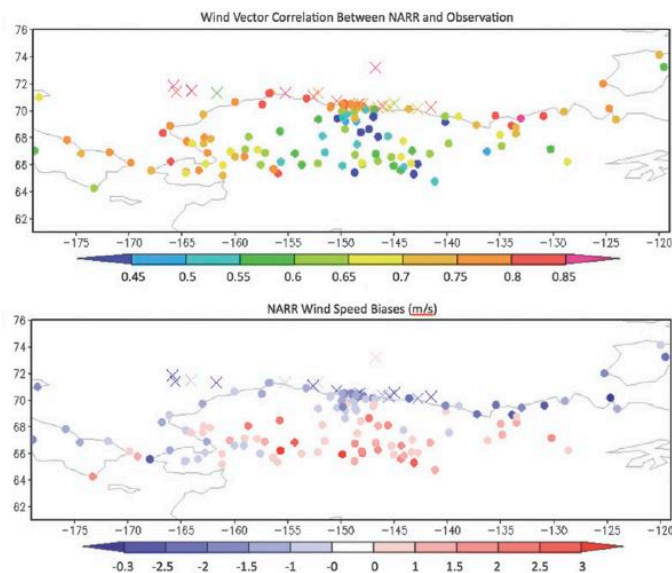


*Figure 4.* Wind vector correlation between (top) NARR reanalysis and station observations and (bottom) NARR wind speed bias (ms$^{-1}$). Dots represent onshore stations and crosses offshore stations. The four seasons are represented as spring (green), summer (red), autumn (orange), and winter (blue).

## 3.4 Wind Speed Climatology, Changes, and Extremes

**3.4.1 Seasonal and diurnal variations.** Monthly average wind speeds in the study area demonstrate a clear seasonal cycle (Figure 5).
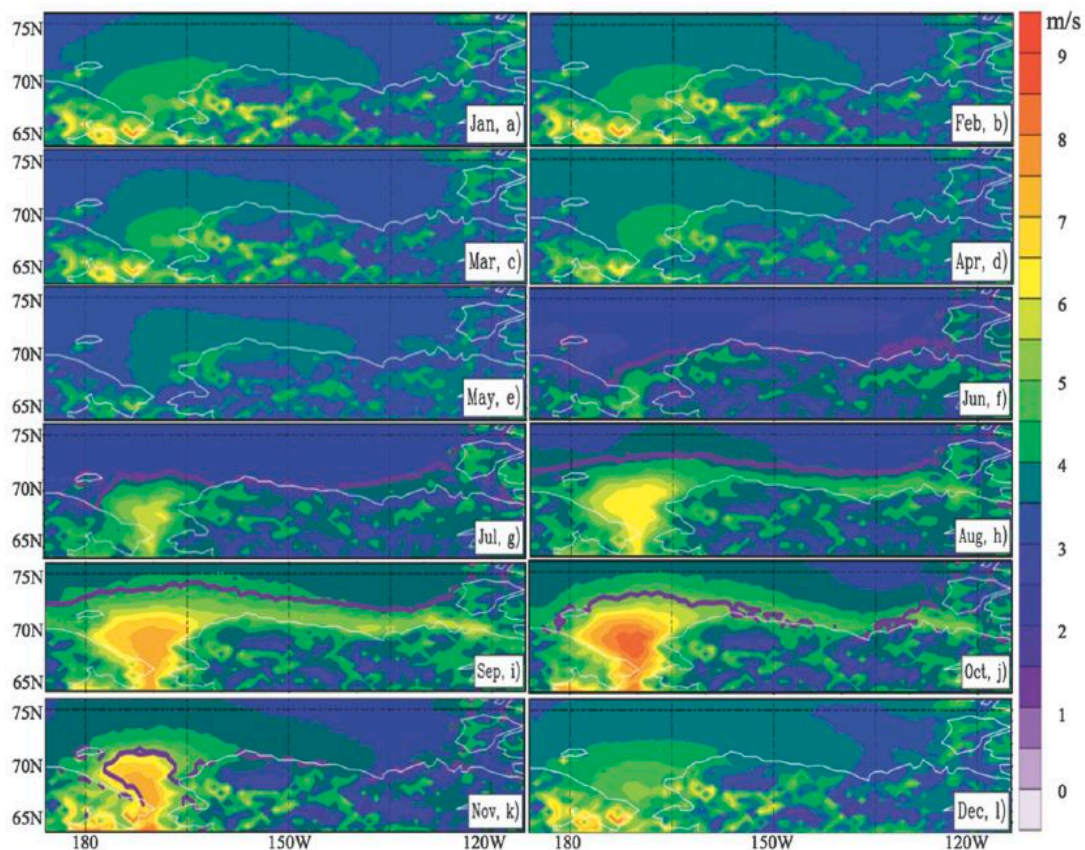


*Figure 5*. Monthly mean wind speed (color; ms$^{-1}$) and 50% sea ice concentration (purple curves) during 1979-2009.

The minimum wind speeds occur in May and June at ~2.5 ms$^{-1}$. Then the wind speeds in the Chukchi Sea begin to increase steadily and reach 5-6 ms$^{-1}$ in July; however, the winds in the Beaufort Sea do not change very much from May to July. In August the maximum speeds in the Chukchi Sea basically keep the same as in July but 5-6 ms$^{-1}$ isotachs cover a mush larger area. On the other hand, the winds in the Beaufort Sea begin to increase by about 1 ms$^{-1}$ in August.

The wind speeds reach a maximum at the center of the Chukchi Sea. Starting in November, the winds begin to decrease, becoming less than 4ms$^{-1}$ in the Beaufort Sea and around 5ms$^{-1}$ in the Chukchi Sea in December. Overall the seasonal variation of wind speed in the Chukchi Sea is much stronger that in the Beaufort Sea. The wind speed annual ranges are about 6 ms$^{-1}$ in the Chukchi Sea and 3 ms$^{-1}$ in the Beaufort Sea. The wind speed in the North Slope has relatively small seasonal variation except that a greater wind of ~6 ms$^{-1}$ occurs over the Brooks Range during the winter months. When the monthly mean contours of 50% sea ice concentration (purple cures in Figure 5) are overlaid on the monthly wind speeds, they show a clear synchronized behavior between the poleward retreat of sea ice extent and poleward shit of the maximum winds.

The maximum and 95$^{th}$ percentile wind speeds over the 31-yr period were also analyzed for each month to investigate the seasonal extreme wind field features in the study area. A similar seasonality as seen in the monthly average wind was found, with strong winds in fall and calm winds in spring (not shown). The monthly maximum wind speeds over the 31-yr period for the entire study area are 8-11 ms$^{-1}$ in May and 18-28 ms$^{-1}$ in October. The 95$^{th}$ percentile wind speeds are around 5-7 ms$^{-1}$ in May and then increase to 9-11 ms$^{-1}$ in July in the Chukchi Sea and show little change in the Beaufort Sea. In September and October, the 95$^{th}$ percentile winds reach maximum values of 10-15 ms$^{-1}$ over the study area.

To illustrate the systematic distribution of the entire domain winds, we also conducted a seasonal probability analysis for the 31-yr period (Figure 6). The monthly probability distribution function (PDF) (Figure 6a) and cumulative distribution function (CDF) (Figure 6b) of the entire domain winds show that he chance of wind speeds between 2 and 5 ms$^{-1}$ dominates the study area by about 60% (CDF 80% around 5 ms$^{-1}$ minus CDF 20% around 2 ms$^{-1}$).
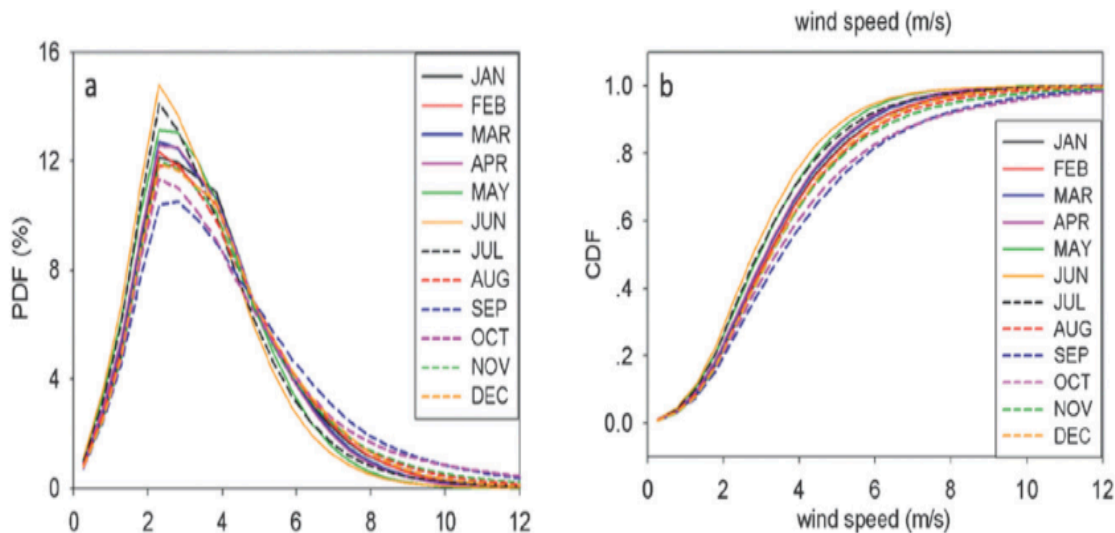
*Figure 6.* Monthly (a) PDF and (b) cumulative density function (CDF) of domain winds during 1979-2009.

These 2-5 ms$^{-1}$ wind speeds do occur the most for every month, but the probability during the early summer months (May and June) is greater than during the autumn months (September and October) by about 20% (CDF 90% in June minus CDF 70% in September around 5 ms$^{-1}$). The monthly probability of relatively strong winds (>5 ms$^{-1}$) demonstrates a completely opposite distribution where the greater winds occur more frequently in autumn than the early summer. For instance, winds greater than 5 ms$^{-1}$ occur in September and October with a frequency of 30% (CDF 100% around 12 ms$^{-1}$ minus CDF 70% around 5 ms$^{-1}$), but only about 10% (CDF 100% around 12 ms$^{-1}$ minus CDF 90% around 5 ms$^{-1}$) in May and June. The seasonal variability of domain winds' PDF and CDF is consistent with the seasonal wind speed climatology in the study area.

The 31-yr domain averaged 3-hourly winds on each day of the month show a clear diurnal cycle over land during the warm seasons (April-September) and over ocean during spring (mid-March-May) (Figure 7).
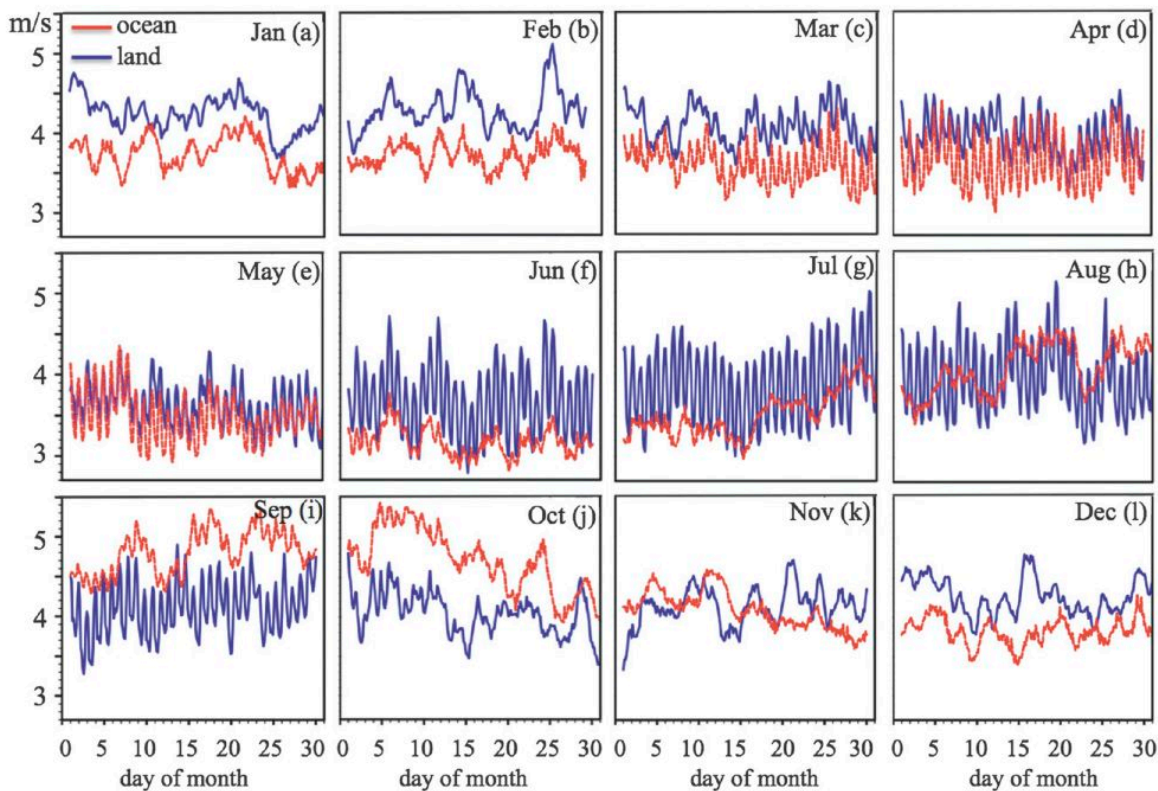
*Figure 7.* 31-yr domain averaged 3-hourly wind speed (ms$^{-1}$) in each month over ocean (red) and land (blue).

The diurnal cycle of the land winds, with the strongest variations in June and July, is obviously attributable to the strong diurnal solar radiation forcing and small land heat capacity, which gives rise to more stable conditions and low wind speeds around midnight and more unstable conditions and higher wind speeds around noon.  In winter the weak radiation forcing and the associated cold surface condition tend to create a very stable boundary layer; thus, the changes in surface wind speeds should be largely influenced by the weather system.  Note that the ocean in the study area is covered by sea ice seasonally.  The sea ice-covered Chukchi-Beaufort Seas have more continentality and thus a lower heat capacity compared to the open water.  As a result, the diurnal cycle of sea ice surface thermal properties are closer to that of the land rather than the

ocean; the sea ice surface winds show a diurnal variation during mid-March to May when the solar radiation forcing is getter greater day by day.  The diurnal signal is negligible in the open ocean surface winds due to a large water heat capacity.

  **3.4.2 Long-Term trend.**  Domain-averaged monthly mean and 95$^{th}$ percentile wind speeds were calculated for each month in each year.  A pronounced increasing trend (Figure 8)
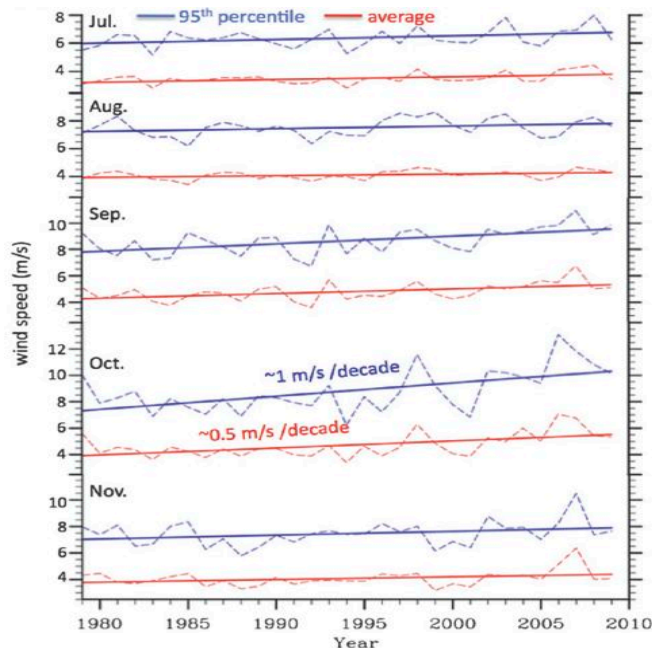


*Figure 8*. Domain averaged monthly (July-November) mean (blue) and 95$^{th}$ percentile (red) wind speeds from 1979-2009.

 exists from July through November during the entire 31-yr period although the upward trend occurred throughout the year at a significance level of 95% through an F-test.  The largest increase for the monthly average and 95$^{th}$ percentile winds all occurs in October, in which the average winds increase from ~4.0 ms$^{-1}$ in 1979 to ~5.5 ms$^{-1}$ in 2009 and the 95$^{th}$ percentile winds from ~7 ms$^{-1}$ in 1979 to ~10.5 ms$^{-1}$ in 2009.

It has been well understood that the sea ice extent over the Chukchi-Beaufort Seas demonstrates a drastic decreasing trend and a large variance of variability (e.g., Comiso et al. 2008). Changes in sea ice and its associated upper ocean thermal and kinematic conditions (e.g., air temperature gradient and surface toughness) may alter the overlaying atmospheric circulation and weather to impacts winds. This encourages us to investigate how sea ice and surface wind are related. The correlation coefficients between the monthly mean sea ice extents and monthly mean wind speeds over the study area show a strong negative correlation during the months of July-December with a 95% confidence level as summarized in Table 1. The correlation between sea ice extent and wind speed during January-June is much weaker and not significant.

Table 1

*Correlation coefficients between monthly mean sea ice extents and monthly mean surface winds during July-December with 95% significant level.*

| Jul | Aug | Sep | Oct | Nov | Dec |
|-------|-------|-------|-------|-------|-------|
| −0.76 | −0.68 | −0.73 | −0.85 | −0.67 | −0.82 |

Monthly linear trend distributions were analyzed with the linear regression coefficients of monthly wind speeds at each grid point of the study area (Figure 9) and it is shown that the wind speeds in the Chukchi-Beaufort Seas generally have an increase trend from July through November over the entire 31-yr period. The strongest increase, which is as high as 0.7 ms$^{-1}$decade$^{-1}$, occurs in the northern Chukchi Sea and eastern Beaufort Sea. However, a relatively

strong decreasing trend also exists around the southern Chukchi Sea region in September and

along the Beaufort Coast in November.
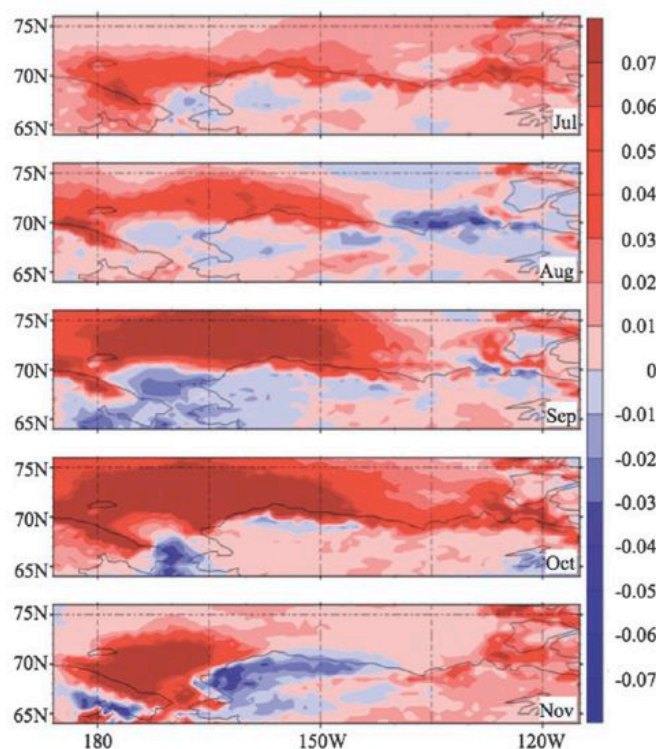


*Figure 9.* The monthly (July-November) wind speed linear trends (ms[-1-year]) distributions during

1979-2009.

That increasing trend in the northern Chukchi Sea concurs with decreasing trend in the

southern Chukchi Sea seems to correspond with the poleward shift of northern Pacific storm

track (Zhang et al. 2004), which deserves further investigation.  A comparison of decadal

probability density function of the entire domain winds further provides an insight into how the

wind spectra change during three decades of 1980-89, 1990-99, and 2000-09.  An obvious shift

of wind speed PDF pattern occurs in the most recent decade especially during the autumn

months: reduced density in calm winds (around 3 ms^{-1}) and enhanced density in strong winds (>6

ms$^{-1}$).  The PDF patterns between the first two decades of 1980-89 and 1990-99 are very close

(Figure 10).
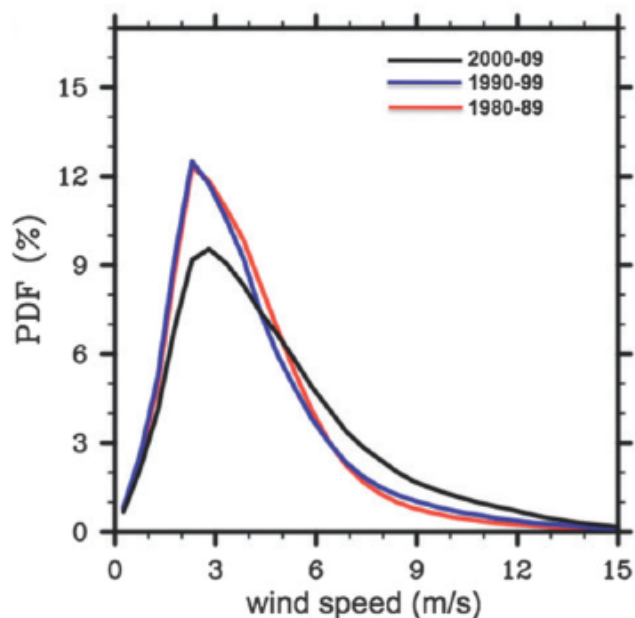


*Figure 10.* The PDF of October winds during the three decades of 1980-89, 1990-99, and 2000-

09.

We defined the frequency of extreme wind events as the occurrence of wind speeds

greater than the 95$^{th}$ percentile winds for the study period.  In detail, the frequency is calculated

as a percentage of the counting number of wind speeds greater that the 95$^{th}$ percentile winds

divided by the total number of available data for a given period.  Once this is calculated at each

grid point of the study domain, the domain-averaged frequency of extreme wind events is taken

for each month in each year.  The increasing trend in the frequency of extreme wind events

occurs almost every month (black lines in Figure 11), unlike the increasing trend in wind speeds,

which mainly occurs from July through November (Figure 8).  A relatively large frequency

increase (>5%) occurs in fall [September-November (SON)], when the sea ice extent in the study

area reaches a minimum and also shows the strongest decreasing trend during the 31-yr period (not shown). Possibly the widely opened water provides energy to force more frequent extreme wind events. With more open water there would be more sensible and latent heat fluxes release into the atmosphere from the ocean, which can further destabilize the atmosphere and enhance low-level baroclinicity (Businger and Baik 1991). Synoptic weather systems and the associated surface winds can be further strengthened because of increased baroclinic instability in the atmosphere. Again we see the greatest frequency increase in October, when we have 8% more extreme events in 2009 comparing to 1979.

The strongest frequency increase of extreme wind events in October concurs with the strongest increase of wind speeds (both monthly mean and 95th percentile winds) in October (Figure 8). It is noticeable that the frequency of extreme wind events is relatively high during most months of 2006 and 2007. Thus a question arises naturally: How much of the increasing trend is due primarily to the high values of 2006 and 2007?
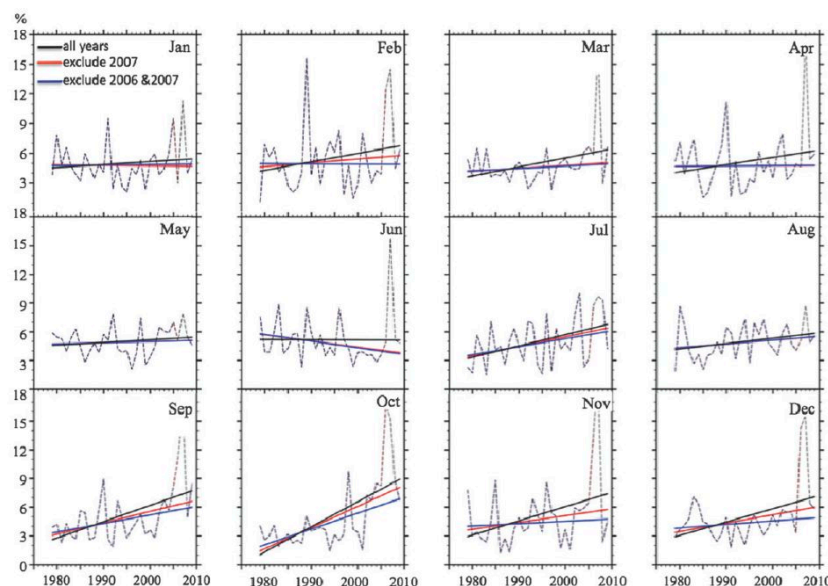


*Figure 11.* The monthly frequency of extreme wind events from 1979 to 2009 and linear trends (all years in black, 2007 excluded in red, and 2006 and 2007 excluded in blue).

We conducted two more trend analyses, one (red line of Figure 11) excluding 2007 and the other (blue line of Figure 11) excluding both 2006 and 2007; that is, the frequency values for the excluded year were set to missing values and the trend was recalculated. The increasing trend still exists during most months although the rate of increasing trends decreases. The strongest increase still happens in October with more that 4% more extreme wind events in 2009 comparing to 1979 when both 2006 and 2007 were excluded.

We further investigated the frequency distribution of extreme wind events that occurred in the autumn months of September to November for three decades of 1980-89, 19909-99, and 2000-09, which gives us some insight into how the frequency of the extreme wind events varies by decade and where the extreme win events are increasing or decreasing (Figure 12).
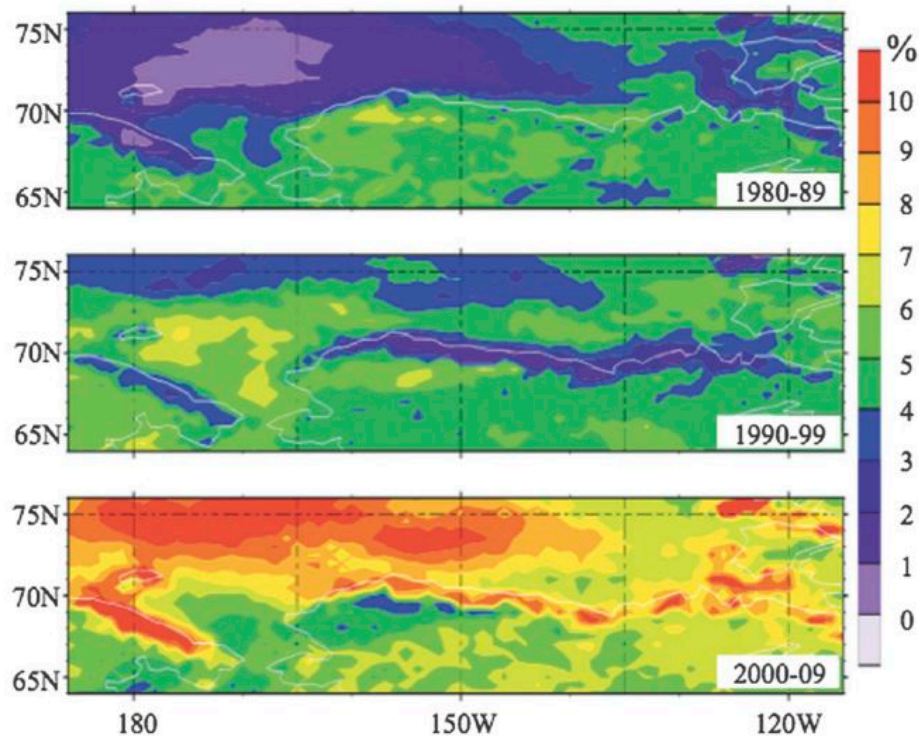


*Figure 12.* The frequency distributions of extreme wind events in fall (SON) during the three decades of 1980-89, 1990-99, and 2000-09.

Over most study areas, the frequency was less than 2% over the northern Chukchi Sea and

western Beaufort Sea during the first decade (1980-89), then increased to 4%-7% during the

second decade (1990-99) and reached 10% and higher in the third decade (2000-09).  On the

other hand, the frequency of extreme events over the southern Chukchi Sea, northern Bering

Strait, and the North Slope does not change much from the first decade to the third decade.

Obviously the distribution of frequency increase (Figure 12) is basically consistent with that of

the long-term trend (Figure 9), suggesting that the increase of wind speed is accompanied by

more frequent extreme wind events.

**3.5 Wind Direction Climatology and Mesoscale Structures**

   **3.5.1 Seasonal variation.**  The monthly frequency of wind directions in four quadrants of

northeast (0°-90°), southeast (90°-180°), southwest (180°-270°), and northwest (270°-360°)

during the entire 31-yr period depicts a seasonal variation.  The northeast quadrant (NEQ)

represents winds approximately from the NNE, NE, and ENE; the southeast quadrant (SEQ)

from the ESE, SE, and SSE; the southwest quadrant (SWQ) from the SSW, SW, and WSW; and

the northwest quadrant (NWQ) from the WNW, NW, and NNW.  The prevailing wind direction

in the Chukchi-Beaufort Seas and the North Slope is from the NEQ with a frequency around

40%-60% during most of the year (Figure 13), although the area under the NEQ winds is much

greater during the cold season months (October-May).  The frequency of 60% or higher of the

NEQ winds are mainly controlled by the Beaufort high located in the area almost year round,

although with the greatest strength in March and least in August (Figure 14)
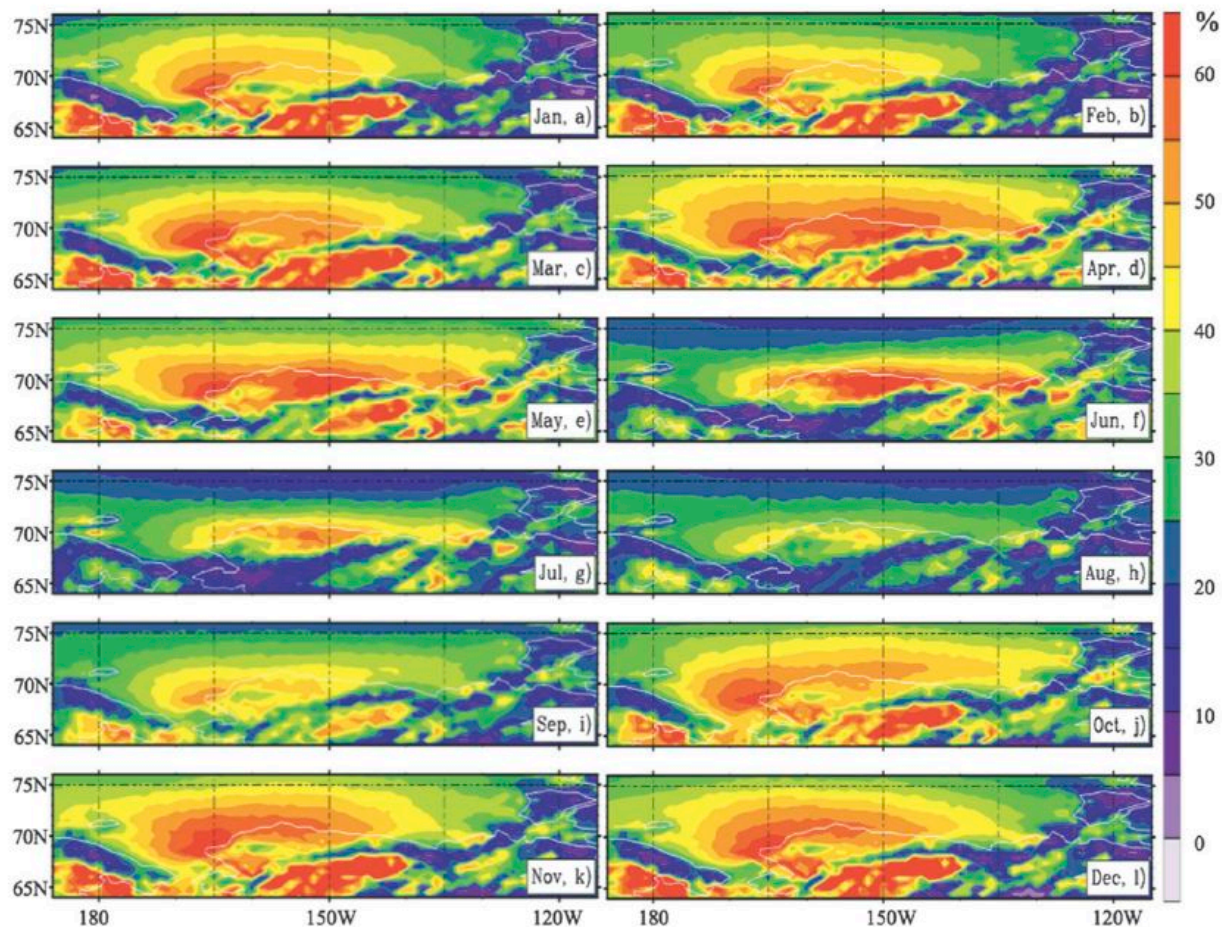
*Figure 13.* Monthly frequency of northeast winds during 1979-2009.

Starting in June, the areal extent of NEQ winds quickly shrinks to the coast region and the frequency begins to decrease in July and reaches minima in August. From October, the areal extent of NEQ winds begins to expand again. The seasonality in the frequency and areal extent of NEQ winds are consistent with the temporal evolution of the Beaufort high as described by Overland (2009). The 30-yr monthly mean sea level pressure with the NARR reanalysis over the study area (Figure 14) demonstrates that the Beaufort high reaches its peak strength in spring with a center located over the northern Chukchi Sea.
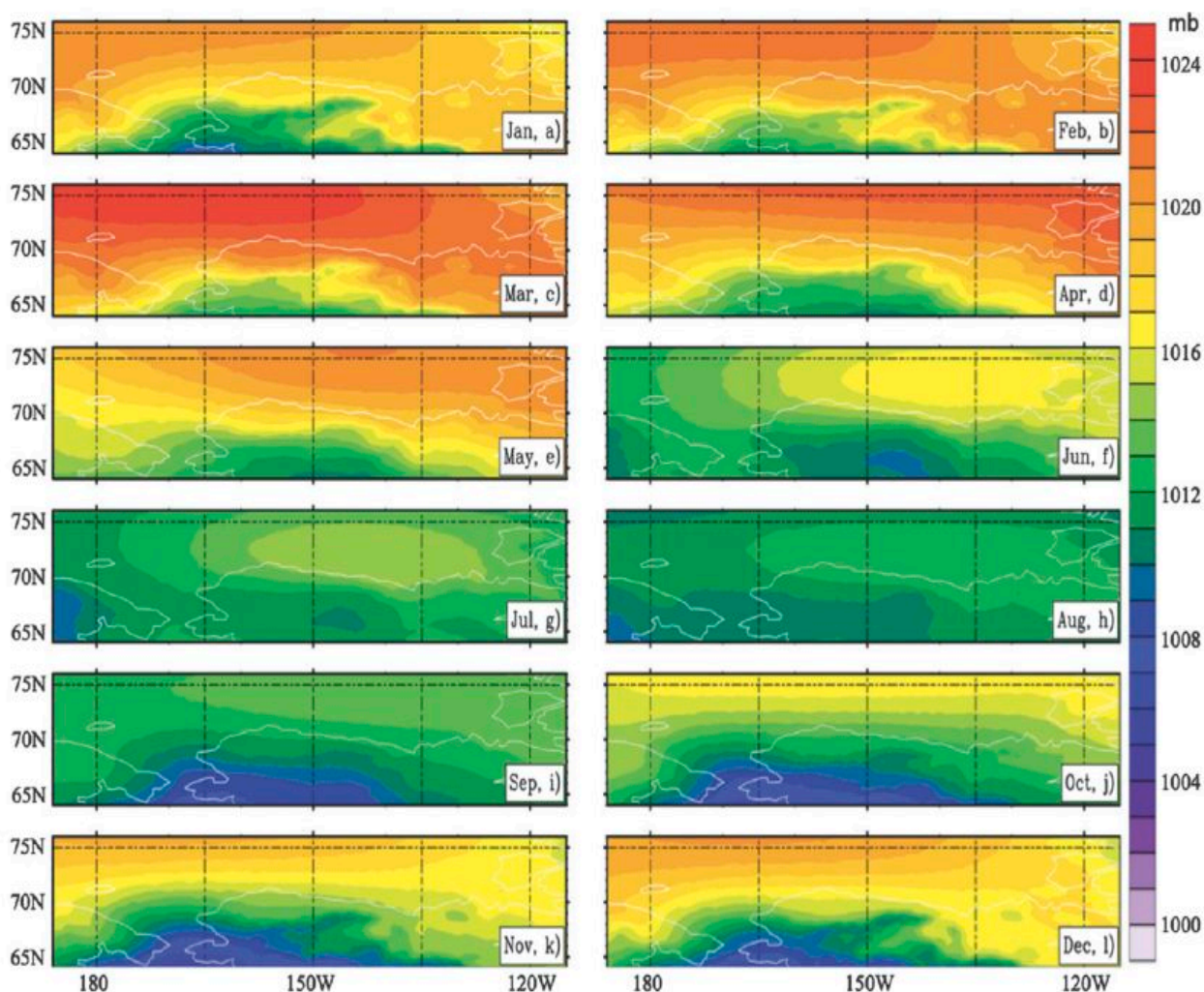
*Figure 14.* Monthly mean sea level pressure during 1979-2009.

Then the Beaufort high weakens through the summer months and moves eastward to the eastern Beaufort Sea. During the winter months, the Beaufort high begins to intensify and moves westward. On the other hand, it should be also noticed that the low system Aleutian low over the southern study area also displays a clear seasonal variability, peak in fall and flat is spring.

The frequency of wind directions from the other three quadrants (SEQ, SWQ, and NWQ) in the Chukchi-Beaufort Seas and North Slope is relatively low except for some areas characterized by mesoscale features, which will be discussed in section 3.5.2. For the whole

year the frequency of SEQ wind is around 10%-20% with little seasonal variation (not shown). The NWQ winds mainly occur over the northeast corner of the study domain (the Canadian Arctic Archipelago) during the cold season months (November-March) with a frequency around 30%-50%, due to the presence of the Beaufort high to the west of the Canadian Arctic Archipelago. The frequency of SWQ wind is less than 20% during most of the year except June through September, when an area with enhanced frequency (30%-40%) occurs to the north of the Chukchi-Beaufort Seas. The weakening of the Beaufort high during these months results in less NEQ winds, and then more SWQ winds occur due to the low system from the south (Figure 14). Similarly, the frequency of wind direction for the extreme winds (wind speeds at or above the 95th percentile wind speed) in each quadrant was also calculated (not shown). The persistence of the NEQ winds is also seen in the extreme wind events. Overall more than 60% of the frequency of extreme winds is from the NEQ direction for most of the study domain except for the eastern domain, where the highest frequency (>40%) of extreme winds is from the NWQ direction.

Similarly to the wind speed trend analysis, the frequency of wind directions from each quadrant (NEQ, SEQ, SWQ, and NWQ) was calculated and averaged for the entire study domain in each year and the linear trend was analyzed (Figure 15). A noticeable decreasing trend is seen in the NEQ winds and increasing trend in the SEQ winds. The trends in the NWQ and SWQ winds are flat. The strongest decreasing trend in the NEQ winds (~10% less in 2009 compared to 1979) occurs in January and November. A relatively strong increasing trend in the SEQ winds occurs in spring and fall. In particular, there are ~5% more SEQ winds in 2009 compared to 1979 during April and ~8% more during September. The frequency change of wind direction is probably the result of synoptic weather system changes, including strength and location movement, which is worth further investigation.
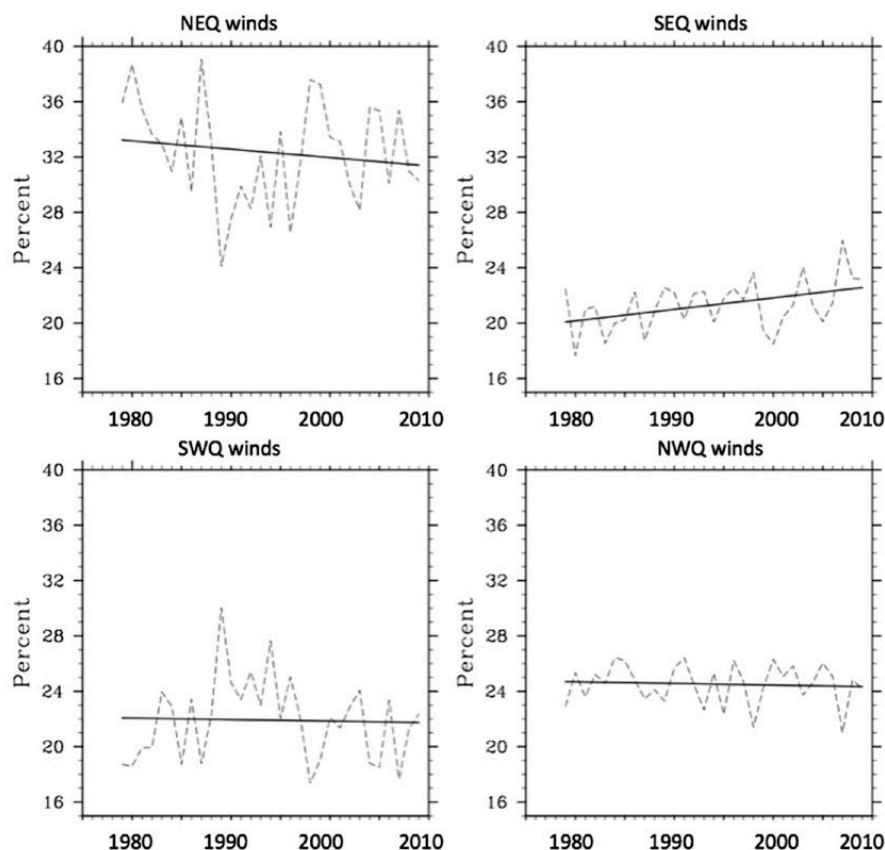
*Figure 15.* Monthly frequency of wind directions in each quadrant of NEQ, SEQ, SWQ, and NWQ and the linear trends during 1979-2009.

**3.5.2 Mesoscale features.** The study area features the Brooks Range in Alaska and the Chukotka Mountains is easternmost Russia.  The mountain dynamic modification of airflow could leave significant mesoscale fingerprints in the mountainous wind field.  The Froude number is a dimensionless number defined to describe the flow pattern over an obstacle (such as a mountain barrier) and calculated as the ratio kinetic energy (proportional to squared wind speed) to potential energy (proportional to stability times mountain height).  Thus, a Froude number smaller than the unit implies that the airflow is blocked from flowing over a mountain range because of either too high mountain elevation or too stable air.  The Arctic airflow in our

study domain is usually very stable, especially during the cold season months.  When the stably

stratified airflow approaches toward a mountain barrier, the Froude number of the airflow is

relatively small, which suggests that the flow cannot go over the mountain and will be blocked.

Then the airflow on the windward slope will slow down, and the original balance between

synoptic pressure gradient force (PGF) and the decreased Coriolis force (due to decreased win

flow) will be upset.  As a result a mountain barrier flow is generated to the low pressure of the

synoptic system due to relatively large synoptic PGF.  The flow is parallel to the longitude axis

of mountain and the Coriolis force then acts on it to generate a component directed toward the

mountain.  However, the flow cannot easily surmount the mountain and eventually a region of

mesoscale ridging against the mountain slope becomes established, and then the tendency for the

Corialis force to turn the flow toward the mountains will be balanced by the localized mesoscale

pressure gradient force (Bell and Bosart 1988; O'Conner et al. 1994; Harden et al. 2011).  Thus

as Bell and Bosart (1988) discussed, mountain barrier flow is a topographically induced,

mesoscale form of geostophic balance, but not in qeostrophic balance with the synoptic-scale

pressure gradient field.

As discussed in section 3.5.1, the dominant winds in the study area are from NEQ,

especially during the cold season months.  When the stably stratified NEQ winds, particularly the

NNE winds, approach the Brooks Range, the wind component perpendicular to the east-

northeast- to west-oriented mountain range is deflected and an SWQ mountain barrier wind will

be set up.  A similarly mountain barrier effect occurs along the Chukotka Mountains: when the

stable NEQ winds approach to the northwest- to southeast-oriented Chukotka Mountains, a

NWQ mountain barrier wind is formed.  This cyclonic deflection of wind direction along the

other mountain ranges has also bee extensively investigated (e.g., Parish 1983; O'Conner et al.

1994).  The mountain barriers winds are well depicted in the occurrence frequency of the SWQ

and NWQ wind during the entire cold season months (October-May) (Figure 16).
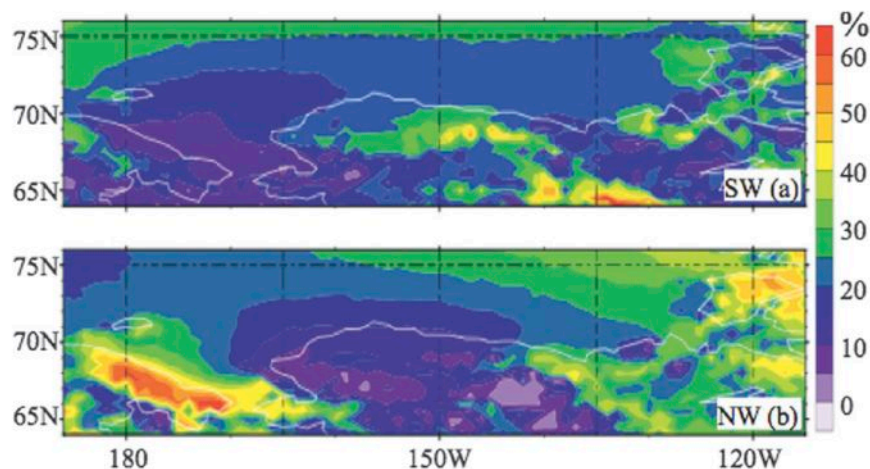


*Figure 16.*  Frequency of (top) southwest and (bottom) northwest winds during the cold months

(October-May) of 1979-2009.


Over the whole study area, the frequency of SWQ and NWQ winds is relatively small (<20%)

excepts for two anomalous areas along the Brooks Range and Chukotka Mountains, where the

occurrence frequency around 35%-50% occurs for the SWQ and NWQ winds, respectively.  It is

obvious that the frequency and area of SWQ winds along the Brooks Range are much smaller

that for the NWQ winds along the Chukotka Mountains, which is due to the orientation of these

two mountain systems and the prevailing wind directions.  Because of the orientation of the

mountain systems, only the NNE winds can be potentially deflected by the Brooks Range, and

the NNE, NE, and ENE winds can all be potentially deflected by the Chukotka Mountains.

Not only do the wind speeds have a diurnal cycle as shown in Figure 7, the wind

directions also demonstrate a diurnal variation due to the mesoscale sea breeze and mountain

valley breeze effects during the warm seasons whenever the land surface is snow free.  Figure 17
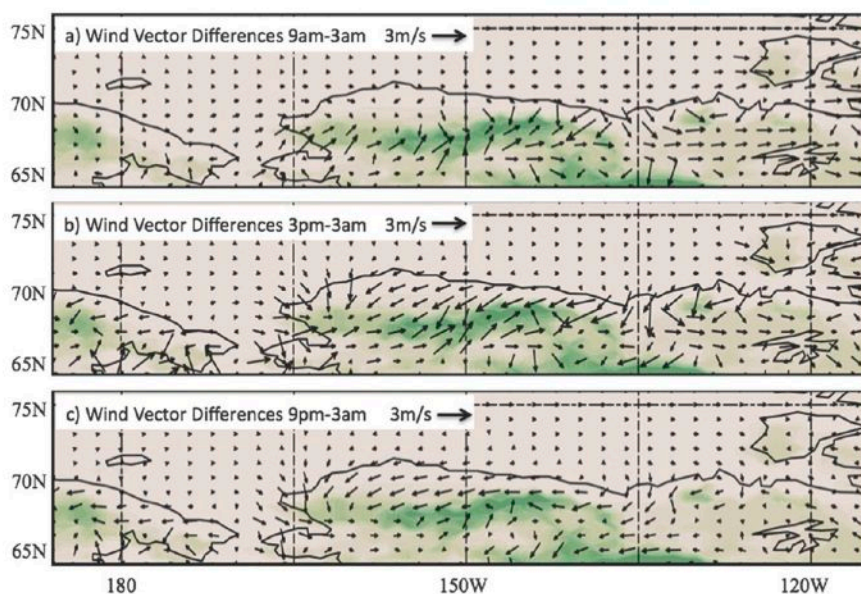
*Figure 17.*  Long-term mean wind vector differences from 0300 LT at (top) 0900, (middle) 1500, and (bottom) 2100 LT in July of 1979-2009.  Colors represent topography as in Figure 2.


depicts these mesoscsle breezes with the differences of long-term averaged wind fields between the warmer hours [0900, 1500, and 2100 local time (LT)] and the early morning hour hour of 0300 LT for July.  Mountain valley breeze along the Brooks Range starts as early as 0900 LT because of the polar day phenomena (24 h of daylight) in the study area (Figure 17 top).  As the land surface and mountain slope continue to warm because of stronger solar radiation, the valley breezes are further enhanced and a well-developed sea breeze is also present along the coast at 1500 LT (Figure 17 middle).  It should be emphasized that whenever a cross-shore wind begins to blow from the north due to the land-sea (ice) thermal contrast, the relatively large Coriolis effect at the high latitudes will generate an east wind component.  The stronger the cross-shore wind, the greater the east wind component.  As a result, northeast sea breezes are present along

the coast.  Because of the polar day phenomena, the sea breeze can continue to the late evening at 2100 LT (Figure 17 bottom).

## 3.6 Summary

The wind field climatology for the Chukchi-Beaufort Seas and Alaska North Slope regions was analyzed with the 3-hourly North American Regional Reanalysis (NARR) for the period of 1979-2009.  The result indicates that the wind speeds in the study area have a clear seasonal variability.  The relatively calm seasons are in spring and early summer.  Wind speeds over the Chukchi-Beaufort Seas gradually increase while the sea ice retreats back to the Arctic from summer to autumn.  The strength of winds over the Chukchi-Beaufort Seas reaches to the maxima of 6-9 ms$^{-1}$ for monthly average winds and 10-15 ms$^{-1}$ for monthly 95$^{th}$ percentile winds in autumn (September-October).  Wind speeds over land show a much weaker seasonality.  The seasonal amplitude of wind speed over the Chukchi Sea wind is around 6 ms$^{-1}$, which is double of the amplitude (3 ms$^{-1}$) over the Beaufort Sea.  The analysis of monthly probability density function (PDF) of the entire domain winds shows a consistent seasonality of more calm winds in spring and greater frequency of strong winds in autumn.

A diurnal variability of wind speed exists over land and sea ice-covered areas during the warm seasons.  The warm season's strong diurnal solar radiation forcing plus relatively small heat capacity over land and sea ice contribute to the diurnal variations.  Once the sea ice retreats significantly, the large water heat capacity dampens the diurnal fluctuation of winds over the open water.  The diurnal cycle over the land areas lasts for six months from April to September with the maximum cycle amplitude in June and July.  The diurnal cycle over sea ice lasts only 2.5 months from mid-March to May.

The 31-yr surface wind speed displays an increasing trend for both monthly mean and 95th percentile wind speeds from July through November. The strongest increase of monthly extreme winds (i.e., the 95th percentile wind speeds) occurs in October from 7 ms$^{-1}$ in 2009. The frequency of extreme wind events (i.e., occurrence of wind speeds above the 95th percentile winds) also shows an increasing trend and the greatest frequency increase in October again, 8% more extreme win events in 2009 than in 1979. Apparently the study area has a phenomenon of the "October Gale," with the greatest wind, the highest frequency of strong wind occurring in October. The northern study area is controlled by the Beaufort high during most of the year and the strength of the Beaufort high varies with season (Figure 14). On the other hand, the southern part of the study area is under the influence of the Aleutian low, which also displays a seasonal variability (Figure 14). In October, the Beaufort high begins to strengthen as well as the Aleutian low (Figure 14). These pressure patterns set up a strong pressure gradient over the study area and as a result the October Gale occurs. The significant retreat of sea ice in the study area during the most recent decade (e.g., Comiso et al. 2008; Polyakov et al. 2012) most likely contributes to the strong increasing trend in both wind speeds and frequency of extreme wind events. The wind direction climatology shows that the prevailing wind in the study area is from northeast with a frequency 40%-60% for most months, which is attributed to the dominant Beaufort high. Because of seasonal variations in the position and strength of the Beaufort high, the areal extent of the NE wind changes. The frequency of southwest and northwest winds is low (<20%) excepts for two anomalous areas along the Brooks Range in Alaska and the Chukotka Mountains in easternmost Russia where the frequency increases to 35%-50% during the cold season months. The extremely stable airflow plus the mountain barrier effect causes these mesoscale features in the wind direction climatology. During the warm seasons whenever

the land surface is now free, the mesoscale see/valley breezes develop along the coast and mountain range, impacting the area's wind field feature on a diurnal basis.  The frequency analysis of wind directions from each Quadrant (NEQ, SEQ, SWQ, NWQ) shows a decreasing trend in the NEQ winds and an increasing trend in the SEQ winds, indicating that the synoptic weather systems in the study area are changing, including the strength and location movements.

**CHAPTER 4**

**Surface Wind Field Climatology and Changes in CBHAR and Comparisons with ERA-I**

**Abstract**

An intercomparison of the surface wind field climatology and changes in the Chukchi-Beaufort

Seas High-Resolution Atmospheric Reanalysis (CBHAR) and the ERA-Interim (ERA-I) is

conducted for the period of 1979-2009.  Results show that the highest wind speeds (both mean

and 95th percentile) occur in the Chukchi Sea in November for both datasets.  ERA-I shows

higher 95th percentile winds than CBHAR, especially over ocean and sea ice points.  The

CBHAR clearly captures more detailed and stronger mesoscale features than the ERA-I,

especially over land and complex topography, notably the anomalous northwest winds in the

Mackenzie River valley and delta.  There is also a major difference in the wind speeds over the

coastlines, mainly due to the 10km grid spacing of the CHBAR vs. the much courser ERA-I.

Both datasets capture:

- The persistent northeast winds, mostly due to the persistent Beaufort High.

- Anomalous southwest winds along the Brooks Range and the anomalous northwest
  winds along the Chukotka Mountains in Siberia.  Both datasets capture

- Similar linear trends in wind speed, with the largest increasing trend in October.

- Similar linear trends in extreme winds, again with the largest increasing trend
  occurring in October.

However the ERA-I linear trends also capture higher extreme wind speeds consistent with

the monthly areal plots.

**4.1 Introduction**

In this chapter, the surface winds and associated parameters in the CBHAR and ERA-I datasets will be compared in term of their long-term (1979-2009) climatology, interannual variability, changes, and extremes.  There will also be a discussion of these two datasets's comparison to observations, station data, and QuikSCAT ocean surface winds.  Since the CBHAR is much finer in grid spacing (10km vs. 0.75° lat/lon) and 24 times daily data vs. 4 times daily.  This comparison helps to understand how the high resolution CBHAR performs differently from the global reanalysis ERA-I.

There is an imperative need to conduct this analysis for various applications, due to rapid environment changes and a lack of credible surface climate information in the study area. The CBHAR data enable us to carry out this analysis because its high resolution and well-captured regional physics, which can resolve finer scale processes caused by complex topography (i.e. the Brooks Range), variable sea ice and ocean properties, and their interactions. This regional analysis will add significant information to the understanding of the Arctic climate as a whole. Surface climatology of 2-m temperature, 10-m wind field, SST, and sea ice concentration/extent are analyzed.

**4.2 Analysis Approach**

A detailed climatology of the surface winds in CBHAR was analyzed, including construction of a long-term climatology and analysis of the linear trends in the surface wind speeds. Wind direction climatology was also analyzed. The monthly-average wind speeds were calculated by averaging over all output times for each month of the 31-year period. The monthly maximum wind speeds were determined by selecting the maximum wind speed for each month

over the 31-year period. The percentile wind speeds are calculated as discussed in the chapter 2.2 Methodology section.

The trends of monthly-average and 95th percentile wind speeds for the entire 31-year period were also analyzed with a linear regression approach, in which a positive value indicates an increase in wind speed and a negative value represents a decrease over the 31-year period. To investigate the variations of extreme wind events, defined as occurrences of wind speed greater than the monthly 95th percentile wind as calculated over the entire 31-year period, their frequency, expressed as a percentage, was calculated over a specified time period. For the wind direction climatology, the directions were first grouped into quadrants, and the monthly frequency of wind directions in each quadrant then calculated for each month over the 31-year period.

### 4.3 Surface Wind Speed Climatology in CBHAR and ERA-I

This section will compare the surface wind speeds (both average and 95th percentile) of the CBHAR dataset and the ERA-Interim dataset and both will be discussed and compared to the NARR results presented in chapter 3. There will also detailed discussion of the mesoscale features present, especially in the CBHAR dataset, which has 10km grid spacing vs. the 0.75° grid spacing of the ERA-I dataset.

To begin with, the monthly mean SLP over the study area from 1979-2009 is presented in Figure 18. The dominant weather features that affect the study area are the Beaufort High in the north and the Aleutian Low to the south with a clear seasonal variation shown with both of these systems. The Beaufort High reaches its peak in March at ~ 1024 hPa and is centered north of Barrow. By June, the Beaufort High weakens to ~1015 hPa and moves to the east, becoming centered in the middle of the Beaufort Sea. From July – September, the Beaufort High weakens

further, reaching a minimum central SLP of ~1010 hPa to 1012 hPa. The High strengthens again

from October to December and begins to move back to the north of Barrow with pressures

between 1017 hPa to ~1021 hPa. The Aleutian low impacts the study area in the south starting

in September, reaching its peak strength in November and then weakening. Overall, the CBHAR

successfully captures the climatological seasonal evolution of the synoptic-scale Beaufort high.

This climatological evolution matches that previously documented using NARR reanalysis data,

in which the same evolutionary trajectory was found (Stegall and Zhang, 2012).
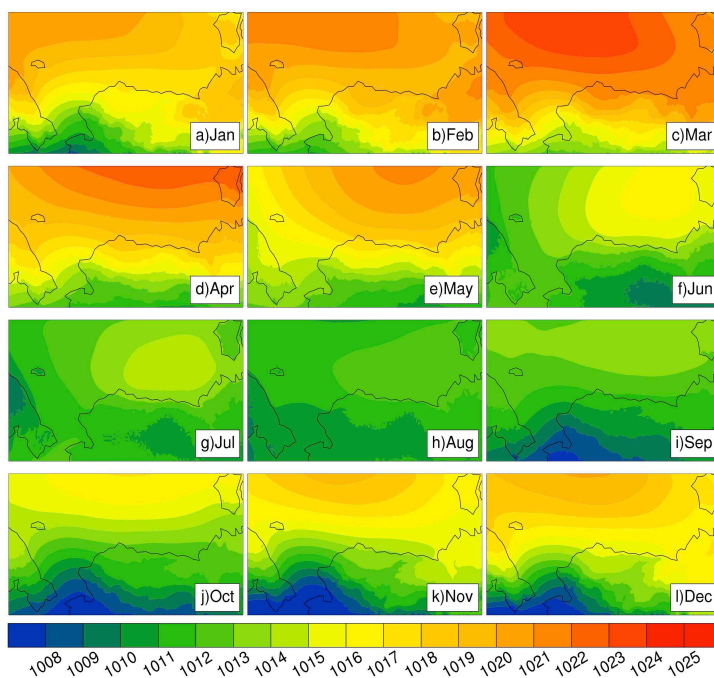


*Figure 18.* Climatological monthly mean sea level pressure (SLP) in hPa from 1979-2009 in

CBHAR.


Before a detailed comparison of CBHAR and ERA-I surface winds, a short discussion is

given of how CBHAR and ERA-I compare to observations (station data and satellite retrievals).

From chapter 2, a total of 262 station data were collected for the study area. From Zhang et al.,

(2013), the surface wind speed errors (measures by root mean square error (RMSE)) of CBHAR is smaller than ERA-I for all months of the year from 1979-2009 when verified with the observations. Also when each dataset is compared to station data, both coastal and inland stations, the CBHAR produces smaller RMSE. Both datasets were also compared with the QuikSCAT ocean surface winds. The results from Zhang et al. (2013) show that the CBHAR compared better than the ERA-I for the entire 31-year time period.

The long-term climatology of the surface wind from 1979–2009 includes analysis of the average wind speed, 95th-percentile wind speed, and wind direction. Figure 19 shows the 31-year average wind speed for each month of the year. Generally, the high climatological wind speeds are distributed from the Bering Strait to the shelf area of the Chukchi and Beaufort Seas, with the maximum monthly average wind speed occurring over the Bering Strait. The wind speed exhibits an obvious seasonality, with higher speeds in fall (SON) and winter (DJF) and lower values in summer (JJA).
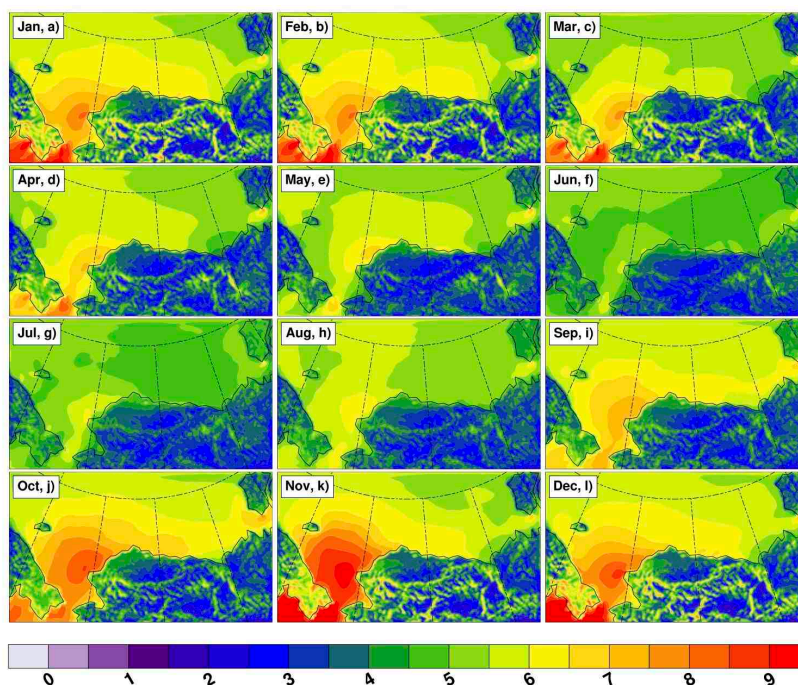


*Figure 19*. Climatological monthly mean wind speed (ms⁻¹) for 1979–2009 in CBHAR.

The highest wind speeds occur in November, reaching up to ~6 m s$^{-1}$ over the Beaufort Sea and ~9 m s$^{-1}$ over the Chukchi Sea, while the lowest wind speeds appear in June. Completing a parallel analysis using NARR (chapter 3, Stegall and Zhang, 2012), shows CBHAR has a consistent seasonality of surface wind speeds. However, the NARR winds show October to be the maximum wind speed month. When comparing with in-situ observations within the study domain, CBHAR presents a better estimate of the time of the maximum wind speed occurrence (Zhang et al. 2013).

When compared to NARR (chapter 3, Stegall and Zhang, 2012) the CBHAR wind speeds are consistently greater than NARR. From December through April, the CBHAR winds in Beaufort Sea are ~4 ms$^{-1}$ to 6ms$^{-1}$ where as the NARR wind speeds are below 4 ms$^{-1}$. During these same months the CBHAR winds in the Chukchi Sea are ~6 ms$^{-1}$ to 9 ms$^{-1}$, while the wind speeds in NARR are between 4 ms$^{-1}$ to ~6 ms$^{-1}$. For May through August the CBHAR wind speeds in the Chukchi Sea are ~4 ms$^{-1}$ to 6ms$^{-1}$, while NARR shows speeds below 4 ms$^{-1}$, except for in July and August when the speeds increase up to 6 ms-1 in the Chukchi Sea. For September through November, NARR has wind speeds increasing up to ~9 ms$^{-1}$ in the Chukchi Sea in October, While CBHAR has wind speeds increasing up to ~9ms$^{-1}$ in November in the Chukchi Sea. The Beaufort Sea during these same months in NARR are mainly ~5 ms$^{-1}$ or below, while for CBHAR the Beaufort Sea winds are ~6 m$^{-1}$ or 6.5 ms$^{-1}$ or below. According to Stegall and Zhang, (2012), NARR tends to underestimate surface winds along the coastal area. CBHAR indeed better captures the reality, mainly due to the usage of ERA-Interim as the forcing its generation. The ERA-Interim is considered a relatively better reanalysis in capturing

Arctic Climate. Figure 20 shows the ERA-Interim monthly average wind speeds and the speeds are also consistently greater than the NARR winds.
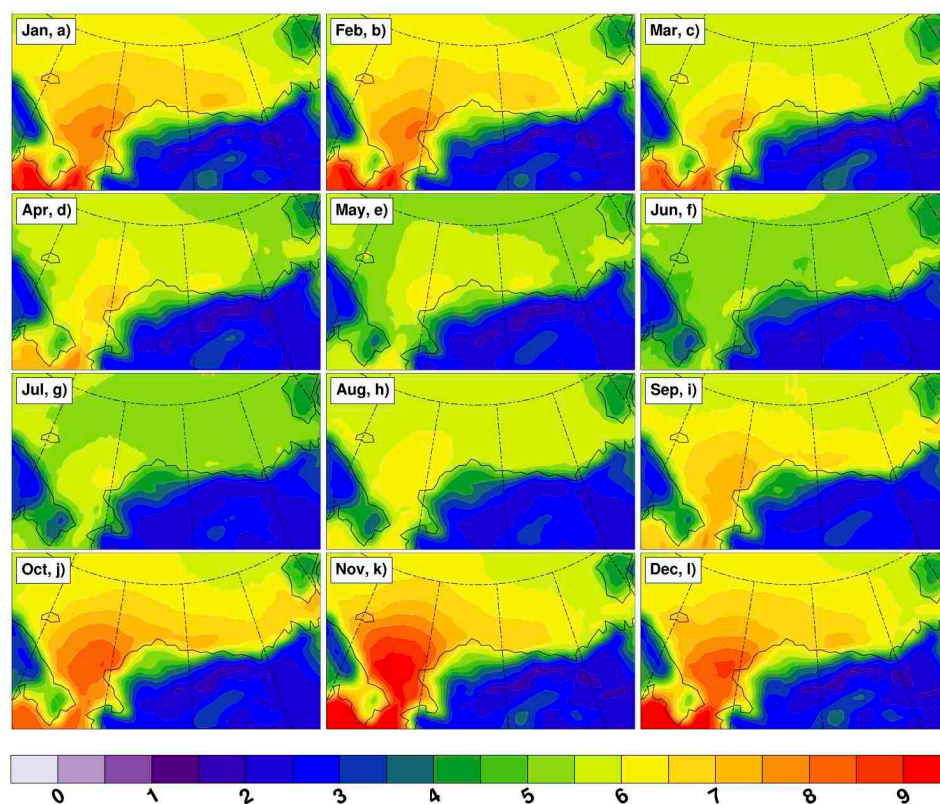


*Figure 20.* Climatological monthly mean wind speed (ms$^{-1}$) from 1979-2009 in ERA-Interim.

In comparison to ERA-I, CBHAR exhibits similar regional-scale seasonality in the surface wind field, with the added benefit that CBHAR is able to capture many high-resolution features and processes not present in the ERA-I (Figure 19). Monthly average surface wind speeds in ERA-I demonstrate the similar seasonality as in CBHAR. This is not unexpected, as ERA-I was used to drive the production of CBHAR. Wind speed patterns over the ocean compare favorably between ERA-I and CBHAR, though it is quite clear that CBHAR better captures topographically influenced wind features than does ERA-Interim. For example, during the autumn and winter seasons, higher wind speeds (~6 m s$^{-1}$) exist over the mountain ranges,

such as the Brooks Range and Chukotka Mountains in CBHAR. This is a signature of drainage and/or mountain downslope winds, features that are not present in the ERA-I data (Figure 20). Another difference between the two reanalyses is that ERA-I has consistently higher wind speeds over the coasts, with differences of about 2 m s$^{-1}$. Also the CBHAR data captures relatively high wind speeds over the Mackenzie River Delta and River Valley mainly from October through May, which is not present at all in the ERA-I data. This difference is most likely primarily due to the much coarser grid spacing present in ERA-Interim than in CBHAR.

An analysis of the 95$^{th}$ percentile wind speeds in CBHAR, given in Figure 21,
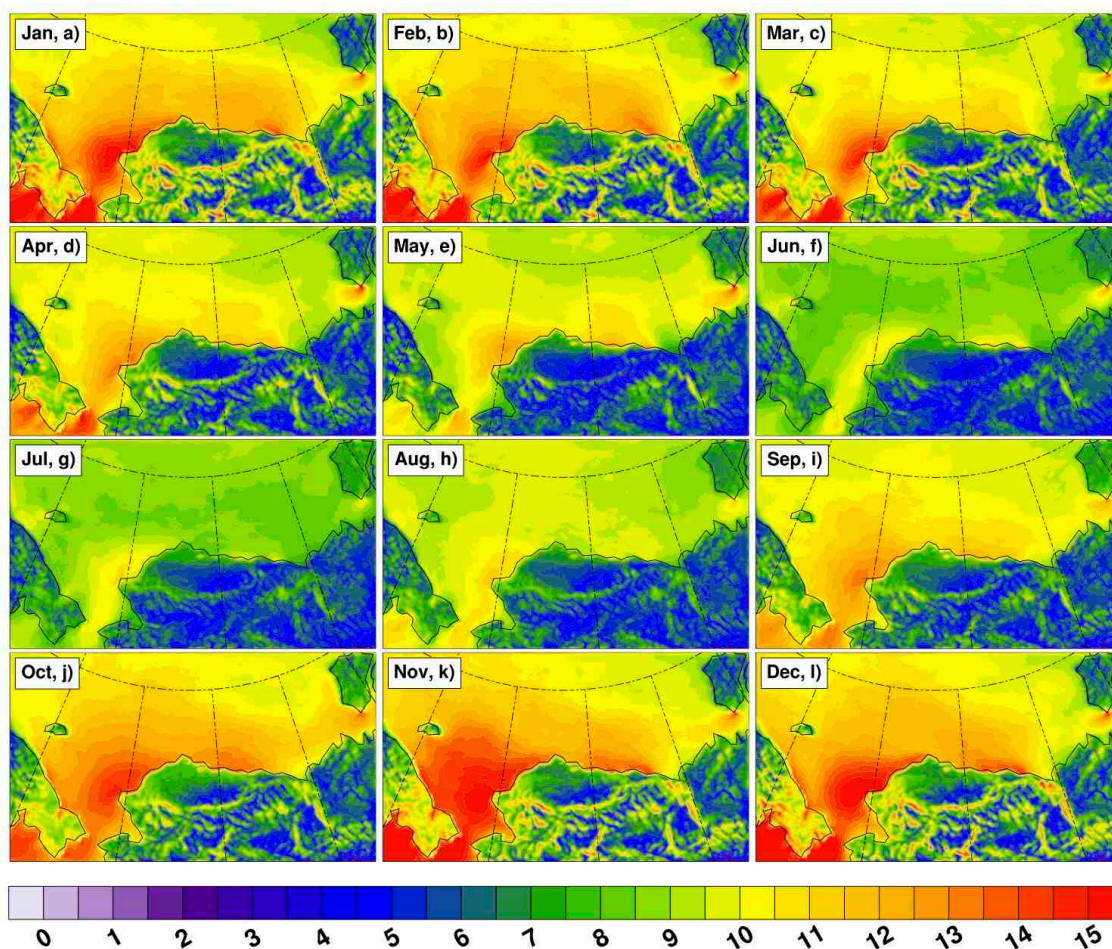


*Figure 21.* Monthly 95th percentile wind speeds (ms$^{-1}$) from 1979-2009 in CBHAR.

shows that relatively strong winds occur in the fall and winter (September through March), with the strongest in November. A similar geographic pattern and seasonal cycle are seen in the 95th-percentile winds as in the climatological means (Figure 19 vs. Figure 20). The strongest winds occur primarily over the Chukchi Sea with speeds of ~14–15 m s$^{-1}$. Wind speeds of ~12–13 m s$^{-1}$ can be seen in October over the Beaufort Sea, and primarily along the Alaska coast.

For comparison, Figure 22 shows the 95th percentile wind speeds using in ERA-I.
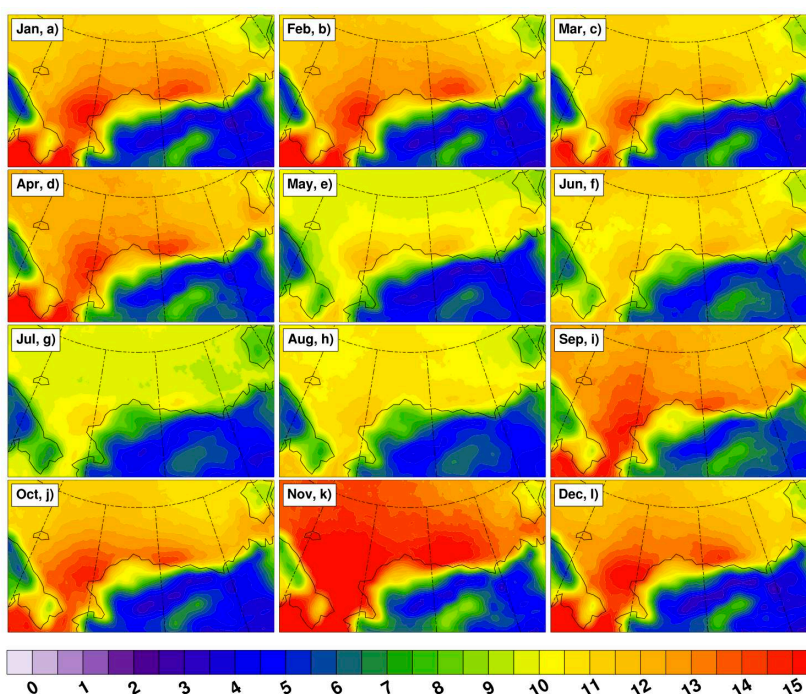


*Figure 22.* Monthly 95th percentile wind speeds (ms$^{-1}$) from 1979-2009 using ERA-I.

A very similar seasonality is present as that seen in CBHAR. A very evident difference between the two, however, is that the 95th-percentile winds in ERA-I are noticeably higher than those of CBHAR, particularly over the ocean, with a difference of around 2 m s$^{-1}$. The biggest difference is in November, where most of the offshore areas have wind speeds of ~13 m s$^{-1}$ to above 15 m s$^{-1}$ in ERA-I. In CBHAR, however, wind speeds of 13-15 ms$^{-1}$ are primarily limited to the Chukchi

and Bering Seas. Similar to the average wind speed, the CBHAR 95th percentile winds capture the relatively stronger wind speeds in the Mackenzie River Delta/Valley whereas the ERA-I does not capture this feature. As with the average wind speeds, CBHAR captures the drainage and mountain downslope winds during the autumn and winter months that are lacking in the larger-scale reanalysis, ERA-I.

To further understand the frequency of different wind speeds over the study domain, a probability density function (PDF) analysis was conducted for each month of the year in CBHAR (Figure 23).
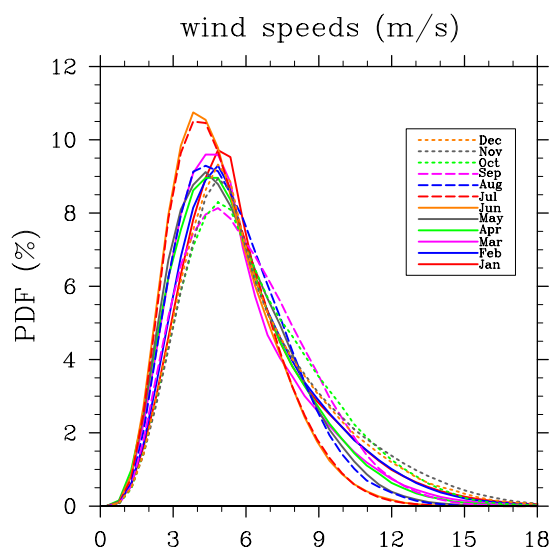


*Figure 23.* Probability Density Functions (PDFs) of the climatological monthly surface wind speed in CBHAR.

It was found that the peak frequency of any individual speed occurs in June and July for a wind speed of around 4 m s^{-1}. For most of the months, the highest frequency occurs for wind speeds ranging between 4–6 m s^{-1}. The frequency of wind speeds greater than 9 m s^{-1} increases in October and November. Figure 24 shows PDFs of the surface wind speeds over the entire year

and throughout the full 31-year time period for both CBHAR and ERA-I. CBHAR exhibits a

peak frequency at ~3.5 m s$^{-1}$, while the most frequent speed in ERA-I is ~2 m s$^{-1}$. However, the

higher wind speeds of ~7–13 m s$^{-1}$ exhibit greater frequency in ERA-I, which is consistent with

the findings that ERA-I tends to be greater than the CBHAR winds.
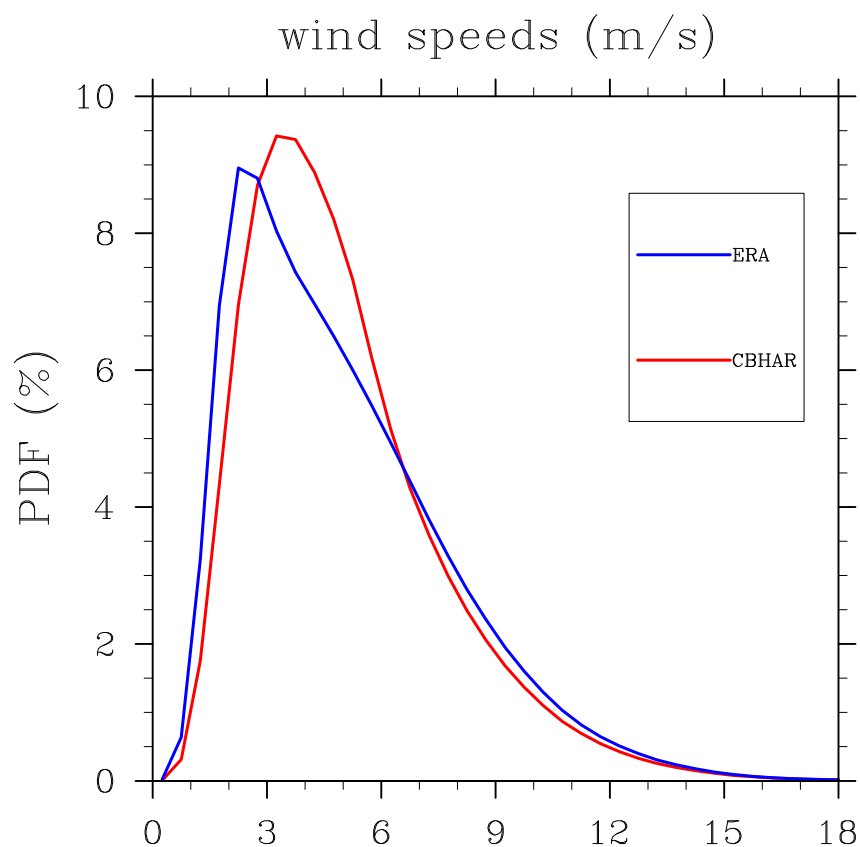


*Figure 24*. PDFs of surface wind speed for ERA-Interim (Blue) and CBHAR (red).

It is also relevant to investigate possible diurnal signatures in the wind speed. In this

analysis, the wind speeds are divided into those over land and ocean points. This allows an

analysis to be done to identify at which times of year diurnal signatures occur over the ocean as

well as land. Figure 45 (appendix A) shows the hourly CBHAR wind speeds averaged over the

study region for the 31-year period, separated into those over ocean (blue) and land (red). From late March through May, a clear diurnal signature exists over the ocean. This feature is significantly less pronounced, though still present, through mid-September, before disappearing for the remainder of the year. Over land, the diurnal signature begins in April and is clear until about mid-October. This diurnal signature agrees well with that seen by Stegall and Zhang (2012). However, the ocean wind speeds are much higher than the NARR wind speeds they observed.  This agrees with the discussion of the differential wind speeds between CBHAR and NARR given above. Another reason for this discrepancy in the domain-averaged speeds is that the study region used by Stegall and Zhang (2012) extended from the Bering Strait north to about 76°N. The CBHAR domain, on the other hand, extends farther north, but more importantly it also includes most of the Bering Sea and a small piece of the North Pacific Ocean, which include some of the highest average wind speeds in the study area (Figure 19 and Figure 21).  In addition, the CBHAR ocean wind speeds are much higher than those over land, whereas Stegall and Zhang (2012) found that in NARR, the ocean and land wind speeds were much more similar. This difference between CBHAR and NARR might be due to the treatment of sea ice in the NARR model vs. that in CBHAR. Also, as the wind speeds in the Bering Sea/Pacific Ocean are some of the highest in the region, when they are included in the averages shown in Figure 45 (in appendix A), the ocean wind speeds are increased relative to those over land. Figure 46 (in appendix A), similarly shows the 31-year 6-hourly average wind speeds in ERA-I. As with CBHAR, the ocean wind speeds are significantly higher than those over land. However, during the months of March through May the diurnal variability is weaker than in CBHAR, most likely due in part to the effect of only having data four times per day vs. the hourly data available in CBHAR, causing ERA-I to miss the diurnal maxima and minima.

**4.4 Surface Wind Direction Climatology in CBHAR and ERA-I**

To investigate the wind direction climatology, directions were first divided into quadrants, with 0–90° representing winds from the northeast (NE), 90–180° from the southeast (SE), 180–270° from the southwest (SW), and 270–360° from the northwest (NW). The monthly frequency of wind directions in each quadrant was then calculated for each month over the entire 31-year period. Figure 25 and Figure 26 highlights the monthly frequency of the NE winds in CBHAR and ERA-I respectively.
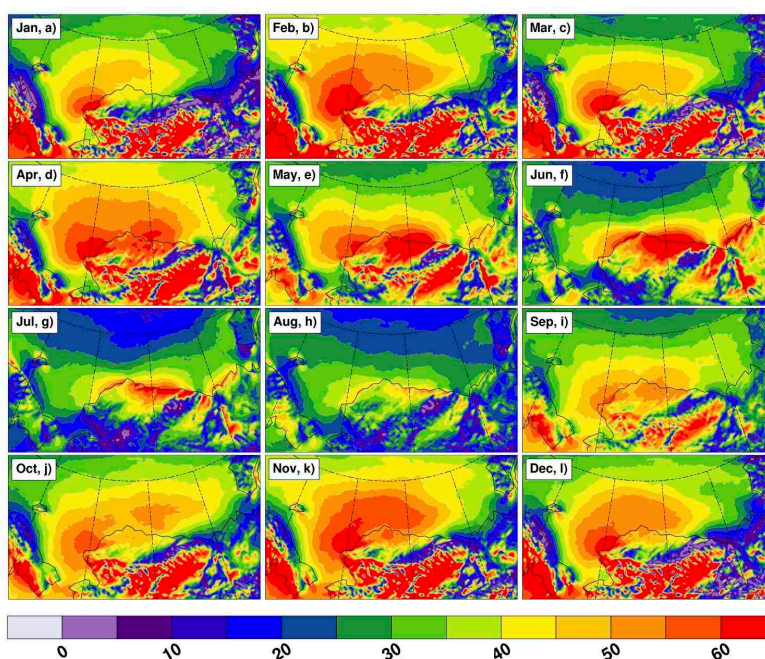


*Figure 25.* Monthly frequency (%) of northeast winds in CBHAR.

Northeast winds clearly prevail for most of the year within the study area, a result of the dominant influence of the Beaufort High. In the months of June to August, the frequency of the northeast wind direction decreases, primarily due to a weakening of the Beaufort High during summer. The frequency of northeast wind in ERA-I (Figure 26) is similar to that in CBHAR, including its seasonality. However, similar to what has been seen in the wind speed climatology,

ERA-I does not capture the topographic features nearly as well as CBHAR. The differences in the NE wind frequency over the Brooks Range and eastern Siberia are most likely the result of mesoscale circulations, such as mountain/valley breezes and the mountain barrier effect.
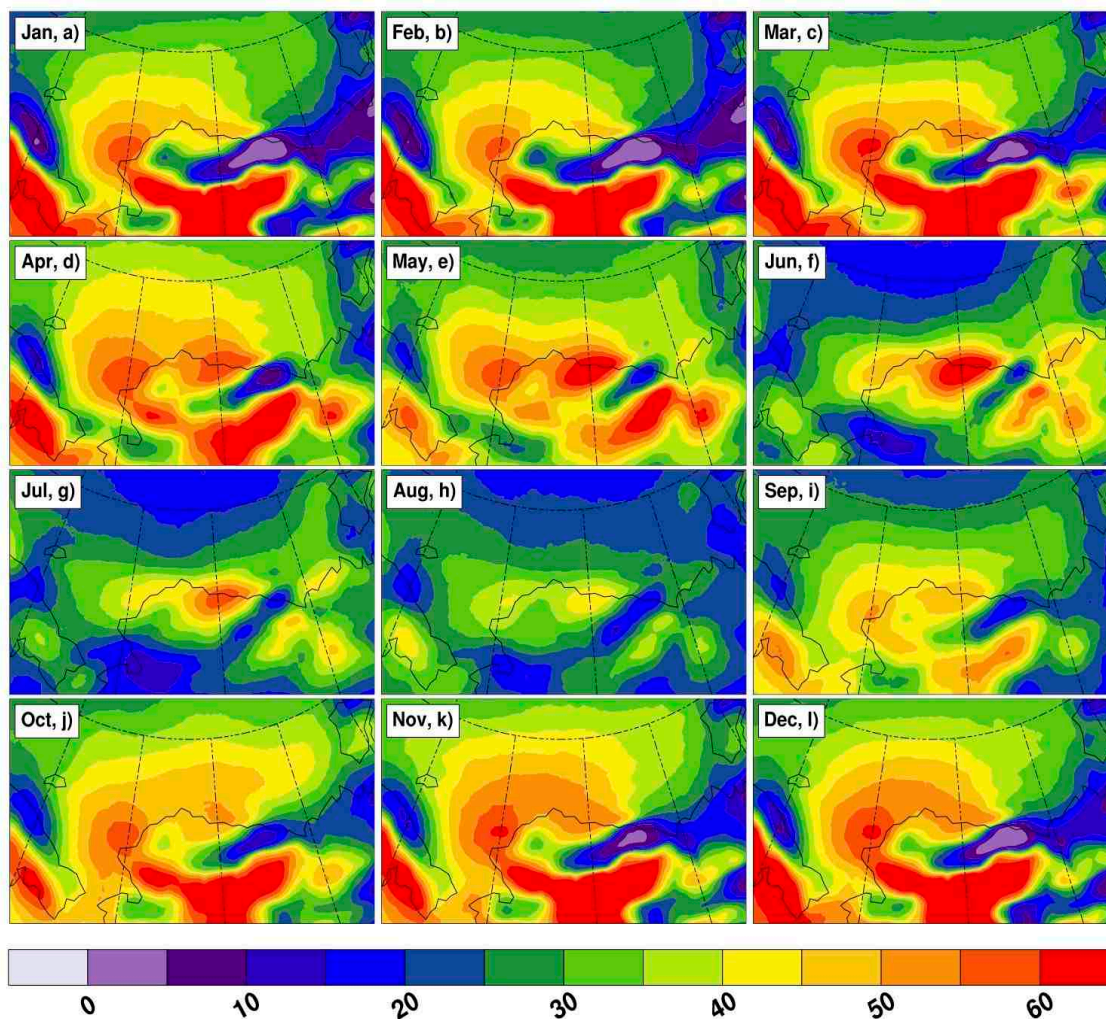


*Figure 26.* Monthly frequency (%) of northeast winds in ERA-I.

Although the northeast wind dominates the study area, wind from other directions can also be influential. Thus, southwest and northwest winds, averaged over the cold season including the months of January–May and October–December, were also analyzed (Figure 27).
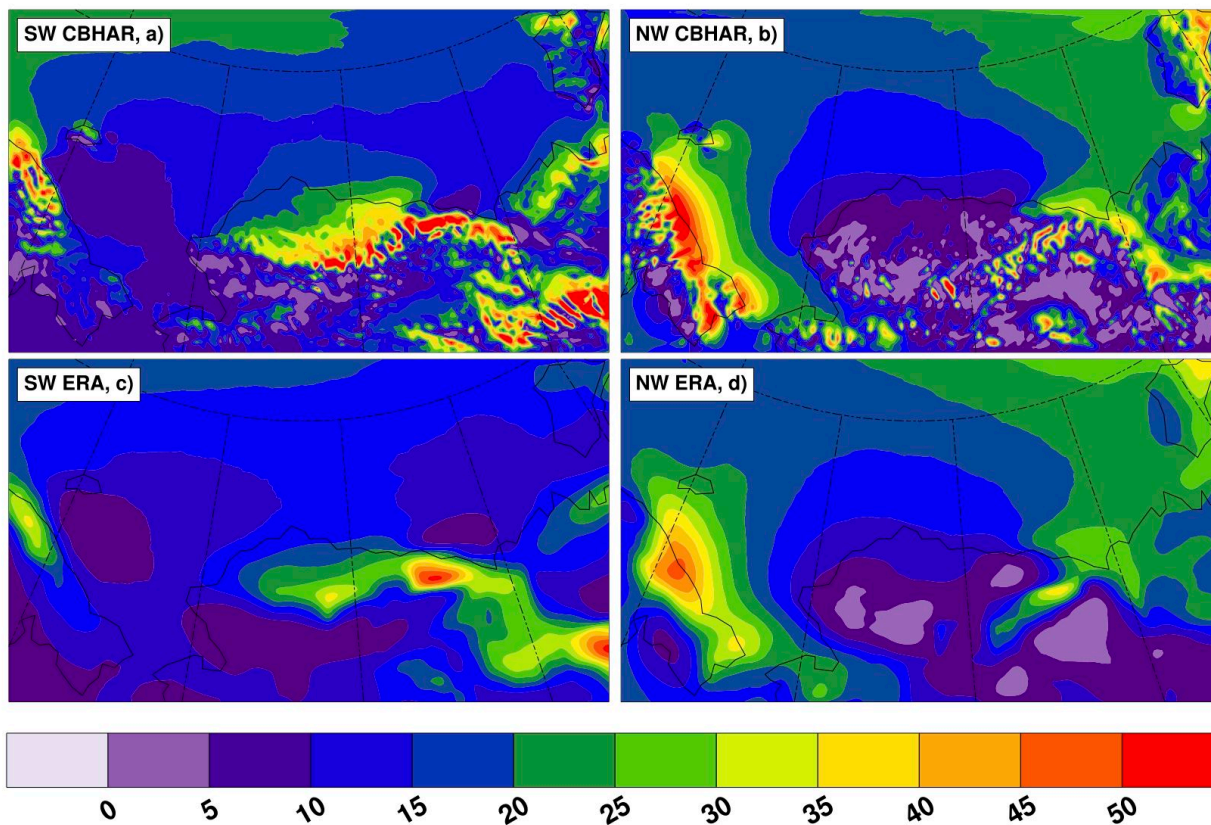
*Figure 27.* Southwest and northwest winds in CBHAR (a and b), and Southwest (SW) and northwest (NW) winds in ERA-Interim (c and d), averaged over the cold months January–May and October–December expressed as a percent (%).

This analysis reveals the presence of a high percentage of southwest and northwest winds, particularly along the Brooks Range in Alaska and along the Chukotka Mountains in eastern Siberia. Some of the anomalous southwest winds along the Brooks Range, particularly those around its eastern end near Canada, could be the result of cold-air damming against the mountain barrier. However, the southwest winds near the ridgeline of the Brooks Range and along its western section could represent mountain downslope winds that flow from the top of the range

toward the Arctic Slope. In a similar way, the southwest winds present on the northern slope of the Chukotka Mountains are also most likely due to the mountain downslope winds. The anomalous northwest winds along the Chukotka Mountains are the result of the mountain barrier effect.

A high frequency of northwest winds also occurs in the region around the Mackenzie River, including the Mackenzie Delta, in the northern Yukon. Small et al. (2011) also observed anomalous NW winds in this region. They conclude that these could be the result of NW surface winds overlain with NW 925 hPa geostrophic winds, and observed a strong correlation of surface winds with those from 1000 to 850 hPa, as well as a tendency towards lower stability, suggesting the mixing of momentum throughout the lower atmospheric column (1000 to 850 hPa). They also link this feature to synoptic SLP patterns, such as an anomalously strong high-pressure ridge over eastern Siberia and the Bering Sea, contributing to a pressure rise over the Brooks Range and cold-air damming that results in an alteration of the pressure gradient along the coast. The ERA-I data shown in Figure 27 c,d also captures the anomalous features seen in CBHAR. However, the frequency (percentage) of these features is lower by about 10%. In addition, the detailed mesoscale features seen over the mountains in CBHAR are not present in ERA-I. Over the Mackenzie River valley and delta, the anomalous winds are present, but lower in frequency (25–30% vs. 35–45%) and much less prominent.

## 4.5 Variability and Changes in Surface Winds

Based on the results of the above climatological analysis, the interannual variability and long-term changes in the CBHAR monthly surface wind speeds were further examined, with a simultaneous comparison made to ERA-Interim. Direct comparisons of monthly mean and 95th-percentile wind speeds between CBHAR and ERA-I are shown in (Figure 47 Appendix A) and

95th percentile wind speeds (Figure 48 in Appendix A), respectively. Both figures show that the trends in CBHAR and ERA-I are nearly the same, which is likely due to the CBHAR having larger winds (both mean and 95th percentile) over land and ERA-I having larger winds over ocean. Thus when analyzed over the whole domain, the two will balance out as in Figure 47. Again, ERA-I wind speeds, particularly the 95th-percentile winds, are slightly higher than those in CBHAR, which is consistent with the findings in Section 4.3. The trends in CBHAR and ERA-I are nearly the same and only the trend in October is significant at the 95% level using the t-test. Notable increasing trends of 0.27 m s$^{-1}$ decade$^{-1}$ and 0.26 m s$^{-1}$ decade$^{-1}$ exist for the October 95th-percentile winds in CBHAR and ERA-I, respectively.

Given their completely distinct geographic features, this interannual variability analysis was also performed over ocean and land areas separately, as shown for CBHAR in Figure 49 (Appendix A). Generally, ocean surface wind speeds are larger than those on land due to the lower surface friction typically present over water surfaces. According to the time series shown in Figure 49, both ocean and land surface wind speeds exhibit interannual variability throughout the year, with the amplitude varying from month to month. Superimposed on this interannual variability lie varying rates of upward and downward trends. However, only the trends in August and October over the ocean, and September and November over land are significant at the 95% level using the t-test. A pronounced increasing trend of 0.26 m s$^{-1}$ decade$^{-1}$ exists over the ocean in October.

The interannual variability of extreme surface wind speeds was also examined separately over ocean and land areas for CBHAR as shown in Figure 50, exhibiting very similar features to those of the monthly mean winds, except for an obviously larger wind speed. A stronger increasing trend of 0.48 m s$^{-1}$ decade$^{-1}$ occurs in the extreme surface wind speed over the ocean

in October. For comparison Figure 49 and Figure 50 also show the wind speed trends over land and ocean for the ERA-I data also. The trends are very similar to those in CBHAR, although the 95th-percentile wind speeds are higher, especially in November. Figure 51 displays the frequency of extreme winds, defined as the percentage of winds occurring above the 95th-percentile wind speeds for both CBHAR and ERA-I. Both datasets show very similar results. Clearly, the trends in Figure 51 are similar to the trends seen in the previous figures, with October showing the largest overall increasing trend. This agrees with the findings of chapter 3 and Stegall and Zhang, (2012), except that they found a positive trend in September as well as October in the NARR reanalysis.
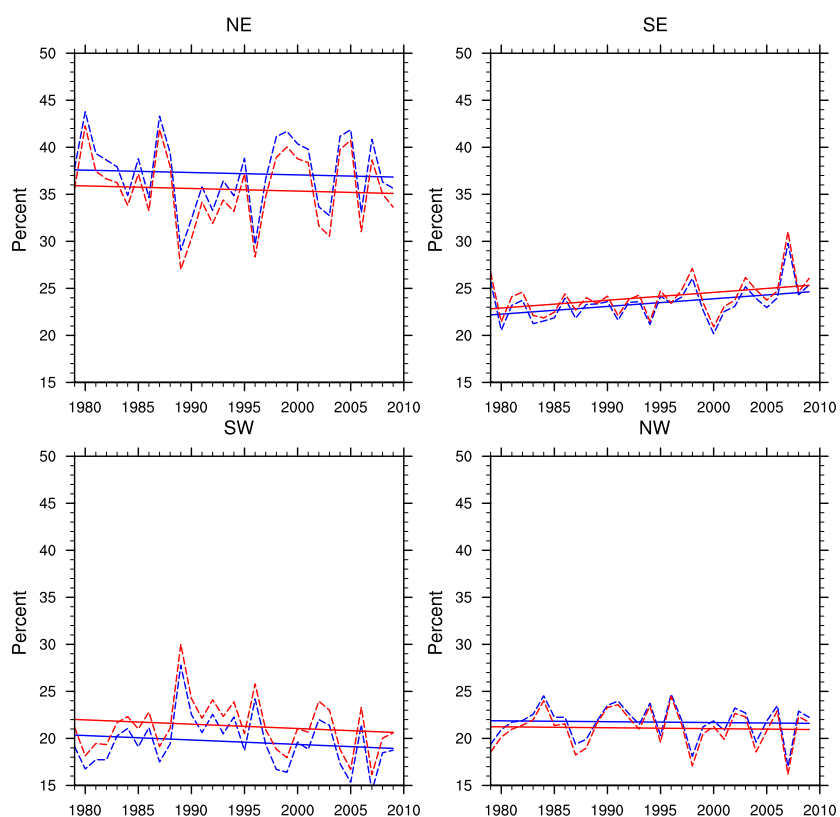


*Figure 28*. Frequency of monthly mean surface wind directions, grouped by quadrant, from 1979–2009 in CBHAR in blue and ERA-I in red.

This analysis was extended to include wind direction by computing the frequency of winds (Both CBHAR and ERA-I) originating from each quadrant and evaluating their interannual variability and long-term changes (Figure 28). The frequency of the wind from the northeast, northwest, and southwest directions exhibits year-to-year fluctuations, with just a slight decreasing trend. However, the frequency of the wind from the southeast has experienced a marked increase over time. Determining the reason for this increase requires further investigation into the impact of weather systems on wind direction in the region. The trends for the two data are very similar, except for the northeast where CBHAR is a bit higher and in the southwest where the CBHAR is a bit lower. The other two quadrants the datasets are nearly the same.

While the domain-averaged surface wind speed demonstrates a particular long-term trend, such changes may vary dramatically at different locations in the study area. To investigate the geographic distribution of surface wind changes, their linear trends were computed at each grid point in CBHAR (Figure 29). The results indicate that the largest decrease in monthly mean wind speed has occurred over the northern Chukchi–Beaufort Sea in January, with the minimum centered near the boundary of the two seas, well north of the Bering Strait. There is at the same time, however, a noticeable increase in wind speeds near the boundary of the Chukchi and Bering Seas in January. A notable decrease also appears over ocean areas in May and August, located primarily over the Beaufort Sea and the Canada Basin. By contrast, the largest increase in monthly surface wind speed has occurred over the entirety of the Chukchi and Beaufort Seas in October. In chapter 3 and Stegall and Zhang, (2012), a similar finding was reported, and they showed a high negative correlation between sea ice retreat and higher wind speeds, i.e., less sea ice is correlated with stronger winds.
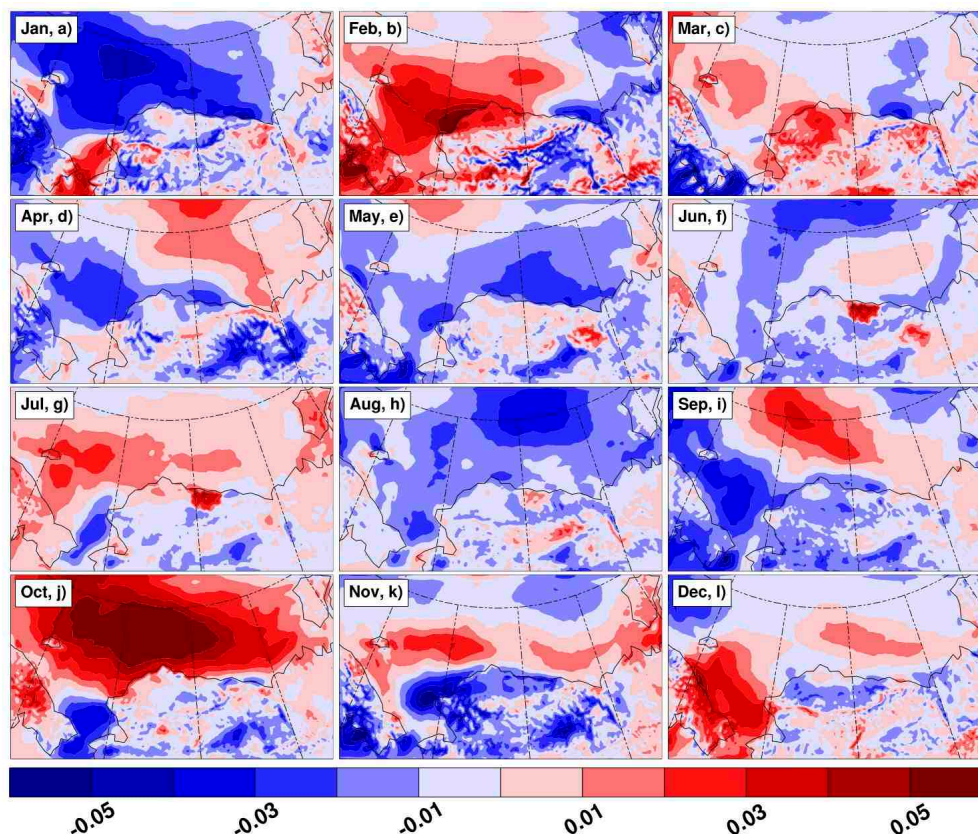
*Figure 29.* Linear trends in the monthly mean surface wind speed (m s$^{-1}$ year$^{-1}$) at each grid point in CBHAR. Positive values indicate an increase over the 1979-2009 period, and negative values indicate a decrease over the 31-year period.

A similar analysis for the 95$^{th}$-percentile wind speeds (Figure 30) shows some differences from the monthly-mean analysis, even though the domain-averaged features are shown to be quite similar. Unlike the monthly means, increasing trends dominate throughout the year and the decreasing trend in January is confined to a much smaller area. Increasing trends occur over nearly the entire ocean surface in February, March, May, July, and October. As with the monthly-mean analysis, the largest trend emerges in October, with a maximum increase over the Beaufort Sea.
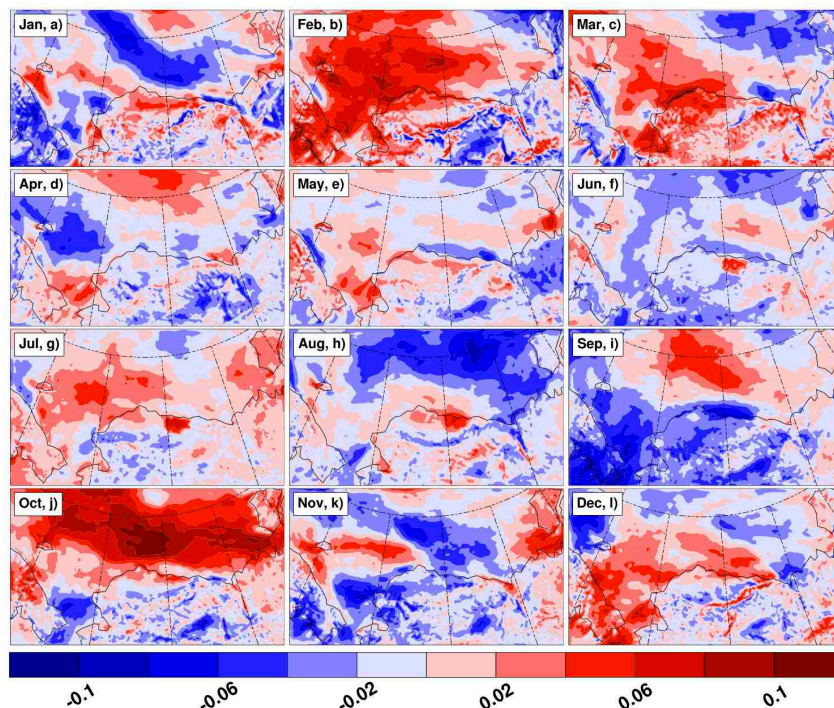
*Figure 30.* Linear trends in the monthly 95th percentile surface wind speeds (m s$^{-1}$ year$^{-1}$) at each grid point in CBHAR. Positive values indicate an increase over the 1979-2009 period, and negative values indicate a decrease over the 31-year period.

## 4.6 Variability and Changes in Sea Ice, 2m-air Temperature and SST

The wind field climatology (Section 4.3) has shown that the highest wind speeds in the study region occur during the autumn, particularly in November. This generally coincides with the time of year of the sea ice minimum and, consequently, the maximum amount of open ocean. Stegall and Zhang (2012) found that there is a high correlation between sea ice extent and wind speed. A detailed description of the sea ice concentration/extent present in CBHAR is therefore important. It is also important to investigate the sea ice trends given that the Chukchi/Beaufort Seas region is an area that has seen dramatic sea ice loss, particularly over the last decade or so (Jahn et al. 2012).
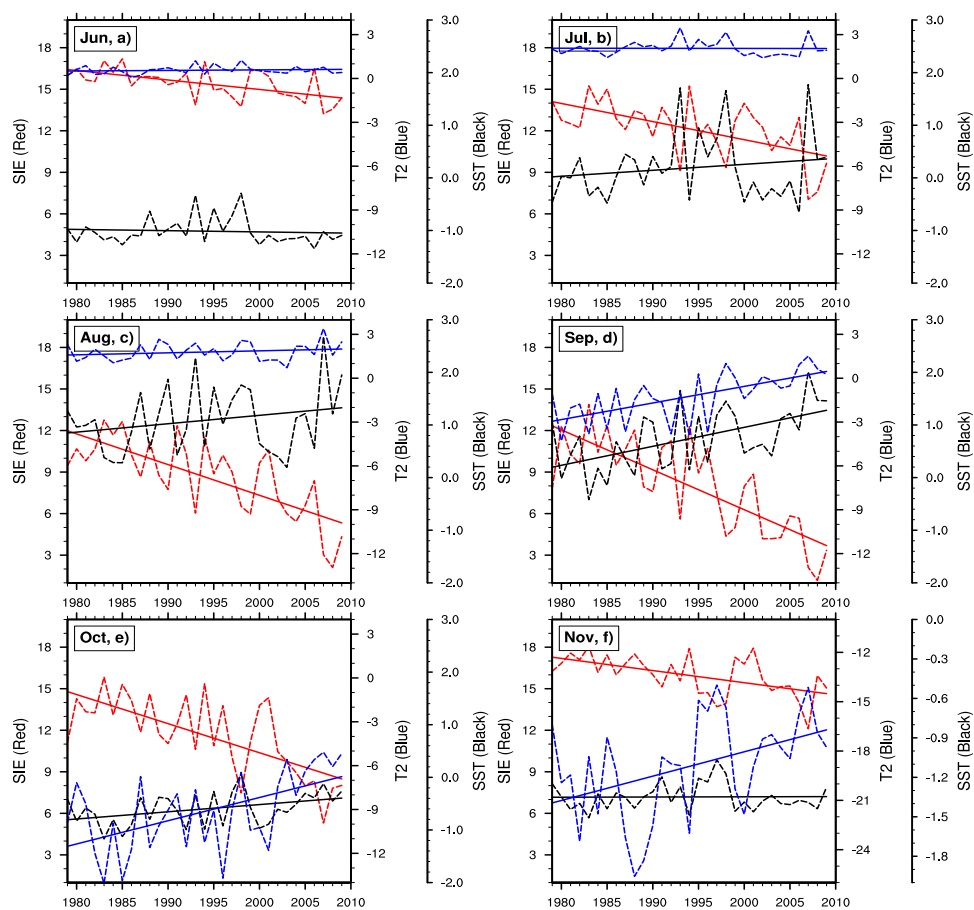
*Figure 31*. Monthly means and linear trends of sea ice extent (SIE, X $10^5$ km$^2$) in red, 2m-air temperature (ocean only) trend in blue, and SST trend in black for 1979-2009.

In this section, the trends in sea ice, 2-m air temperature, and SST are analyzed for the months of June through November, when sea ice extent exhibits large fluctuations (Figure 31). The 2m-air temperature from CBHAR and ERA-I were compared to station data similar to the wind speed (section 4.3). When compared to observation station data the CBHAR show slightly

better results of the 2m-air temperature than the ERA-I data. The sea ice data output in CBHAR

is the NASA Bootstrap SIC derived from the Scanning Multichannel Microwave Radiometer

(SMMR), thus a comparison to ERA-I is not done.

The decreasing trends in ice extent shown for the study region from July through October

are significant at the 95% confidence level using the t-test. The largest decreasing trend

($\sim 0.3 \times 10^5$ km$^2$ yr$^{-1}$) occurs in September, the month associated with the annual sea ice minimum.

A record low extent over the entire Arctic occurred in September 2007; however, for the study

region, the minimum extent occurred in September 2008. August and October also exhibit

dramatic decreases in sea ice extent ($\sim 0.2 \times 10^5$ km$^2$ yr$^{-1}$). Accompanying the strong decreasing

trends in sea ice during September and October, both 2-m air temperature and SST shows

significant increasing trends.

Figure 32 shows the linear trends in sea ice concentration (% yr$^{-1}$) for all months; shaded

colors are significant at the 95% level. The figure clearly shows that a substantial portion of the

domain has experienced significant sea ice loss for July through October. For September and

October most of the Chukchi/Beaufort Seas region displays a decrease in sea ice concentration.

The month of November shows a significant decrease in the Chukchi Sea vs. the Beaufort Sea.

Overall, for the autumn as a whole, the study domain exhibits a negative regression in sea ice

concentration, which is consistent with larger-scale trends as well as observations. The winter

months, especially January through April, show no real significant change in sea ice cover for

the 31-year study period. The area averaged 2m-air temperatures in CBHAR over ocean and

land demonstrate various interannual variability and long-term trends during 1979-2009 (Figure

52 in Appendix A). Clearly, September and October show large increases in temperature, with

the greatest increase over the ocean in October. This agrees with the observed temperature

increase as well as other studies showing similar results.
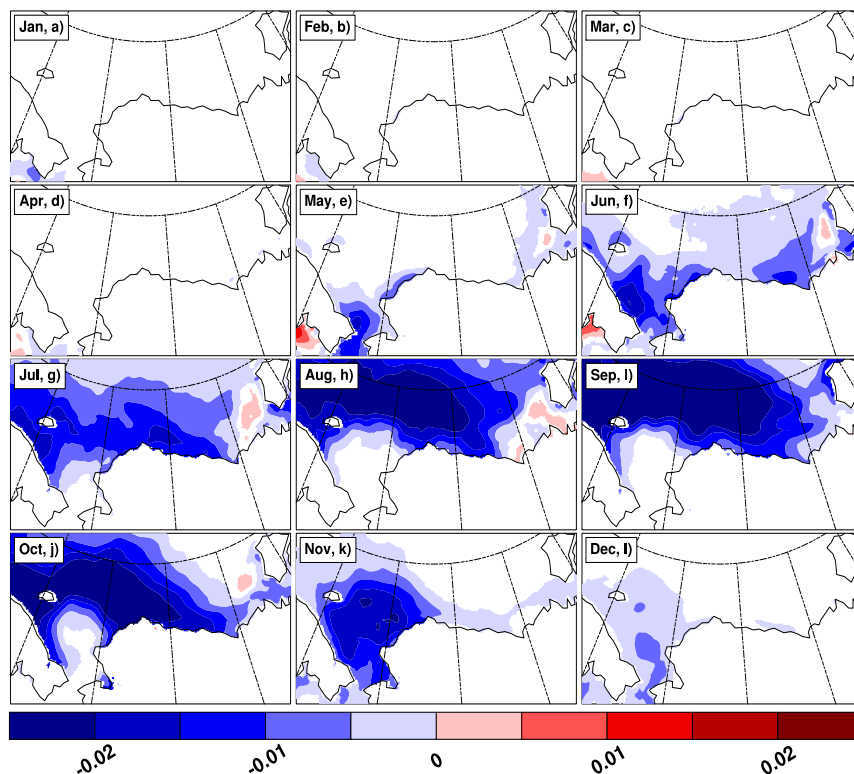


*Figure 32.* Linear trend of sea ice concentration (% per year) for all months from 1979-2009.

Contours plotted are significant at the 95% confidence level. Positive values indicate an increase

over the 1979-2009 period, and negative values indicate a decrease over the 31-year period.

.

Figure 33 displays the 2m-air temperature linear trend (°C yr$^{-1}$) at each grid point in

CBHAR for all months of the year. Colors shown are significant at the 95% confidence level.

The most obvious feature is the large area of increasing temperatures in the Chukchi–Beaufort

Seas from September through December. The summer months (May–August) show little trend

over most of the region.
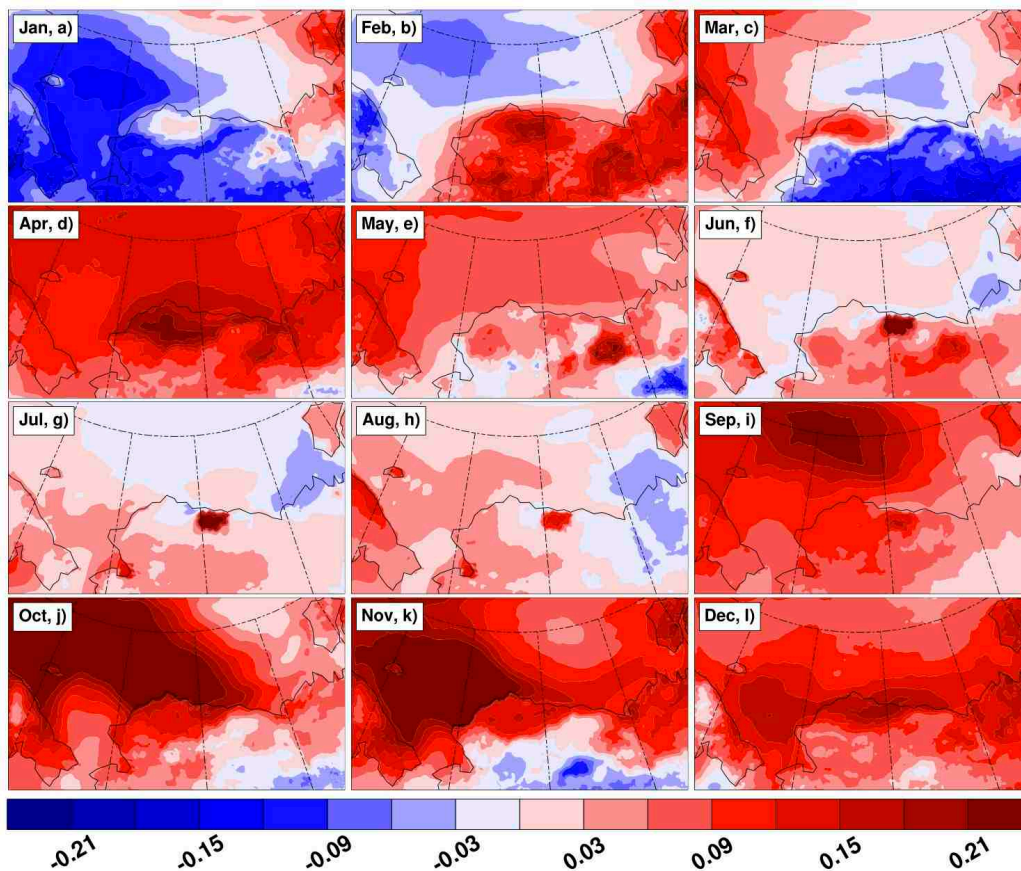
*Figure 33.* Linear trend of the 2m-air temperatures for all months from 1979-2009. Contours plotted are significant at the 95% confidence level. Positive values indicate an increase over the 1979-2009 period, and negative values indicate a decrease over the 31-year period.

Figure 33 and Figure 52 (Appendix A) indicate the presence of much warmer air in the latter part of the 31-year study period. This warmer air is one potential cause for the substantial sea ice loss in the region. Another important variable to analyze is the SST in areas of open, ice-free ocean. Warmer SST may contribute to sea ice loss through redistribution and mixing by ocean dynamic processes. Figure 31 above shows the long-term SST trend for the months of June through November. The largest increasing trend occurs in September, while the other three months show weaker, but still positive, trends as well.
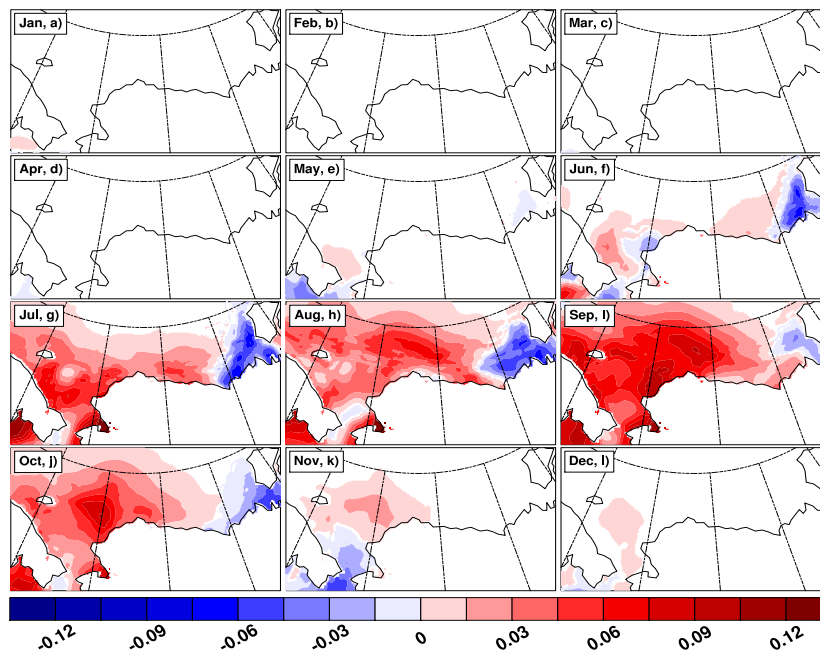
*Figure 34*. Linear trends of SST for 1979-2009.  Contours plotted are significant at the 95% confidence level.  Positive values indicate an increase over the 1979-2009 period, and negative values indicate a decrease over the 31-year period.

Figure 34 shows the SST linear trends at each of the ocean grid points in CBHAR. Clearly, SSTs have increased over most the study region, with the broadest area of increase occurring in September. Although there are large areas of increasing SSTs in July, August, and October, the areas of warming are not as large as the maximum area present in September. One very noticeable feature of the trends is the decreasing SST in the southeastern Beaufort Sea and off the coast of Canada. This could be related to the outflow of fresh water from the Mackenzie River/Delta and may be worth further research.

**4.7 Summary and Discussion**

The surface climate analysis using CBHAR shows that the wind speeds (monthly mean and monthly 95th percentile) exhibit a clear seasonality, with the lowest wind speeds in the spring

months and the highest wind speeds in the autumn.  The ERA-I captures a similar seasonality as CBHAR, with highest winds in the autumn months.  However the ERA-I 95th percentile winds are consitently higher than the CBHAR winds.  When both datasets were compared to station data and QuikSCAT ocean surface winds, the CBHAR performed better with less RMSE.  Thus the CBHAR winds are a better representation of the climate.

The wind direction climatology shows that winds from the NE quadrant are the most frequent in the region, except during the summer months when the Beaufort High tends to weaken. The direction climatology also captures mesoscale features, including anomalous SW winds over the Brooks Range, anomalous NW winds over the Chukotka Mountains in eastern Siberia, and anomalous NW winds over the Mackenzie River valley in Canada, particularly during the cold season months. These anomalous winds could be the result of cold-air damming, resulting from a mesoscale force imbalance between the pressure gradient and Coriolis forces, as well as the downslope mountain breeze. The linear trend analysis of the wind speeds shows that the largest increasing trend occurs in October. These results are consistent between CBHAR and ERA-Interim, even though CBHAR employed different assimilation technology and assimilated different data. This suggests that CBHAR accurately captures changes in the large-scale surface climate. Sudden changes in trends due to a change in technology (e.g., the introduction of QuikSCAT or MODIS observations), such as discontinuities in the trend data or sudden increases or decreases in the trends are not present. Both the climatology and trends of the winds in CBHAR agree well with ERA-I data, indicating that the assimilation of different types of data as technology changed over time was handled correctly in CBHAR.

# CHAPTER 5

## Wind-SST-Ice Relations in the Marginal Ice Zone of the Chukchi-Beaufort Seas

**Abstract**

The newly generated Chukchi-Beaufort High-resolution Atmospheric Reanalysis (CBHAR) is used to analyze the relation between surface wind, sea surface temperature (SST) and sea ice coverage in the marginal ice zone of Chukchi-Beaufort Seas for September and October when both open water and sea ice are present with compatible percentages. The CBHAR surface wind field compares well to global reanalysis (ERA-Interim) with add on benefits capturing additional spatial details, particularly over complex coastal and terrain areas. Cross-correlation between surface wind and SST anomalies shows there are negative correlation for open water and less-ice covered areas and positive correlation over sea ice and more-ice covered areas, the significance of correlation is above the 95% level. Composite analysis of positive and negative wind speed anomalies and associated radiation forcing reveals that with positive (negative) wind speed anomalies there are more (less) clouds, stronger (weaker) downward longwave radiation, and weaker (stronger) downward shortwave radiation, indicating that strong winds during the study period are associated with storm activities. Warmer SST associated with positive wind anomalies (more sea ice covered areas) is thus the result of enhanced longwave radiation forcing brought by the storm activities. On the other hand (less sea ice cover and open ocean), strong thermal gradients also exit between the open water and ice-covered areas, which generate strong cold air advection when the surface winds are strong, plus relatively strong decrease of cloudy-sky solar radiation, a negative relation between winds and SST occurs over the water adjacent to the ice.

**5.1 Introduction**

With potential energy industry development in the Chukchi/Beaufort Seas, the potential threat of oil spills exists. Should a spill occur, the surface wind field is a crucial parameter for accurately predicting spill transport (Reed et al. 1999). As such a thorough mesoscale meteorology study over the Chukchi/Beaufort Seas region has been conducted (Zhang et al. 2013) and the analysis of the area's wind climatology indicates an intensified surface wind over recent decades during fall when minimal sea ice coverage presents (Stegall and Zhang, 2012). The strengthened surface winds concur with the fast decline of sea ice in the Chukchi/Beaufort Seas (Comiso 2012). Stegall and Zhang (2012) also found significant correlation between sea ice concentration (SIC) and wind speed.

Prior studies have shown that a strong relationship exits between sea surface temperature (SST) and surface wind speed. O'Neill et al. (2010) and O'neill (2012) found a positive linear relationship between wind speed and sea surface temperature (SST) in various study areas including the Kuroshio in the Pacific Ocean, the Gulf Stream, the South Atlantic Ocean, the Agulhas Return Current, the North Atlantic Gulf Stream and the Eastern Equatorial Pacific Cold Tongue. Sampe and Xie (2007), and Chelton and Xie (2010) also noticed stronger winds speeds with warmer SST's in the Agulhas Return Current. These studies have mainly focused on warmer oceans such as The Gulf Stream, or the Equatorial Pacific Ocean where no sea ice is present and can be mainly characterized as heat sources over a long time period. However the Chukchi/Beaufort Seas are under the influence of Arctic sea ice on a seasonal basis and the areas are generally characterized as heat sinks (Wang and Key, 2005). Over a partially ice-covered ocean, sharp temperature gradients usually exit between ice and open water. When the winds blow from ice to open water, or from open water to ice, there will be a substantial cold or warm

air advection. Then will the strongly correlated SST and wind speed hold the same positive relationship over the Chukchi/Beaufort Seas as over a warmer ocean, such as the Gulf Stream and the South Atlantic Ocean? To answer this question, the relation between surface winds, SST, and sea ice and the mechanisms impacting the relation over the Chukchi/Beaufort Seas where both open ocean and sea ice are present will be explored with a newly developed Chukchi/Beaufort Seas High-Resolution Atmospheric Reanalysis (CBHAR) (Zhang et al. 2013).

The generation of high-resolution (10 km) regional reanalysis CBHAR allows researchers to better understand the environmental changes over the Chukchi/Beaufort Seas region of the Arctic, an area that has been subject to thinning of sea ice and a dramatic reduction in ice coverage, faster than model projections, especially in September (Stroeve et al., 2012). With less sea ice and more open water, a better understanding of the atmosphere-ocean-ice interaction is necessary, especially with regards to surface wind, SST and sea ice. The goal of this study is to investigate the relation among the wind speed, SST, and ice in the Chukchi/Beaufort Seas during the months of September and October from 1979-2009. The sea ice minimum generally occurs in September, thus there are compatible percentages between open water and ice-covered areas during the study period. Atmospheric conditions such as surface air temperature, and radiation forcing will be used to explore the physical interpretation of the wind speed, SST, and ice relation in the Chukchi/Beaufort Seas region.

The data used in this chapter is the CBHAR data and the methodology used for this study is described in chapter 2. Using the composite analysis described in chapter 2, the atmospheric conditions such as 2m-air temperature and temperature advection, wind direction, long wave and short wave radiations, as well as cloud cover will be investigated under high wind and low wind anomalies separately.

This chapter will be organized in the following way. Section 5.2 will be a study of the relation among surface wind, SST, and sea ice. Section 5.3 will be the composite analysis exploring the mechanisms responsible in the relation, and section 5.4 presents a summary and conclusions.

**5.2 Wind-SST-Ice Relations**

From prior results, Chapters 3, 4, and Stegall and Zhang (2012), surface winds in the study area have been enhanced significantly and especially during the period of September and October, which may be caused by the retreat of sea ice cover in the area. The relationship between winds and SIC in CBHAR is further explored by applying the method discussed in chapter 2. Binned scatters of wind speed anomalies are plotted as a function of SIC anomalies. Figure 35 below shows the wind speed-SIC relation in CBHAR.
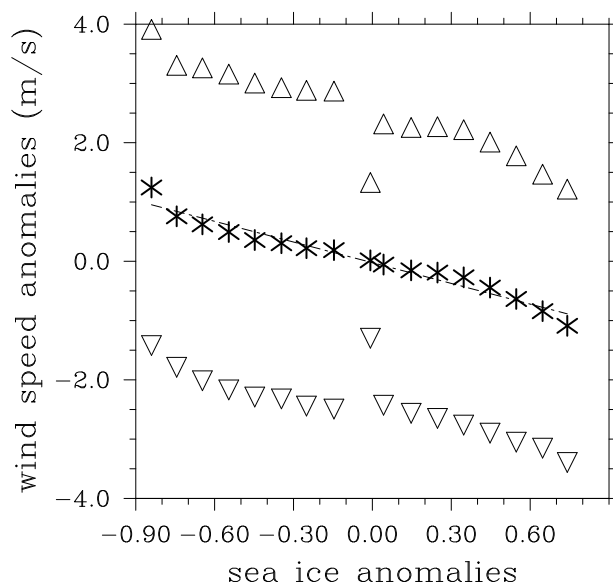


*Figure 35.* Binned wind speed anomalies as a function of binned SIC anomalies. Triangles are +/- one standard deviation. Dashed line is the regression.

There is a clear inverse linear relationship as expected. This further confirms the significant negative correlation between wind speed and sea ice in Stegall and Zhang (2012). The correlations of wind speed anomalies to SIC anomalies are -0.98 for the CBHAR and are significant at the 99% level. These results further suggest that less sea ice (more open ocean) the higher the wind speeds.

With more open ocean leading to higher wind speeds, it is evident there is need to further explore the relationship between surface winds and SST anomalies. The relation among the anomalies is investigated with three groups of SIC ranges from 0% (open water area only), to 1%-19% (slightly ice-covered area), and 20-100% (moderately to mostly ice covered area). This analysis by SIC groups can allow the consideration of sea ice influence on the relation between surface winds and SST.

Figure 36 shows the binned scatter relationship between surface winds and SST anomalies in CBHAR.
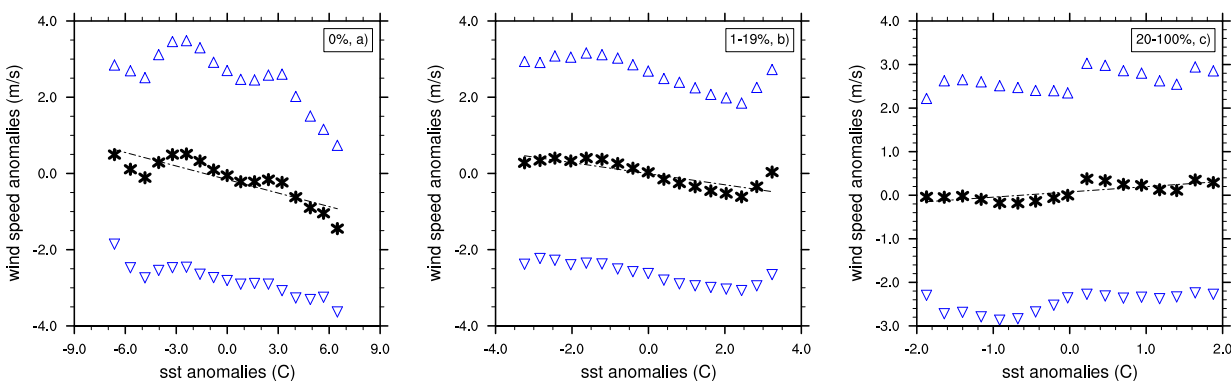


*Figure 36.* Binned wind speed anomalies as a function of binned SST anomalies for open water (a, 0% SIC), slightly ice-covered area (b, <20% SIC) and moderately to mostly ice covered area (c, >20% SIC). Triangles are +/- one standard deviation. The dashed line is the regression.

A clear inverse linear relationship exists for the open water and slightly ice-covered areas. The correlations of wind speed anomalies and SST anomalies over areas with 0% SIC and 1%-19% SIC are -0.85 and -0.83 respectively and significant at the 99% level. Over areas with 20%-100% SIC, the correlation is 0.73 and is also significant at the 99% level. At ~20% SIC the relationship changes from an inverse relationship to a positive, though relatively flat due to small variance in SST under sea ice cover (Figure 36). Of course with more sea ice (increasing SIC) the atmosphere and ocean will become less coupled.

The binned analysis above demonstrates that ~20% SIC there is a change from an inverse linear relationship to a linear relationship. To better understand the surface winds, SST, and ice relation over the marginal ice zone, the correlation distributions with 95% significant level of r-test among the surface winds, SST, and SIC anomalies are shown in Figure 37.
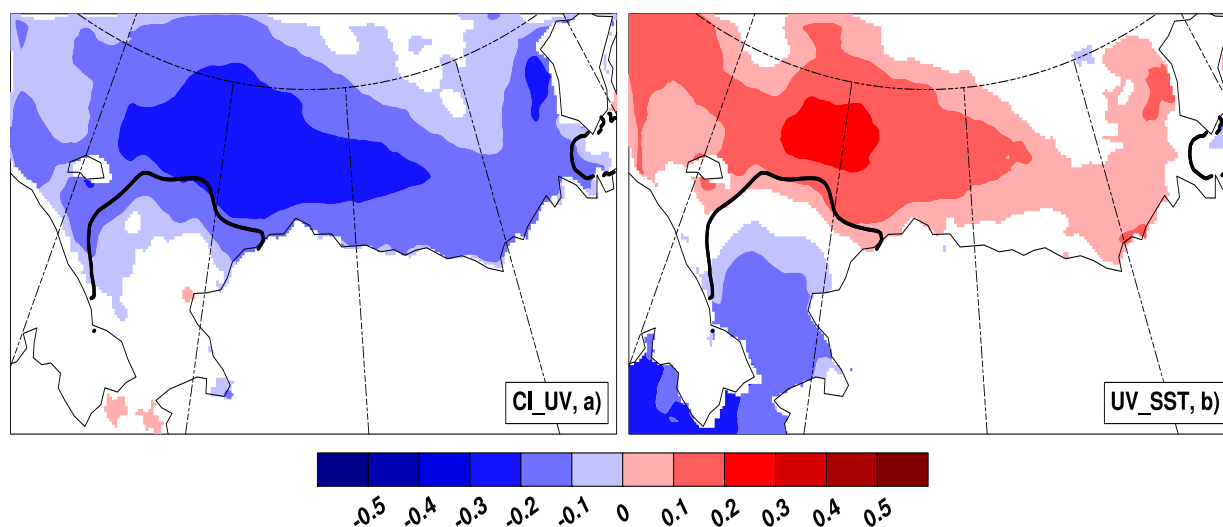


*Figure 37*. Correlation at lag 0 (September and October only) of wind speed and SIC, a), and lag 0 correlation between wind speed and SST, b). The black line is the 20% long-term mean sea ice concentration. The color-filled contours are significant at the 95% level using the r-test.

Confirming the results from Figure 36, there is a clear change in correlation at ~20% SIC indicated by the dark black line in Figure 37 b where there is an inverse relationship in the Chukchi Sea and a linear relationship mainly north of the 20% SIC line.  Figure 37 a shows a clear relationship of sea ice and wind, i.e. less sea ice, higher wind speeds further confirming the results from chapter 3 and Stegall and Zhang, (2012).  The negative correlations between the surface winds and SIC are mainly over the central Chukchi-Beaufort Seas, where there is the strongest SIC gradient (Figure 38).
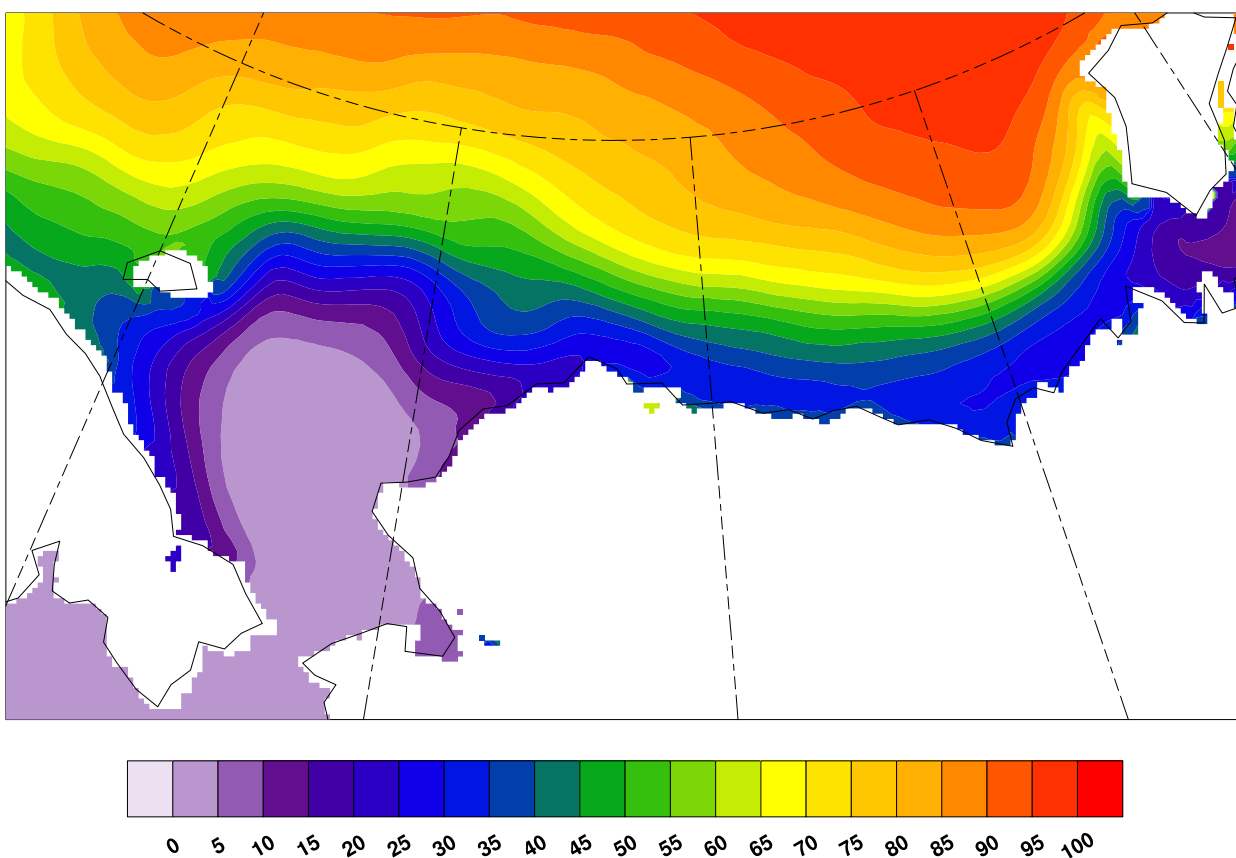


*Figure 38*. Long term mean sea ice concentration (%) in CBHAR during September and October 1979-2009.

The correlations between surface wind and SST show slightly complicated distributions. The negative correlations are mainly over the less ice-covered areas. Over the central Chukchi-Beaufort Seas where negative correlations between winds and SIC are present, a positive correlation between the surface wind and SST anomalies occurs. Which seems to be reasonable due to that warmer SST promotes sea ice melting and then results in enhanced surface winds. Then what's the possible reason for the negative correlations over the less-ice covered areas? A composite analysis is therefore conducted in Section 5.3 for better understanding the mechanisms behind this wind-SST-ice relation.

**5.3 Physical Interpretation for the Wind-SST-Ice Relations**

To further explore the physical interpretation for the wind-SST-ice relation, composite analysis of wind speed anomalies and associated SST and radiation forcing anomalies are constructed with the algorithm introduced in chapter 2.
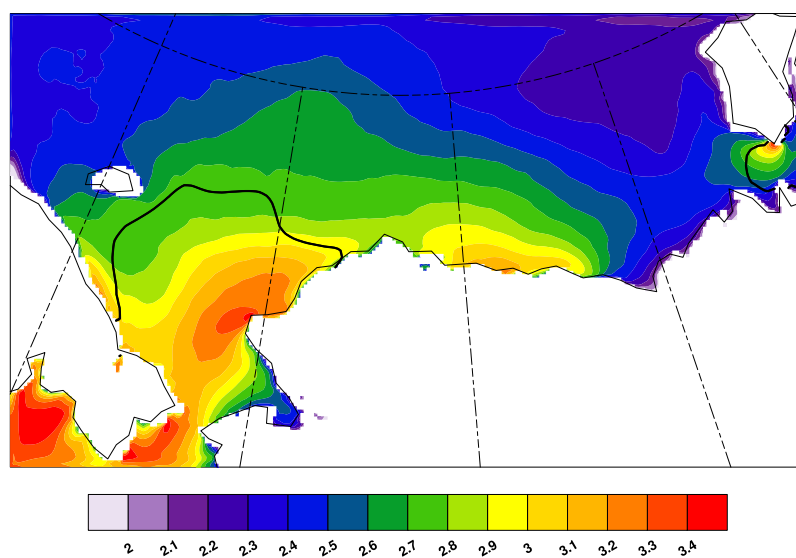


*Figure 39*. The standard deviation of the 31-year daily wind speeds of the CBHAR data from 1979-2009.

The parameter b in the composite equations in Chapter 2, section 2.2 is set to 1.0 (i.e. +/- one

standard deviation of the wind speed) to include relatively stronger anomalies.  From the

distribution of wind speed standard deviation over the study area (Figure 39), the ranges of

standard deviation are 2- 3.5 ms$^{-1}$.  Thus using b=1.0 times the standard deviation should include

strong enough positive wind speed anomalies as well as weak enough negative wind speed

anomalies.

      Figure 40 shows composites of wind speed anomalies and associated SST anomalies, as

well as 2m-air temperature anomalies. The 20% SIC associated with positive and negative

anomalies are overlaid.
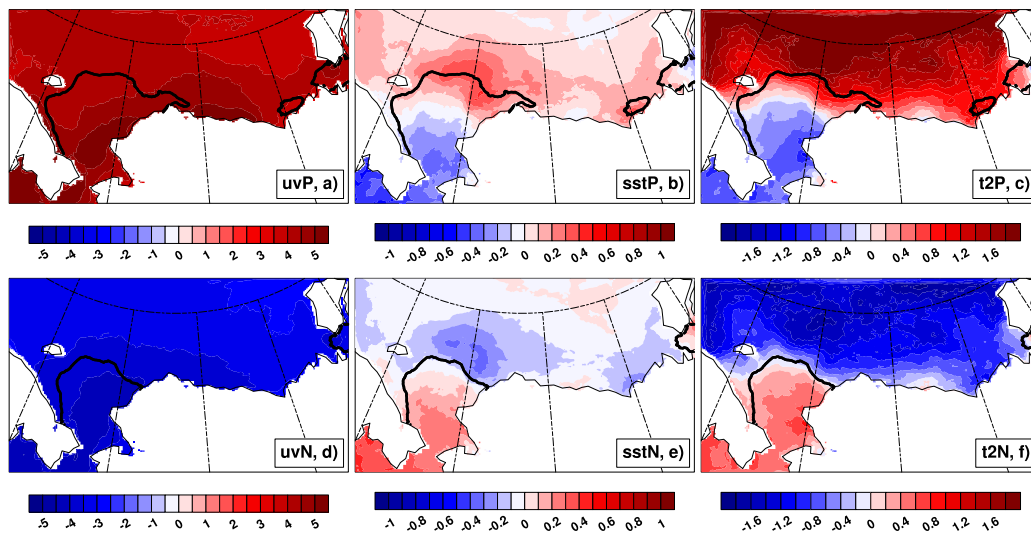


*Figure 40*.  Composites of positive wind speed anomalies (ms$^{-1}$, uvP, a), associated SST

anomalies (K, sstP, b), and associated 2m-air temperature anomalies (K, t2P, c).  d), e), and f) are

the composites of negative wind speed anomalies (ms$^{-1}$, uvN, d),  associated SST anomalies (K,

sstN, e), and associated 2m-air temperature anomalies (K, t2N, f). Black contours are composites

of 20% SIC associated positive and negative wind speed anomalies respectively. The parameter

b in equations in Chapter 2, section 2.2 for anomaly calculation is set to 1.0.

Area with less than 20% sea ice coverage, negative (positive) SST anomalies are associated with positive (negative) wind speed anomalies. These anomalies are mainly located in the Chukchi Sea and Bering Strait.  The greatest negative SST anomalies are along the Siberian coast and in the Bering Sea.  Over areas covered by more than 20% sea ice, opposite anomalies are present, i.e., positive (negative) SST anomalies are associated with positive (negative) wind speed anomalies.
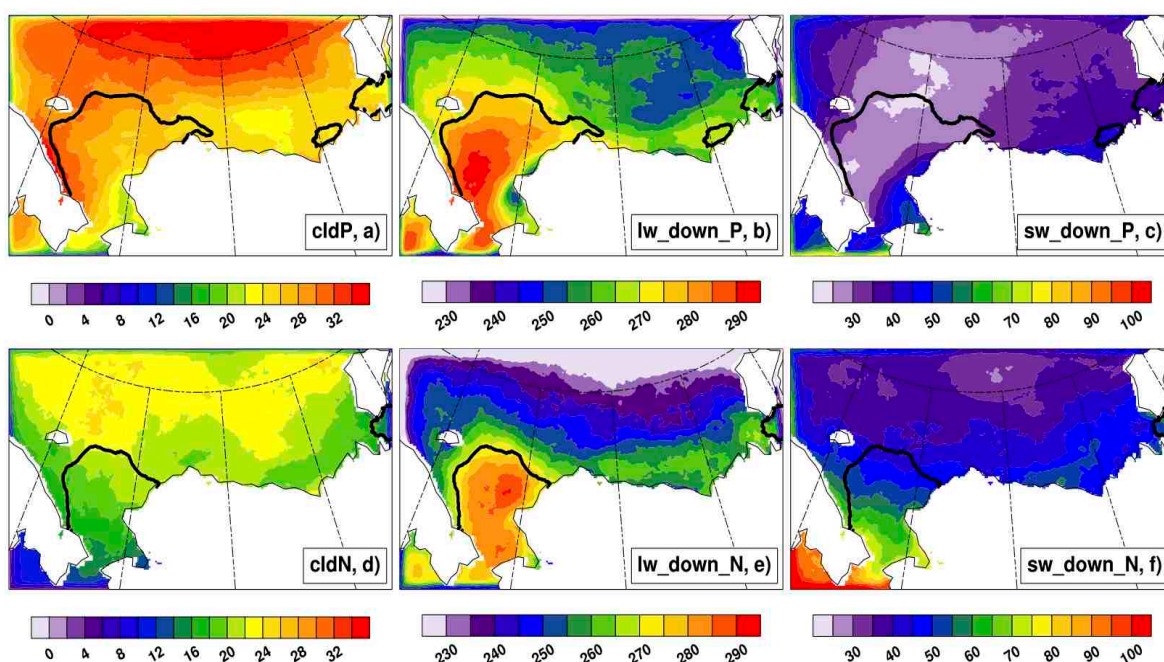


*Figure 41*. Composites of anomalies associated with positive wind anomalies (Figure 40-a) for cloud fraction (%, cldP, a), surface downward longwave radiation (wm$^{-2}$, lw_down_P, b), surface downward shortwave radiation (wm$^{-2}$, sw_down_P, c). d-f are the composites of anomalies associated with negative wind anomalies (Figure 40-d) for cloud fraction ((%, cldN, d), surface downward longwave radiation (wm$^{-2}$, lw_down_N, e), and surface downward shortwave radiation (wm$^{-2}$, sw_down_N, f). Black contour is 20% of long-term average SIC during September and October 1979-2009.

Warm (cold) SST anomalies associated with positive (negative) wind speed anomalies over more ice-covered areas might be the results of atmosphere forcing, rather than the causes for strong (weak) winds. The atmosphere radiation forcing composites associated with positive and negative wind speed anomalies, repetitively, and the differences of these positive and negative composites are presented in Figure 41 and Figure 42.
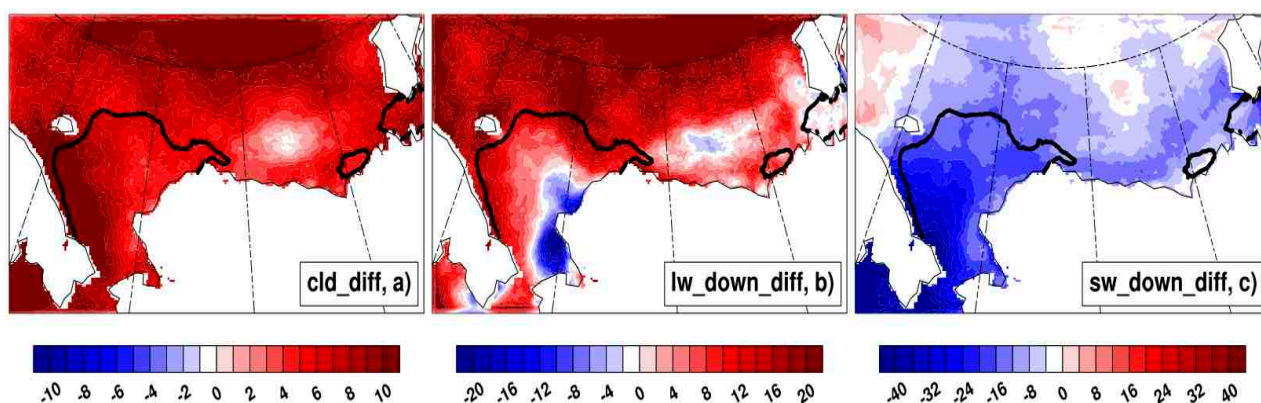


*Figure 42*. Composite differences (composite associated with positive wind speed anomalies minus composite associated with negative wind speed anomalies) for a) cloud fraction (cld_diff, %). b) downward longwave radiation (lw_down_diff, $wm^{-2}$), and c) downward shortwave radiation (sw_down_diff, $wm^{-2}$) respectively. Black contour is the composite of 20% SIC associated with positive wind speed anomalies.

The radiation forcing variables discussed here include cloud fraction, downward longwave and shortwave radiations. It is found that with stronger winds, the atmosphere is much cloudier, which increases the downward longwave radiation and decreases the downward shortwave radiation (Figure 41a-c). Due to that shortwave radiation is already weak during the study period of September-October over the northern part of study area, mainly the north of 20% SIC, as well

as the cold clouds, the clouds are mostly made up of ice crystals, the decrease in shortwave radiation is small (Figure 41c), as a result, more energy absorbed by the surface helps to warm SST and melt ice north of 20% SIC where more sea ice are present (Figure 40b). Obviously the strong winds here are caused by the storm activities. Storms bring both kinetic and thermal energy to the area causing strong winds and strong cloud radiative forcing. When there are less storm activities, weaker winds (Figure 40c) and less cloud and cloud radiation forcing (Figure 41d-e) are present, over the area with weak shortwave radiation (Figure 41f), i.e., mainly north of 20% SIC line, there is reduced energy (Figure 41 e, f) absorbed by the surface, so colder SST occurs (Figure 40d).

With higher winds, increased cloud cover also occurs over the south of 20% SIC, especially along the east Siberian coast, where stronger downward longwave radiation occurs (Figure 42a). Note that the reduced longwave radiation along the west coast of Alaska is likely due to the cold air advection from land (Figure 43). There is a strong decrease in downward shortwave radiation over the south of 20% SIC (Figure 42c), which can be attributed by two folds. One is that the absolute amount of clear-sky downward shortwave radiation is relatively large. The other one is that relatively warmer cloud here can include more water droplets, which efficiently reduces cloudy-sky shortwave radiation comparing to the cold cloud in the north.  As a result, unlike the north of 20% SIC, warmer SST isn't present; instead a colder SST associated with strong winds occurs over the south of 20% SIC (Figure 40b).

To further investigate the colder SST associated with strong winds over south of 20% SIC; thermal advection over the study area is analyzed.  Figure 43 shows the wind vectors overlaid onto the 2m-air temperature associated positive and negative wind speed anomalies.
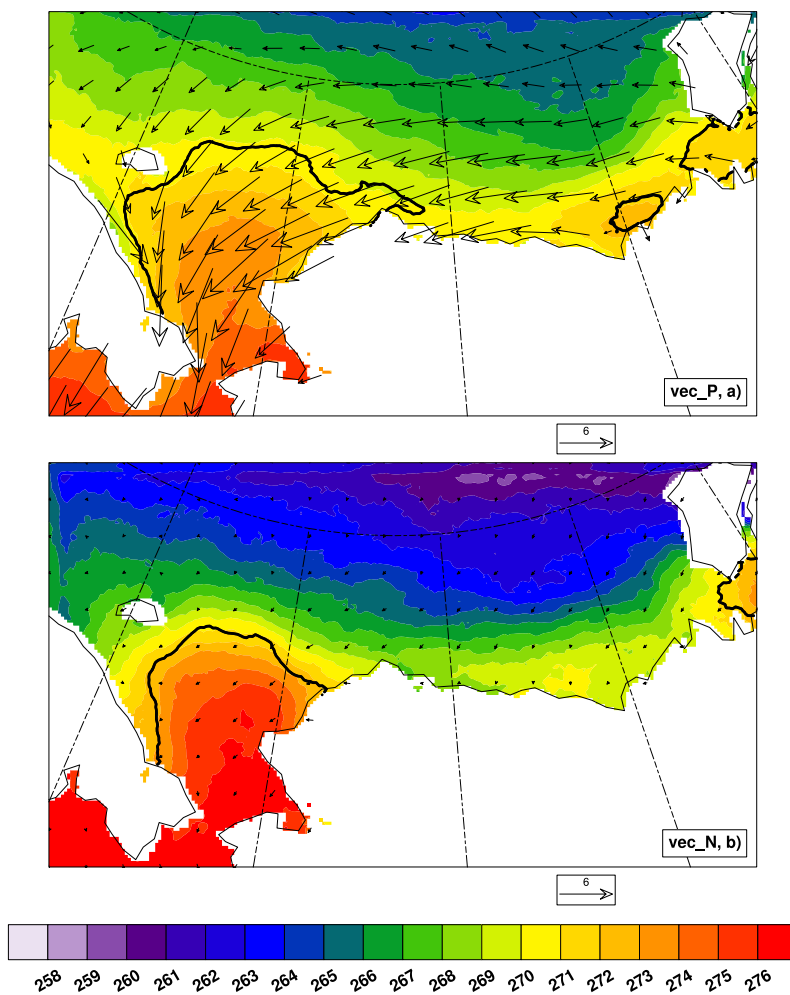
*Figure 43*. Composites of 2m-air temperature in K, and wind vector in ms$^{-1}$ (reference vector 6 ms$^{-1}$) associated with positive wind speed anomalies (a, vec_P), and negative wind speed anomalies (b, vec_N). Black contours are composites of 20% SIC associated with the positive and negative wind speed anomalies respectively.

It is clear strong northward temperature gradient exists in the study area. Meanwhile, with higher winds, east and northeast winds dominant. As a result, strong cold air advection flows from the higher SIC area to the open water and less SIC area in the Chukchi Sea (Figure 44a). Over the north of Chukchi Sea, there is also cold advection due to a warm tongue temperature structure.

Obviously this cold advection isn't strong enough to change the sign of wind-SST correlation.

With weaker winds the advection is nearly zero (Figure 44b).



*Figure 44.* Composite of surface thermal advection (K$^{-s}$ scaled by 10$^{-5}$) associated with positive

wind speed anomalies (a, adv_P) and associated with negative wind speed anomalies (b, vec_N).

Black contours are composite of 20% SIC associated with the positive and negative wind speed

anomalies respectively.

Cold air flowing off the ice over much warmer ocean water produces a strong coupling

between the surface and the air and destabilizes the atmosphere (Vihma and Brümmer, 2002).

With this flow of cold air, clouds can form over ocean water, such as the Chukchi Sea and

Bering Strait, then the accompanied reduced shortwave radiation and precipitation further cool down surface temperature. As a result, colder SST occurs over the ocean water adjacent to the sea ice. Therefore reduced solar radiation plus cold advection contribute to the negative correlation between winds and SST over open water and less ice-covered area. Over north of 20% SIC, enhanced cloud-induced longwave radiation associated with storm activities thus results in positive correlation between winds and SST.

**5.4 Summary and Discussion**

This study has investigated the relationship of wind speed and SST, with the presence of sea ice. There is a clear inverse linear relationship between sea ice and wind speed. Also there is an inverse linear relationship of wind speed and SST (negative correlation) over open ocean up to ~20% SIC. However with increasing SIC up to ~20% to 100% the relationship weakens and is positively correlated with a linear relationship. This weakening is due to more sea ice; the less coupled the atmosphere and ocean become. Cross-correlation analysis of wind speed and SIC as well as cross-correlation of wind speed and SST supports the above conclusions at the 95% significance level.

The composites of wind speed anomalies and associated SST anomalies show a clear inverse relation ship (higher wind speeds, colder SST's), especially in the Chukchi Sea and south of the 20% SIC. North of the 20% SIC there is warmer SST's with higher winds. However warm (cold) SST anomalies associated with positive (negative) wind speed anomalies over more ice-covered areas might be the results of atmosphere forcing, rather than from strong (weak) winds. It is found that with stronger winds, mainly from storm activities bring both kinetic and thermal energy to the area, the atmosphere is much cloudier, which increases the downward longwave radiation and decreases the downward shortwave radiation. Since the shortwave

radiation is already weak during the study period of September-October over the northern part of study area, mainly the north of 20% SIC, as well as the cold clouds are mostly made up of ice crystals, the decrease in shortwave radiation is small resulting in more energy absorbed by the surface to warm SST and melt ice over the north of 20% SIC where more sea ice are present.  In other words, the longwave radiation is larger than the downward shortwave radiation term, thus the SST is warmed mainly by the longwave radiation.  When there are less storm activities, weaker winds and less clouds and less cloud radiation forcing along with weak shortwave radiation, i.e., mainly the north of 20% SIC line, there is reduced energy absorbed by the surface, thus colder SST occurs.

With higher winds, increased cloud cover also occurs over the south of 20% SIC, especially along the east Siberian coast, where stronger longwave radiation occurs.  There is a strong decrease in downward shortwave radiation over the south of 20% SIC, which can be attributed to two reasons. One reason is that the absolute amount of clear-sky downward shortwave radiation is relatively large. The other reason is there are warmer clouds here that can include more water droplets, which efficiently reduces cloudy-sky shortwave radiation comparing to the cold clouds in the north.  The downward shortwave radiation term is larger than the longwave radiation term i.e. there is more energy lost due to shortwave radiation.  As a result a colder SST is associated with a larger downward shortwave radiation term (energy lost) associated with stronger winds south of 20% SIC.

Wind vectors overlaid with 2m-air temperature make it clear that a strong northward temperature gradient exists in the study area. Meanwhile, with higher winds, east and northeast winds are dominant. As a result, strong cold air advection flows from the higher SIC area to the open water and less SIC area in the Chukchi Sea.  Over the north of Chukchi Sea, there is also

cold advection due to a warm tongue temperature structure. Obviously this cold advection isn't strong enough to change the sign of wind-SST correlation. With weaker winds the advection is nearly zero.

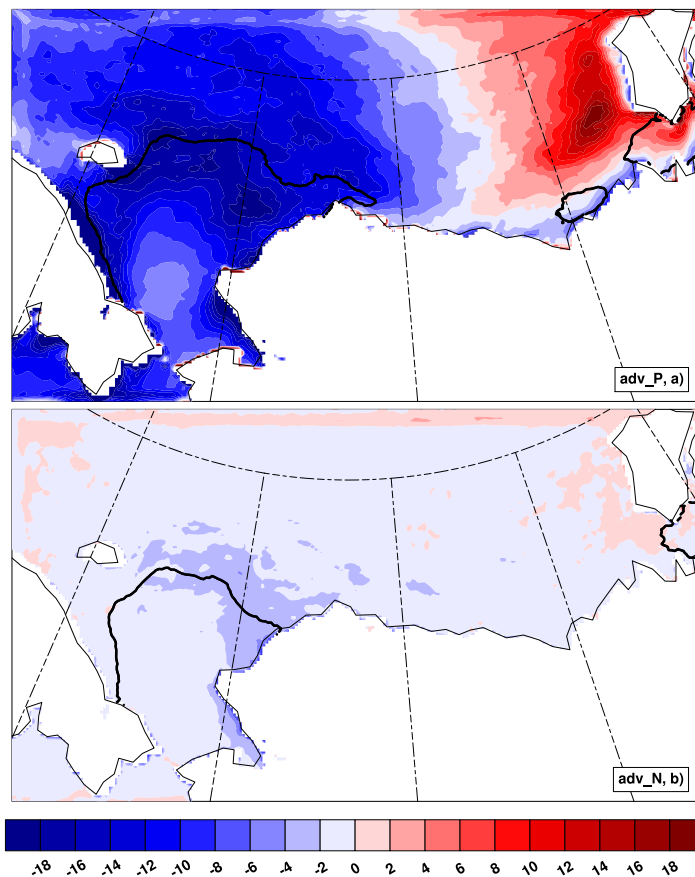With this flow of cold air, clouds can form over ocean water, such as the Chukchi Sea and Bering Strait, then the accompanied reduced shortwave radiation and precipitation further cool surface temperature. As a result, colder SST occurs over the ocean water adjacent to the sea ice. Therefore reduced solar radiation (large downward shortwave radiation term and loss of energy) plus cold advection contributes to the negative correlation between winds and SST over open water and less ice-covered area. North of 20% SIC, enhanced cloud-induced longwave radiation associated with storm activities thus results in positive correlation between winds and SST.

Qian et al., (2012) found similar SST cooling with higher wind speeds in the South China Sea, mainly due to strong sensible heat flux, increase in evaporation/precipitation (increase in cloudiness), weak solar radiation thus cooling the SST's. A similar process is occurring in the Chukchi Sea; increase in sensible heat flux over the open ocean in the Chukchi Sea resulting from high winds and cold air advection, evaporation and an increase in cloudiness and increase in precipitation, and then weak net solar radiation combined with strong cold air advection and cold air damning along the East Siberian Coast, and resulting cooler SST's.

Overall the results above show there is an inverse linear relationship of wind speed and SST's in the Chukchi Sea, with the presence of sea ice. However further study needs to be done with a model coupled with a sea ice model and coupled to an ocean model. Then sensitivity tests of the influence of SIC with atmosphere-ocean-sea ice feedback can be conducted. Also the effects of upwelling/Ekman pumping must also be considered in this region in future research

with a coupled ocean model.  The colder SST's could also be a combination of the atmospheric

effects presented here and colder ocean water upwelled to the ocean surface in the Chukchi Sea.

**CHAPTER 6**

**Summary and Conclusions**

To improve understanding of climate and environment changes in the Chukchi and Beaufort seas, a detailed study of surface wind was conducted. The augmented knowledge is not only of scientific significance but also has important implications for policy-making processes and practical applications, such as assessments and mitigation of oil spill dispersions and coastal erosions should they occur. Using several data sets including NARR, ERA-Interim, and CBHAR, the surface wind field and other associated surface variables such as SST, 2m-air temperature, and sea ice were examined. This included climatology, variability, long-term changes, and extreme events of the surface wind field. Comparison across the datasets was performed to enhance credibility of the scientific findings. In particular, unique mesoscale features are identified and described by taking advantage of the newly developed high-resolution CBHAR data. To better understand the detected changes in surface wind, further analysis was carried out to examine relationships between wind speed, SST, and sea ice.

Climatology and trends of the NARR surface wind field are first analyzed for both the monthly averaged wind speed and 95th percentile wind speeds from 1979-2009. For both the monthly averaged and 95th percentile wind speeds, the minimum occurs in May and June. Concurrent with this minimum is the sea ice covered ocean in the Chukchi-Beaufort Seas. When sea ice reaches its minimum (September-October), the monthly averaged and 95th percentile winds reach their maximum values at 6-9 ms^{-1} and 10-15 ms^{-1}, respectively, mainly occurring over the Chukchi Sea. Over land the wind speeds are much weaker in all seasons. Monthly probability density function (PDF) of the entire domain winds confirms this seasonality with higher wind speeds in the autumn season. NARR shows a diurnal cycle over land from April to September.

The diurnal cycle over sea ice lasts only from mid-March to May.  This is due to the warm season's strong diurnal solar radiation forcing plus relatively small heat capacity over land and sea ice that contribute to the diurnal variations.  Once the sea ice retreats significantly, the large water heat capacity dampens the diurnal fluctuation of winds over the open water.

The 31-year trends of the Monthly average and 95th percentile wind speeds in NARR show an increasing trend in both from July through November. The frequency of extreme wind events (wind speeds above the 95th percentile winds) were analyzed, a similar increasing trend is found, especially in October, with 8% more extreme wind events in 2009 as compared to 1979. Significant retreat in sea ice in the study area, especially during the most recent decade (Comiso et al. 2008; Polyakov et al. 2012) could also contribute to the increasing trend in wind speeds and frequency of extreme wind events.

Northeast (NE) wind most persistently occurs over the study area. However with fluctuation of the Beaufort High and Aleutian Low, the extent of the NE winds changes with the lowest persistence in July through September, and the highest during the colder months (i.e. October to April/May). The frequency of southwest (SW) and northwest (NW) winds is low, except for along the Brooks Range and the Chukotka Mountains in easternmost Russia. The frequency increases to 35% - 50% during the cold season. With the extremely stable airflow plus the mountain barrier effect, this causes the winds to flow along the mountains and thus the mesoscale features are present in the climatology. During the summer months, the land surface is snow free and thus mesoscale mountain/valley breezes develop along the coast and the mountain ranges impacting the wind field on a diurnal basis.

In addition to the climatology of the NARR wind field, The ERA-I and the newly developed dataset CBHAR surface wind fields are compared and the result shows climatology

and trends similar to those in NARR. These two datasets are first tested against observations (coastal and inland station data) and satellite data. The CBHAR data has a smaller RMSE than does ERA-I when compared against the station data and the satellite data. Overall the CBHAR performs better than does the ERA-I, thus the 10km grid spacing is very reliable with less error. Thus the CBHAR data gives a better representation of the wind climate.

Comparing the average wind speeds of CBHAR and ERA-I from 1979-2009 for all months shows that the lowest wind speeds during the summer months and the higher speeds are in the winter months, The highest occur in November for both data sets. During the month of November the wind speeds reach up to 6 ms$^{-1}$ over the Beaufort Sea and 9 ms$^{-1}$ in the Chukchi Sea. The ERA-I shows a very similar seasonality and wind speeds over the oceans. However over land, the CBHAR very clearly captures topographically influenced features that the ERA-I does not. Examples include higher wind speeds over the Brooks Range and interior of Alaska, possibly resulting from drainage and/or mountain/valley breezes. These features are not present in the ERA-I data.

Another feature is the consistently higher coastal wind speeds in the ERA-I than those in the CBHAR, with differences of about 2 ms$^{-1}$. This difference is likely due to a much coarser grid spacing of the ERA-I that that in the CBHAR. Another feature missed by the ERA-I is the anomalous high wind speeds over the Mackenzie River Valley and Delta from October through May that is clearly captured by CBHAR. The 95$^{th}$ percentile winds in the ERA-I are noticeably higher that in the CBHAR, particularly over ocean and sea ice. The differences could be the result of different treatment of sea ice in the in the global model that produced the ERA-I vs. in the CBHAR as well as difference roughness with respect to ocean/ice in each data.

Both CBHAR and ERA-I datasets capture a diurnal cycle over the ocean (sea ice) in

March-May). The CBHAR winds over land give a diurnal cycle similar to NARR from Stegall and Zhang (2012). However the ERA-I maxima and minima are lower, especially in March through May, due to the fact that ERA-I is only 4 times daily vs. 24 times daily in CBHAR. The ocean winds in CBHAR and ERA-I are higher than that found in NARR from Stegall and Zhang (2012). This could be the result of NARR treatment of sea ice in their model.

When wind direction is analyzed using CBHAR and ERA-I datasets, the datasets capture a persistent NE wind direction, especially over the ocean and the Chukchi Sea. Over land both also capture high frequencies of NE winds, however CBHAR very clearly captures mesoscale features and much more details over land than does ERA-I. This difference in ability to capture mesoscale features is very evident when SW and NW winds are analyzed in the winter months. The CBHAR has a much better horizontal resolution (10km, vs. the ERA-I of 0.75° lat/lon), which gives clearer details of the anomalous SW winds over the Brooks Range, and a higher percentage of NW winds over easternmost Siberia. What is also very evident is that the ERA-I essentially fails to capture the anomalous NW winds in the Mackenzie River Delta and Valley, which is clearly captured with the CBHAR data.

The CBHAR and ERA-I datasets show similar trends with the average wind speeds and the 95th percentile wind speeds. The largest and most significant increasing trends for both datasets are in October. When the CBHAR data is divided into ocean and land areas separately, the trends show varying trends from month to month. However, the trends in August and October over the ocean and September and November over land are significant at the 95% level using the t-test. The most pronounced increasing trend is in October. Areal linear trends show a sizable area of the Chukchi/Beaufort Seas to be decreasing in January as well as a sizable area of the Beaufort Seas in May and June. However, the linear trends show a substantial portion of the

Chukchi/Beaufort Seas to be increasing in October. This is similar finding in Stegall and Zhang (2012) where they showed a significant and high negative correlation between retreating sea ice and stronger wind speeds.

In addition to wind speed and direction analysis, trends in sea ice, 2m-air temperature, and SST was also analyzed using the CBHAR data. It is important to confirm these trends, i.e. decreasing sea ice with increasing SST and 2m-air temperature. Given that sea ice loss is occurring dramatically in the region, Jahn et al. (2012) used both modeled and observed sea ice to support its conclusions.  It is important that the CBHAR show similar trends, even though the sea ice in CBHAR was prescribed by observational data and not from the WRF model. The trends are analyzed from July through October, when sea ice fluctuates the largest. Results show that there is significant sea ice loss, especially in September and October, with increasing trends in SST and 2m-air temperature. Areal linear trends show similar results of the sea ice, SST and 2m-air trends, especially in September through November show the largest sea ice loss and the largest 2m-air temperature and SST increases over the Chukchi/Beaufort Seas, with the largest trends in the Beaufort Sea.

The sea ice minimum occurs in September and October in the study area. This is also a time of year with high wind speeds and interaction of wind, open ocean, and sea ice. Most studies, mainly in the tropics and mid-latitudes, show a positive linear relationship between wind speed and SST. Unique to the Chukchi/Beaufort Seas is the presence of sea ice, thus the wind speed/SST relationship is explored with the presence of sea ice.

There is a clear inverse linear relationship between sea ice and wind speed (negative correlation). Also there is an inverse linear relationship of wind speed and SST (negative correlation) over open ocean with SIC less than 20%. However, when SIC increases to 20%-

100%, the relationship weakens and surface wind speed and SST show a linear relationship (positively correlated). This correlation change can be attributable to sea-ice-modulated coupling processes between the atmosphere and ocean. Cross-correlation analysis of wind speed and SIC show that above the ~20% SIC, sea ice and wind speed are negatively correlated. Cross-correlation of wind speed and SST supports the above conclusions, with negative correlation below ~20% SIC and positive correlation above ~20% SIC. Both lag correlations are at the 95% significance level.

The composites of wind speed anomalies and associated SST anomalies show a clear inverse relationship (higher wind speeds, colder SST's), especially in the Chukchi Sea where there is less sea ice covered areas. In contrast, with higher sea ice covered areas, higher winds correspond to warmer SSTs. The association between SST anomalies and wind speed anomalies is a consequence of particular weather system forcing. It is found that strong winds mainly result from storm activities, which bring both kinetic and thermal energy to the area. The stormy weather is generally accompanied with cloudy sky, which increases the downward longwave radiation and decreases the downward shortwave radiation. Shortwave radiation is generally weaker over the northern part of study area mainly mostly ice covered areas. Further, clouds over this northern area are dominantly made up of ice crystals. The shortwave radiation and advection is small when compared to longwave radiation resulting in more energy absorbed by the surface to warm SST and melt ice where more sea ice are present. In other words, the longwave radiation is larger than the downward shortwave radiation term, thus the SST is warmed mainly by the longwave radiation. During the time with weakened storm activities, weaker winds occur, and, at the same time, reduced cloud cover and resulting decreased cloud-forcing longwave radiation lead to colder SSTs.

During the stormy weather, both higher winds and cloud cover can occur at the same time over the area with less sea ice cover and open ocean, especially along the east Siberian coast. Storm-induced higher cloud cover causes an increase in downward longwave radiation. However, the increased downward longwave radiation cannot compensate the decreased downward shortwave radiation, because, downward clear-sky shortwave radiation is relatively large in this southern area (downward shortwave radiation term is larger than the longwave radiation term, i.e. more energy is lost due to decreased shortwave radiation than longwave radiation). Meanwhile, warmer clouds in this area include more water droplets, which efficiently reduces cloudy-sky shortwave radiation comparing to the cold clouds in the north. As a result, colder SST's associated with larger downward shortwave radiation occurs south with less sea ice covered areas and open ocean along with stronger winds.

The 2m-air temperature distribution shows a strong northward temperature gradient exists in the study area. Meanwhile, strong wind speeds are dominated by east and northeast winds. As a result, there is strong cold air advection from the higher SIC area to the open water and less SIC area in the Chukchi Sea. Over the north of Chukchi Sea, there is also cold advection due to a warm tongue temperature structure. Obviously this cold advection isn't strong enough to change the sign of wind-SST correlation. With weaker winds the advection is nearly zero.

With this flow of cold air, clouds can form over ocean water, such as the Chukchi Sea and Bering Strait, then the accompanied reduction in shortwave radiation and precipitation further cool surface temperature. As a result, colder SST occurs over the ocean water adjacent to the sea ice. Therefore reduced solar radiation (large downward shortwave radiation term and loss of energy) plus cold advection contributes to the negative correlation between winds and SST over open water and less ice-covered area. North over mostly ice covered areas, enhanced cloud-

induced longwave radiation associated with storm activities thus results in positive correlation between winds and SST.

Qian et al., (2012) found similar SST cooling with higher wind speeds in the South China Sea, mainly due to strong sensible heat flux, increase in evaporation/precipitation (increase in cloudiness), weak solar radiation thus cooling the SST's. A similar process is occurring in the Chukchi Sea; increase in sensible heat flux over the open ocean in the Chukchi Sea resulting from high winds and cold air advection, evaporation and an increase in cloudiness and increase in precipitation, and then weak net solar radiation combined with strong cold air advection and cold air damning along the East Siberian Coast, and resulting cooler SST's. Overall the results above show there is an inverse linear relationship of wind speed and SST's in the Chukchi Sea, with the presence of sea ice. However further study needs to be done with a model coupled with a sea ice model and coupled to an ocean model. Then sensitivity tests of the influence of SIC with atmosphere-ocean-sea ice feedback can be conducted. Also the effects of upwelling/Ekman pumping must also be considered in this region in future research with a coupled ocean model. The colder SST's could also be a combination of the atmospheric effects presented here and colder ocean water upwelled to the ocean surface in the Chukchi Sea.  Future research of this inverse wind speed/SST relationship should also include expanding to a larger region i.e. the entire Arctic region, or global scale and identifying areas with this feature and comparing and contrasting physical interpretations to those studied in Chukchi/Beaufort Seas region.

References

ACIA, Arctic Climate Impact Assessment (2005), Cambridge University Press, 1042 pp.

Bell, G.D., and L. F. Bosart (1988), Appalachian Cold-Air Damming, *Mon. Wea. Rev.*, **116**, 137-161.

Bonekamp, H., G. J. Komen, A. Sterl, P. A. E. Janssen, P. K. Taylor, and M J. Yelland (2002), Statistical Comparisons of Observed and ECMWF Modeled Open Ocean Surface Drag, *J. Phys. Oceanogr.*, **32**, 1010-1027.

Bromwich, D. H., K. M. Hines, and L.-S. Bai (2009), Development and testing of Polar WRF: 2. Arctic Ocean, *J. Geophys. Res.*, **114**, D08122, doi:10.1029/2008JD010300.

Bromwich, D., Y.-H. Kuo, M. Serreze, J. Walsh, L.S. Bai, M. Barlage, K. Hines, and A, Slater (2010), Arctic System Reanalysis: Call for community involvement, *EOS Trans. AGU*, **91**, 13-14.

Businger, S., and J. Baik (1991), An Arctic Hurricane over the Bering Sea, *Mon. Wea. Rev.*, **119**, 2293-2322.

Cassano, J. J., M. E. Higgins, and M. W. Seefeldt (2011), Performance of the Weather Research and Forecasting (WRF) Model for Month-long pan-Arctic Simulations, *Mon. Wea. Rev.,* in press, doi: 10.1175/MWR-D-10-05065.1.

Chelton, D. B., and S.-P. Xie (2010), Coupled Ocean-Atmosphere Interaction at Oceanic Mesoscales, *Oceanogr. Mag.*, **4**, 52-69.

Chen, F. and J. Dudhia (2001), Coupling an advanced land-surface hydrology model with the PSU/NCAR MM5 modeling system. Part I: Model description and implementation, *Mon. Wea. Rev.*, **129**, 569–585.

Comiso, J. C. (2006), Abrupt decline in the Arctic winter sea ice cover, *Geophys. Res. Lett.*, **33**, L18504, doi:10.1029/2006GL027341.

Comiso, J. C., C. L. Parkinson, R. Gersten, and L. Stock (2008), Accelerated decline in the Arctic sea ice cover, *Geophys. Res. Lett.*, **35**, L01703, doi:10.1029/2007GL031972.

Comiso, J. C. (2012), Large decadal decline of the Arctic multiyear ice cover. J. Climate, 25, 1176–1193.

Crosby, D. S., L. C. Breaker, W. H. Gemmill (1993), A proposed definition for vector correlation in geophysics: theory and application, *J. Atmos. Oceanic Technol.*, **10**, 355–367.

Dee, D. P., and Co-Authors (2011), The ERA-Interim Reanalysis: Configuration and Performance of the Data Assimilation System, *Q. J. R. Meteorol., Soc.*, **137**, 553-597.

Fairall, C. W., E. F. Bradley, J.E. Hare, A. A. Grachev, and J. B. Edson (2012) Bulk Parameterization of Air-Sea Fluxes: Updates and Verification for the COARE Algorithm, *J. Climate*, **16**, 571-591.

Farrugia, P. S., and A. Micallef (2006), Comparative analysis of estimators for wind direction standard deviation, *J. Appl. Met,* **13**, 29-41, doi:10.1017/S1350482705001982.

Fedorov, Alexey V., W. Kendall Melville (2009), A Model of Strongly Forced Wind Waves. *J. Phys. Oceanogr.*, **39**, 2502–2522.

Grell, G. A. and D. Devenyi (2002), A generalized approach to parameterizing convection combining ensemble and data assimilation techniques, *Geophys. Res. Lett.*, **29**, 1693, doi: 10.1029/2002GL015311.

Harden, B.E., I. A. Renfrew, and G. N. Petersen (2011), A Climatology of Wintertime Barrier Winds off Southeast Greenland, *J. Clim.,* **24**, 4701-4717.

Hines, K. M. and D. H. Bromwich (2008), Development and testing of Polar Weather Research and Forecasting (WRF) Model. Part I: Greenland ice sheet meteorology, *Mon. Wea. Rev.*, **136**, 1971–1989.

Hines, K. M., D. H. Bromwich, L.-S. Bai, M. Barlage, and A. G. Slater (2011), Development and testing of Polar WRF. Part III: Arctic land, *J. Climate*, **24**, 26–48.

Iacono, M. J., J. S. Delamere, E. J. Mlawer, M. W. Shephard, S. A. Clough, and W. D. Collins (2008), Radiative forcing by long-lived greenhouse gases: Calculations with the AER radiative transfer models, *J. Geophys. Res.*, **113**, D13103, doi: 10.1029/2008JD009944.

Jahn, A., and Coauthors (2012), Late-Twentieth-Century Simulation of Arctic Sea Ice and Ocean Properties in the CCSM4, *J. Climate*, **25**, 1431-1452.

Janjic, Z. I. (2002), Nonsingular implementation of the Mellor–Yamada level 2.5 scheme in the NCEP Meso model, NCEP Office Note, No. 437, 61 pp.

Jiménez, Pedro A., Jimy Dudhia (2012), Improving the Representation of Resolved and Unresolved Topographic Effects on Surface Wind in the WRF Model. *J. Appl. Meteor. Climatol.*, **51**, 300–316.

Johannessen, O. M., and Coauthors (2004), Arctic climate change: Observed and modeled temperature and sea ice variability, *Tellus A*, **56**, 328-341.

Kara, A. B., P. A. Rochford, and H. E. Hurlburt (2000), Efficient and Accurate Bulk Parameterizations of Air-Sea Fluxes for Use in General Circulation Models, *J. Atmos. Oceanic. Technol.*, **17**, 1421-1438.

Kara, A. B., H. E. Hurlburt, A. J. Wallcraft (2005), Stability-Dependent Exchange Coefficients for Air-Sea Fluxes, *J. Atmos. Oceanic. Technol.*, **22**, 1080-1094.

Kozo, T. (1979), Evidence for sea breezes on the Alaskan Beaufort Sea coast, *Geophys. Res. Lett.*, **6**, 849–852.

Kozo, T. (1980), Mountain Barrier Baroclinity effects on surface winds along the Alaskan coast, *Geophys. Res. Lett.*, **7**, 377–380.

Large, W. G., and S. Pond (1981), Open Ocean Momentum Flux Measurements in Moderate to Strong Winds, *J. Phys. Oceanogr.*, **11**, 324-336.

Lindsay, R. W., and J. Zhang (2005), The Thinning of Arctic Sea Ice, 1988-2003: Have We Passes a Tipping Point?, *J. Climate*, **18**, 4879-.4894.

Ludwig, Francis L., Douglas K. Miller, Shawn G. Gallaher (2006), Evaluating a Hybrid Prognostic–Diagnostic Model That Improves Wind Forecast Resolution in Complex Coastal Topography. *J. Appl. Meteor. Climatol.*, **45**, 155–177.

Lynch, A. H., E. N. Cassano, J. J. Cassano, and L. R. Lestak (2003), Case Studies of High Wind Events in Barrow, Alaska: Climatological Context and Development Processes, *Mon. Weath. Rev.*, **131**, 719-732.

Lynch, A. H., J. A. Curry, R. D. Brunner, and J. A. Maslanik (2004), Toward an integrated assessment of the impacts of extreme winds events on Barrow, Alaska, *Bull. Amer. Meteor. Soc.*, **85**, 209-221.

Mahajan, S., R. Zhang, and T. L. Delworth (2011), Impact of the Atlantic Meridional Overturning Circulation (AMOC) on Arctic Surface Air Temperature and Sea Ice Variability, *J. Climate*, **24**, 6573-6581.

Mellor, G. L. and T. Yamada (1982), Development of a turbulence closure model for geophysical fluid problems, *Rev. Geophys. Space Phys.*, **20**, 851–875.

Mesinger, F., and Co-Authors (2006), North American Regional Reanalysis, *Bull. Amer. Meteor. Soc.*, **87**, 343-360.

Monin, A. S., and A. M. Obukhov (1954), Basic laws of turbulent mixing in the surface layer of the atmosphere, *Akad. Nauk. SSSR Geofiz. Inst. Tr.,* **24**, 163-187.

Morrison, H. C., G. Thompson, and V. Tatarskii (2009), Impact of cloud microphysics on the development of trailing stratiform precipitation in a simulated squall line: Comparison of one- and two-moment schemes, *Mon. Wea. Rev.*, **137**, 991–1007.

O'Connor, W. P., D. H. Bromwich, and J. F. Carrasco (1994), Cyclonically Forced Barrier Winds along the Transantarctic Mountains near Ross Island, *Mon. Wea. Rev.*, **138**, 137-150.

O'Neill, L. W., D. B. Chelton, and S. K. Esbensen (2010), The Effects of SST-Induced Surface Wind Speed and Direction Gradients on Midlatitude Surface Vorticity and Divergence, *J. Climate,* **23**, 255-281.

O'Neill, L. W. (2012), Wind Speed and Stability Effects on Coupling between Surface Wind Stress and SST Observed from Buoys and Satellite, *j. Climate*, **25**, 1544-1569.

Overland, J. E. (2009), Meteorology of the Beaufort Sea, *J. Geophys. Res.*, **114**, doi: 10.1029/2008JC004861.

Overland, J. E., and R. L. Colony (1994), Geostrophic drag coefficients for the central Arctic derived from Soviet drifting station data, *Tellus*, **46A**, 75-85.

Overland, J. E., M. Wang, and S. Salo (2008), The recent Arctic Warm Period, *Tellus*, **60A**, 589-597.

Parish, T.R. (1983), The Influence of the Antarctic Peninsula on the Wind Field Over the Western Weddell Sea, *J. Geophys. Res.*, **88**, 2684-2692.

Pattantyus, Andre K., Sen Chiao, Stanley Czyzyk (2011), Improving High-Resolution Model Forecasts of Downslope Winds in the Las Vegas Valley. *J. Appl. Meteor. Climatol.*, **50**, 1324–1340.

Pickart, R. S., G. W. K. Moore, D. J. Torres, P. S. Fratantoni, R. A. Goldsmith, and J. Yang (2009), Upwelling on the continental slope of the Alaskan Beaufort Sea: Storms, ice, and oceanographic response, *J. Geophys. Res.*, **114**, doi:10.1029/2008JC005009.

Polyakov, I. V., R. Kwok, and J. E. Walsh (2012), Recent changes of arctic multiyear sea-ice coverage 1 and the likely causes, *Bull. Amer. Meteor.,* doi: 10.1175/BAMS-D-11-00070.1.

Qian, H., Y. Suxiang, and Z. Yaocun (2012), Analysis of Local Air-Sea Interaction in East Asia Using a Regional Air-Sea Coupled Model, *J. Climate*, **25**, 767-776.

Reed, M. et al. (1999), Oil spill modeling towards the close of the 20th century: Overview of the state of the art, *Spill Sci. Technol. Bull.*, **5**, 3–16.

Sampe. T., and S.-P. Xie (2007), Mapping High Sea Winds from Space, *Bull. Amer. Meteor. Soc.*, **88**, 1965-1978.

Schweiger, A, J., R. W. Lindsay, S. Vavrus, and J. A. Francis (2008), Relationships between Arctic Sea Ice and Clouds during Autumn, *J. Climate,* **21**, 4799-4810.

Serreze, M. C. (2011), Characteristics of the Beaufort Sea High, *J. Climate*, **24**, 159-182.

Shimada, K.., T. Kamoshida, M. Itoh, S. Nishino, E. Carmack, F. McLaughlin, S. Zimmermann, and A. Proshutinky (2006), Pacific Ocean Inflow: Influence on Catastophic Reduction of Sea Ice Cover in the Arctic Ocean, *Geophys. Res. Lett.,* **33**, L08605, doi: 10.1029/2005GL025624.

Shulski, M. D., and J. You (2011), Meteorlogical Data for the Beaufort and Chukchi Sea Coastal Region of the Arctic: Observing Stations and Quality Control Procedures. BOEMRE project report.

Skamarock, W. C., J. B. Klemp, J. Dudhia, D. O. Gill, D. M. Barker, M. G. Duda, X.-Y. Huang, W. Wang, and J. G. Powers (2008), A description of the Advanced Research WRF Version 3, NCAR Tech Note, NCAR/TN–475+STR, 113 pp.

Small, D., E. Atallah, and J. Gyakum (2011), Wind Regimes along the Beaufort Sea Coast Favorable for Strong Wind Events at Tuktoyaktuk, *J. App. Met. Clim.*, **50**, 1291-1306.

Spall, M. A., R. S. Pickart, P. S. Fratantoni, and A. J. Plueddemann (2008), Western Arctic Shelfbreak Eddies: Formation and Transport, *J. Phys. Oceanogr.*, **38**, 1644-1688.

Stegall S. T., J. Zhang (2012), Wind Field Climatology, Changes, and Extremes in the Chukchi-Beaufort Seas and Alaska North Slope during 1979-2009, *J. Climate*, **25**, 8075-8089.

Stroeve, J. C., V. Kattsov, A. Barrett, M. Serreze, T. Pavlova, M. Holland, and W. N. Meier (2012), Trends in Arctic sea ice extent from CMIP5, CMIP3 and observations, *Geophys. Res. Lett.*, **39**, L16502, doi:10.1029/2012GL052676.

Stroeve, J.C., M. Serreze, M. Holland, J. Kay, J. Malanik, and A. Barrett (2012), The Arctic's Rapidly Shrinking Sea Ice Cover: A Research Synthesis. *Clim. Ch*. **110**(3): 1005-1027.

Swail, V. R., V. J. Cardone, B. Callahan, M. Ferguson, D. J. Gummer, and A. T. Cox (2007), The MSC Beaufort Wind and Wave Reanalysis, 1-22.

Taylor, K. E. (2001), Summarizing multiple aspects of model performance in a single diagram, *J. Geophys. Res.*, **106**, 7183–7192, doi:10.1029/2000JD900719.

Thompson, W. J., and J. M. Wallace (1998), The Arctic Oscillation signature in the wintertime qeopotential height and temperature fields, *Geophys. Res. Lett.*, **25**, 1297-3000.

Trenberth, K. E., W. G. Large, and J. G. Olson (1989), The Effective Drag Coefficient for Evaluating Wind Stress over the Oceans, *J. Climate*, **2**, 1507-1516.

Wang, X., and J. R. Key (2005), Arctic Surface, Cloud, and Radiation Properties Based on the AVHRR Polar Pathfinder Dataset. Part I: Spacial and Temporal Characteristics, *J. Climate*, **18**, 2558-2574.

Wang, M., and J. E. Overland (2012), A sea ice free summer Arctic within 30 years: An update from CMIP5 models, *Geophys. Res. Lett.*, **39**, L18501, doi:10.1029/2012GL052868.

Zeng X., M. Zhoa, and R. E. Dickinson (1998), Intercomparison of Bulk Aerodynamic Algorithms for the Computation of Sea Surface Fluxes Using TOGA COARE and TAO Data, *J. Climate*, **11**, 2628-2644.

Zhang, X., and J. E. Walsh (2006), Toward a Seasonally Ice-Covered Arctic Ocean: Scenarios from the IPCC AR4 Models Simulations, *J. Climate*, **19**, 1730-1747.

Zhang, J., and X. Zhang (2010), A soil moisture assimilation scheme using satellite-retrieved skin temperature in meso-scale weather forecast model, *Atm. Res.,* **95**, 333-352, doi:10.1016/j.atmosres.2009.09.003.

Zhang, X., J. E. Walsh, J. Zhang, U. Bhatt, and M. Ikeda (2004), Climatology and interannual variability of Arctic cyclone activity: 1948–2002, *J. Clim.*, **17**, 2300–2317.

Zhang, X., A. Sorteberg, J. Zhang, R. Gerdes, and J. C. Comiso, (2008), Recent radical shifts of

atmospheric circulations and rapid changes in Arctic climate system. *Geophys. Res.

Lett.*, **35**, doi: 10.1029/2008GL035607.

Zhang, X., J. Zhang, J. Krieger, M. Shulski, F. Liu, S. Stegall, W. Tao, J. You, W. Baule, and B.

Potter (2013), Beaufort and Chukchi Seas Mesoscale Meteorology Modeling Study, Final

Report. U.S. Dept. of the Interior, Bureau of Ocean Energy Management, Alaska OCS

Region, Anchorage, AK. OCS Study BOEM 2013-0119. 204 pp.

*Appendix A*
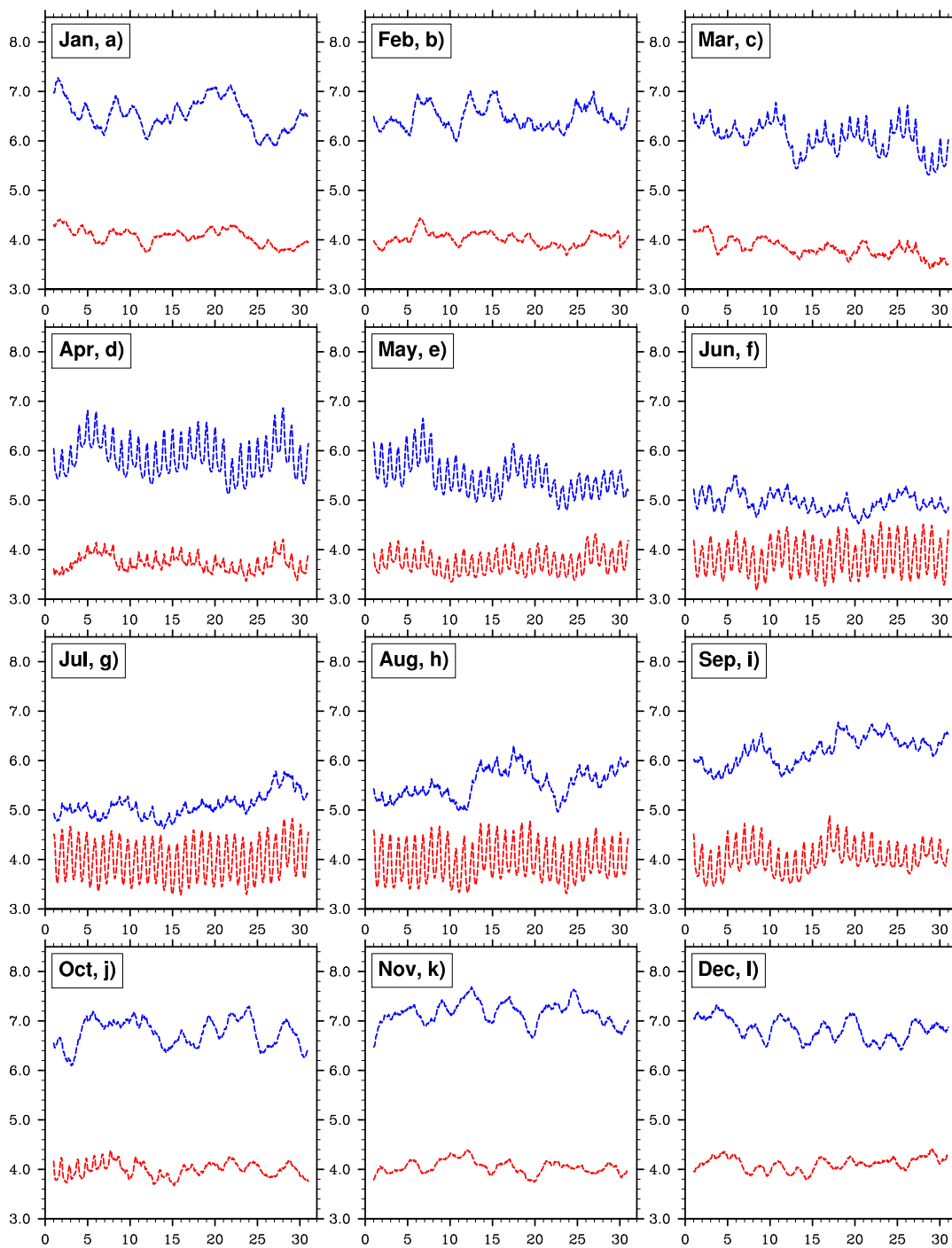


*Figure 45*. The hourly wind speeds averaged over the study region for the 31-years using

CBHAR, with ocean (blue) and land (red).
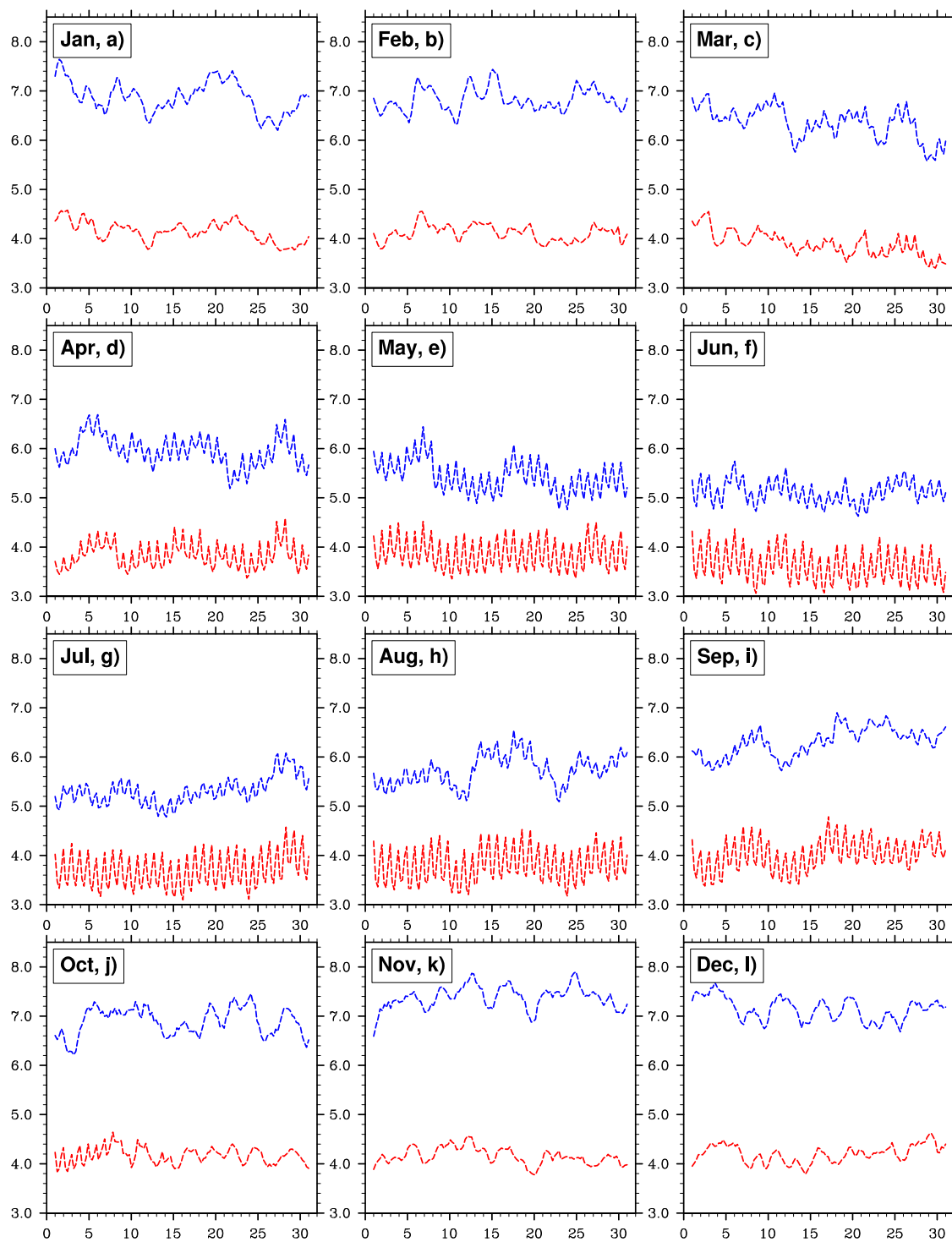
*Figure 46.* The six hourly wind speeds averaged over the study region for the 31-years using ERA-Interim, with ocean (blue) and land (red).
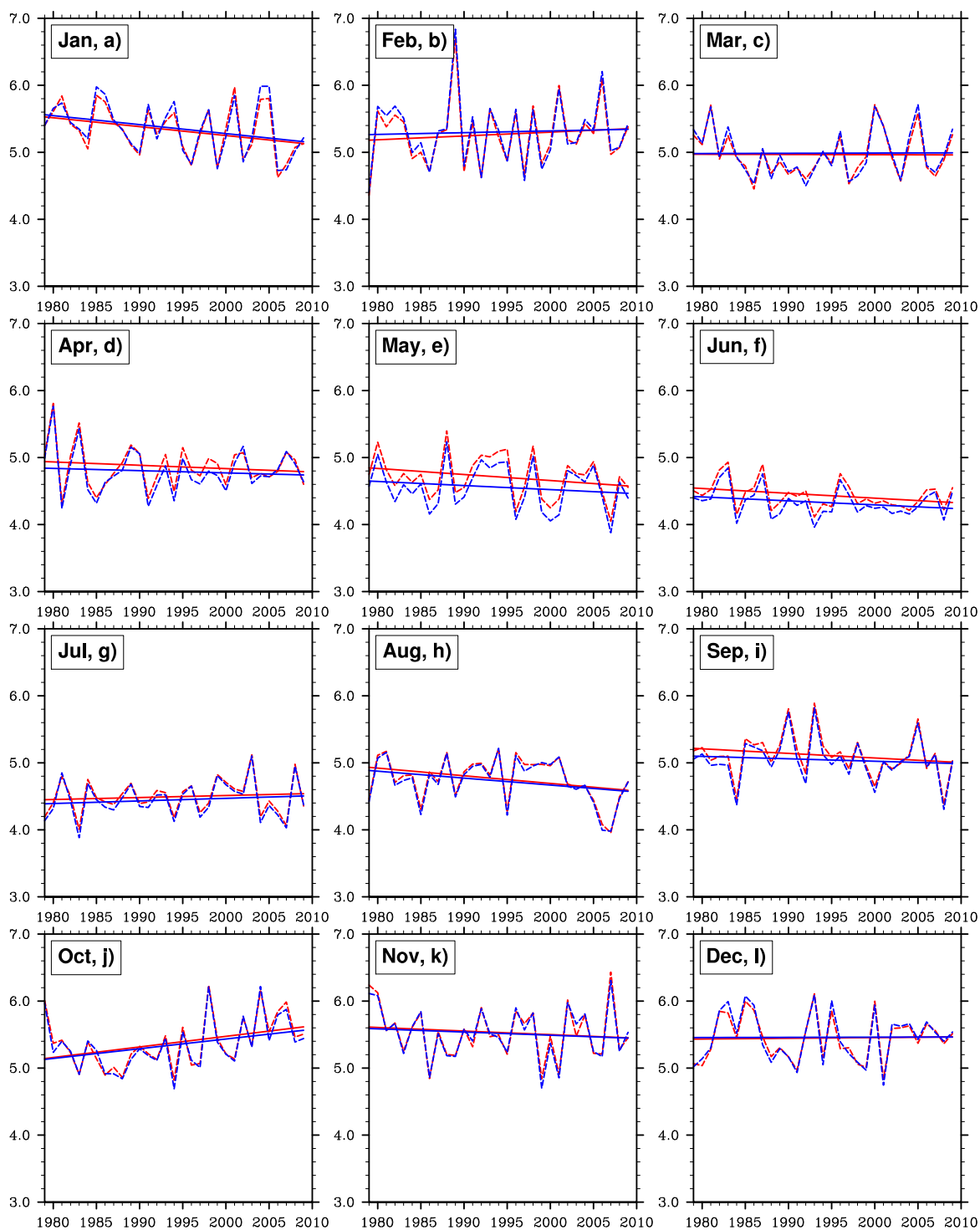
*Figure 47.* Monthly mean surface wind speeds (m s⁻¹) and their linear trends in CBHAR (red) and ERA-Interim (blue) from 1979-2009.
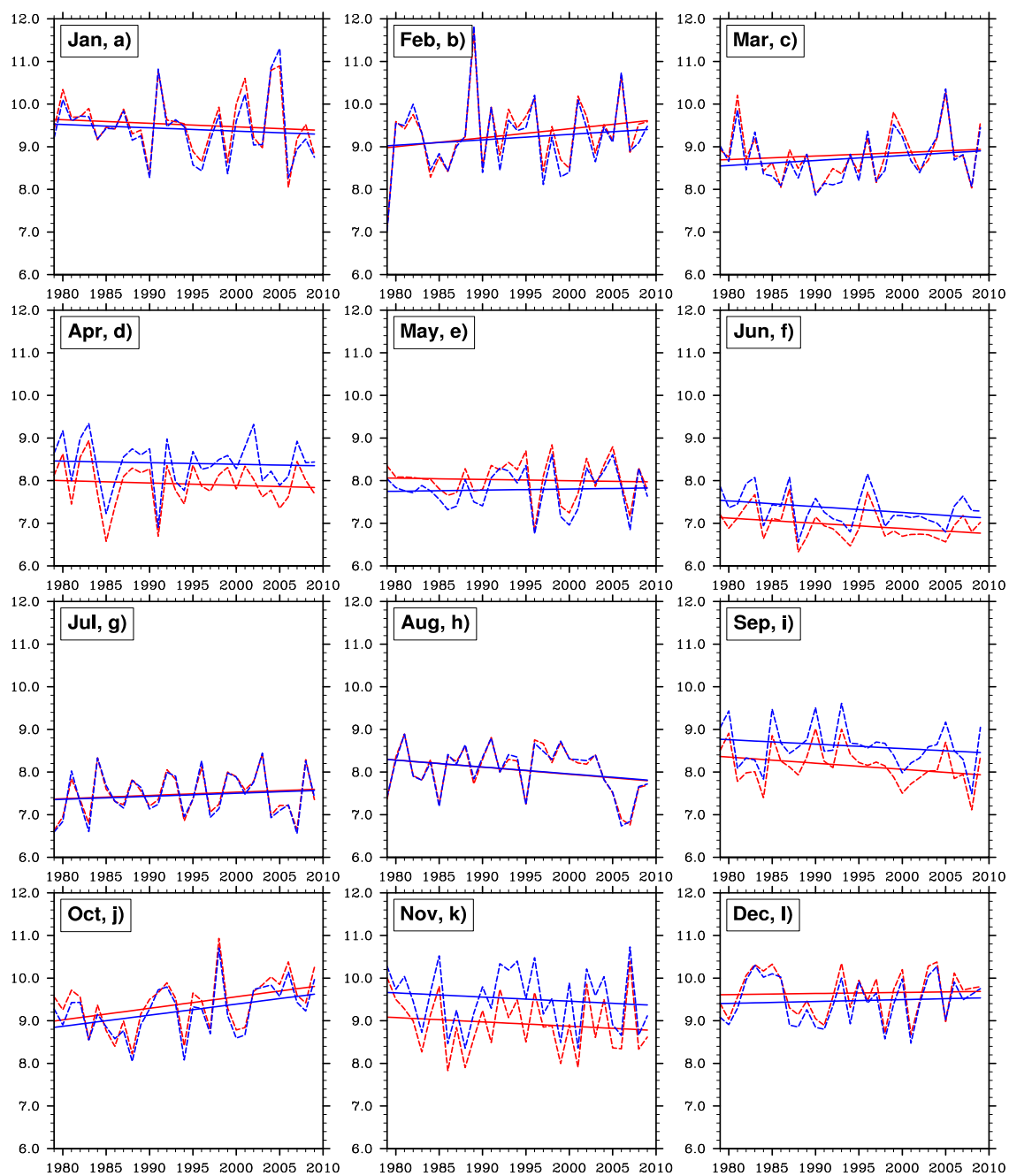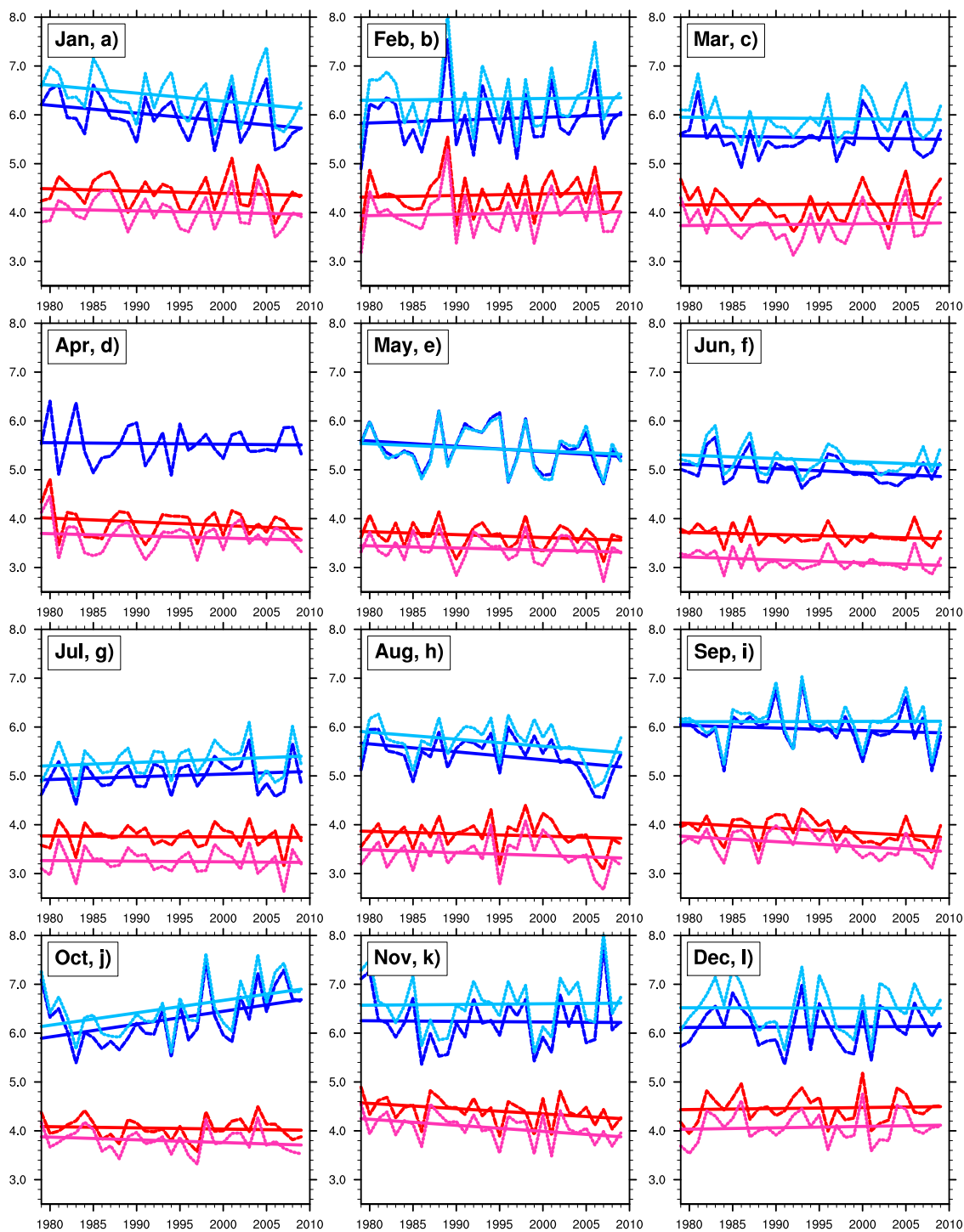
*Figure 48.* Monthly mean 95th percentile wind speeds (m s-1) and their linear trends in CBHAR (red) and ERA-Interim (blue) from 1979-2009.

*Figure 49.* Monthly mean surface wind speeds (m s⁻¹) and their linear trend over ocean

(CBHAR is in blue, ERA-I is in light blue) and land (CBHAR is in red, ERA-I is in light red) for
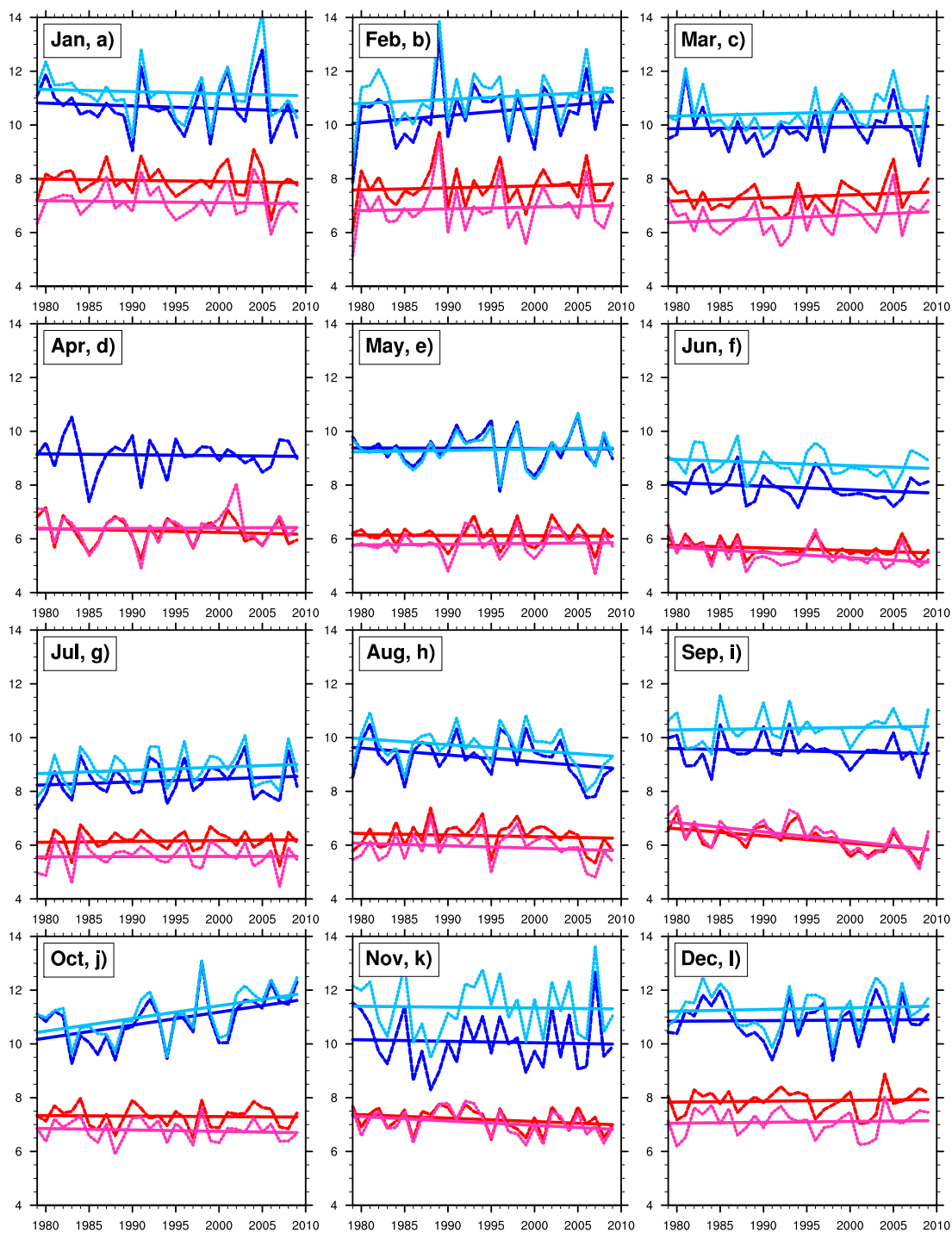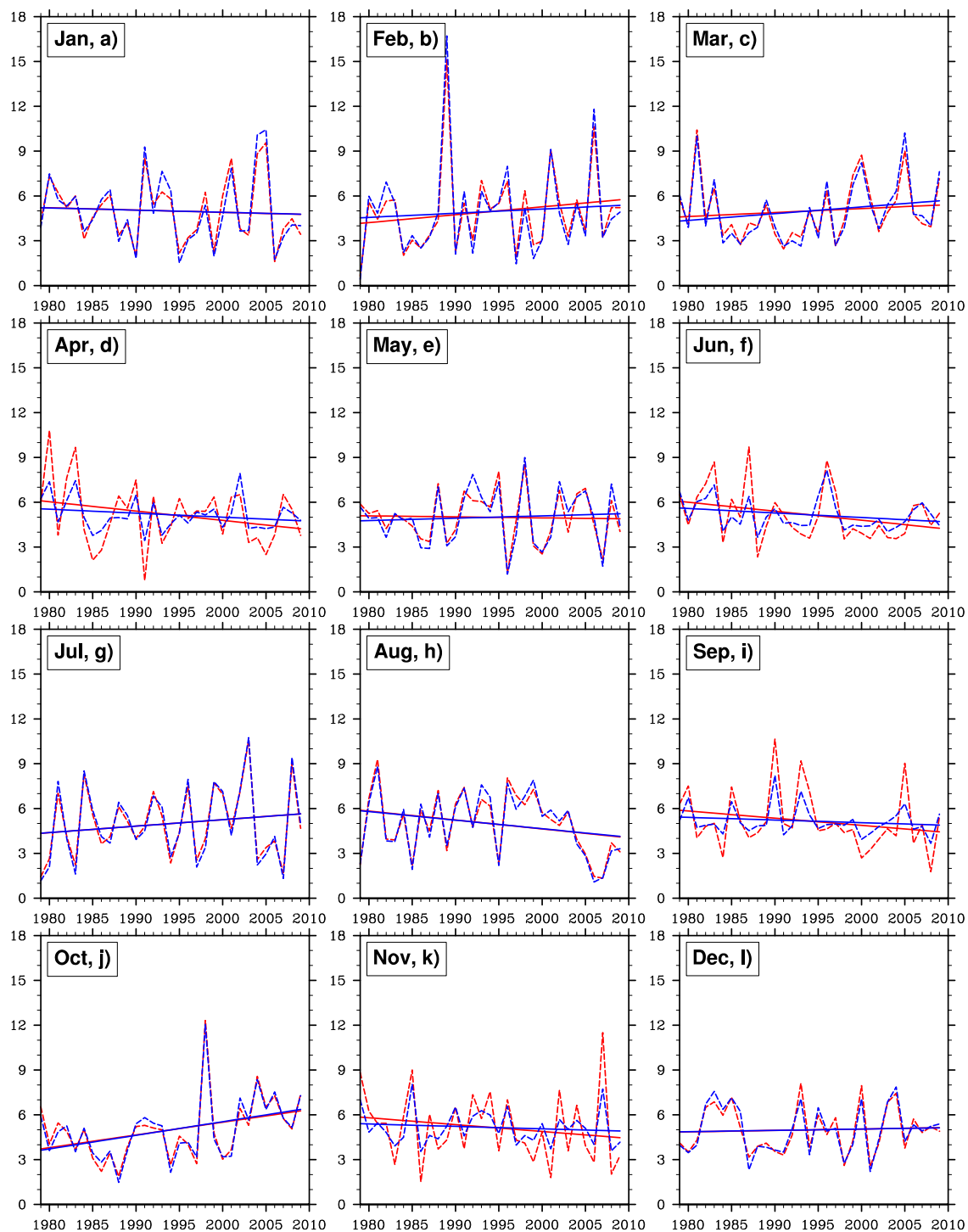
1979-2009.

*Figure 50.* Monthly mean 95th percentile surface wind speeds (m s$^{-1}$) and their linear trend over ocean (CBHAR is in blue, ERA-I is in light blue) and land (CBHAR is in red, ERA-I is in light red) for 1979-2009.

*Figure 51.* Frequency of extreme winds, defined as the percent (%) winds above the 95th percentile wind speed, from 1979-2009 in CBHAR (red), and ERA-interim (blue).
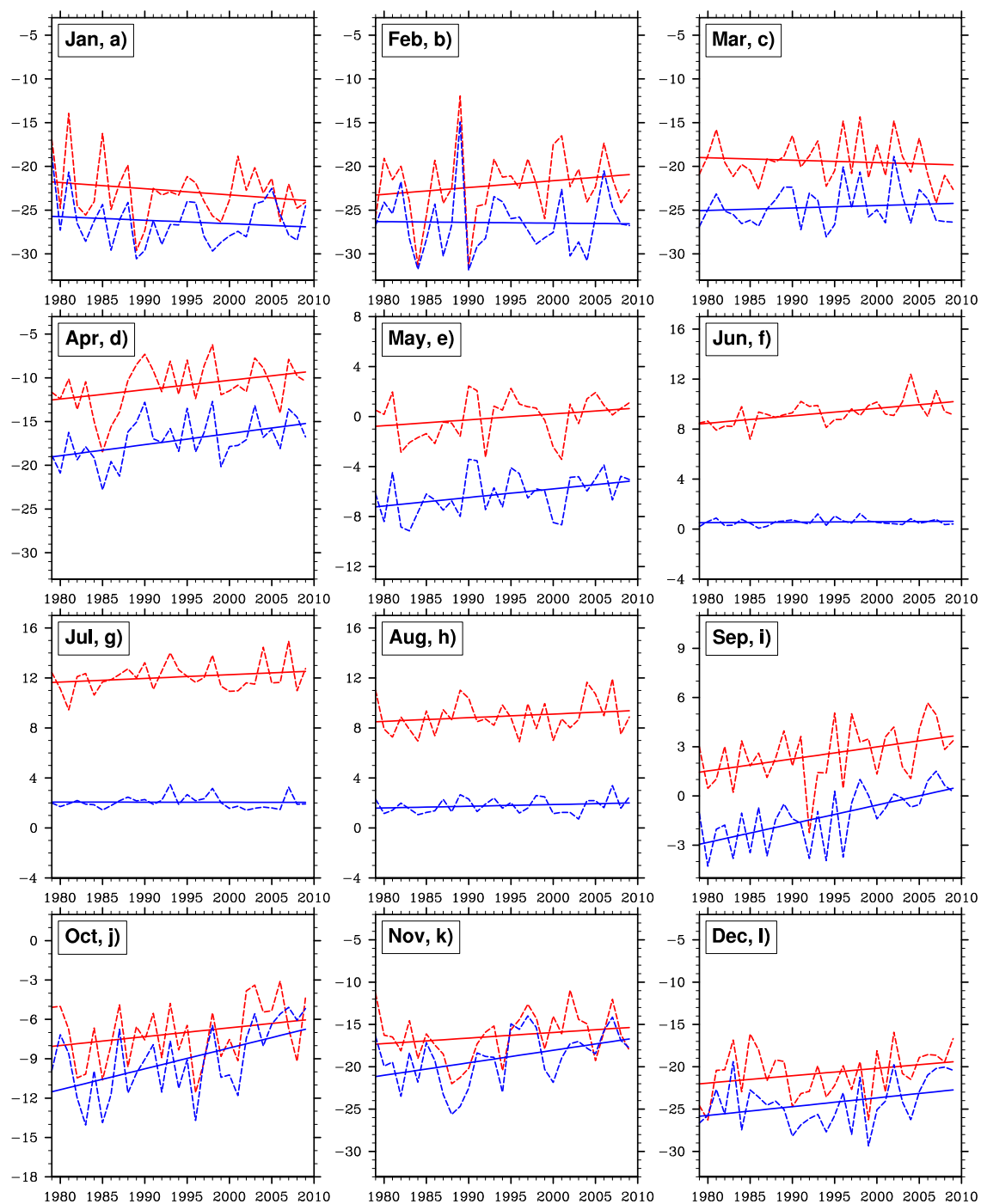
*Figure 52.* Monthly 2m-air temperatures and their trends for 1979-2009 over ocean (blue) and land (red).

*Appendix B*

**Analysis of Chukchi Sea vs. Beaufort Sea with CBHAR**

To further explore the geographic variability of the region, the ocean surface wind data was split into two distinct regions, the Chukchi Sea and the Beaufort Sea, separated by the 203°E meridian that passes through Point Barrow, Alaska (Figure 53).
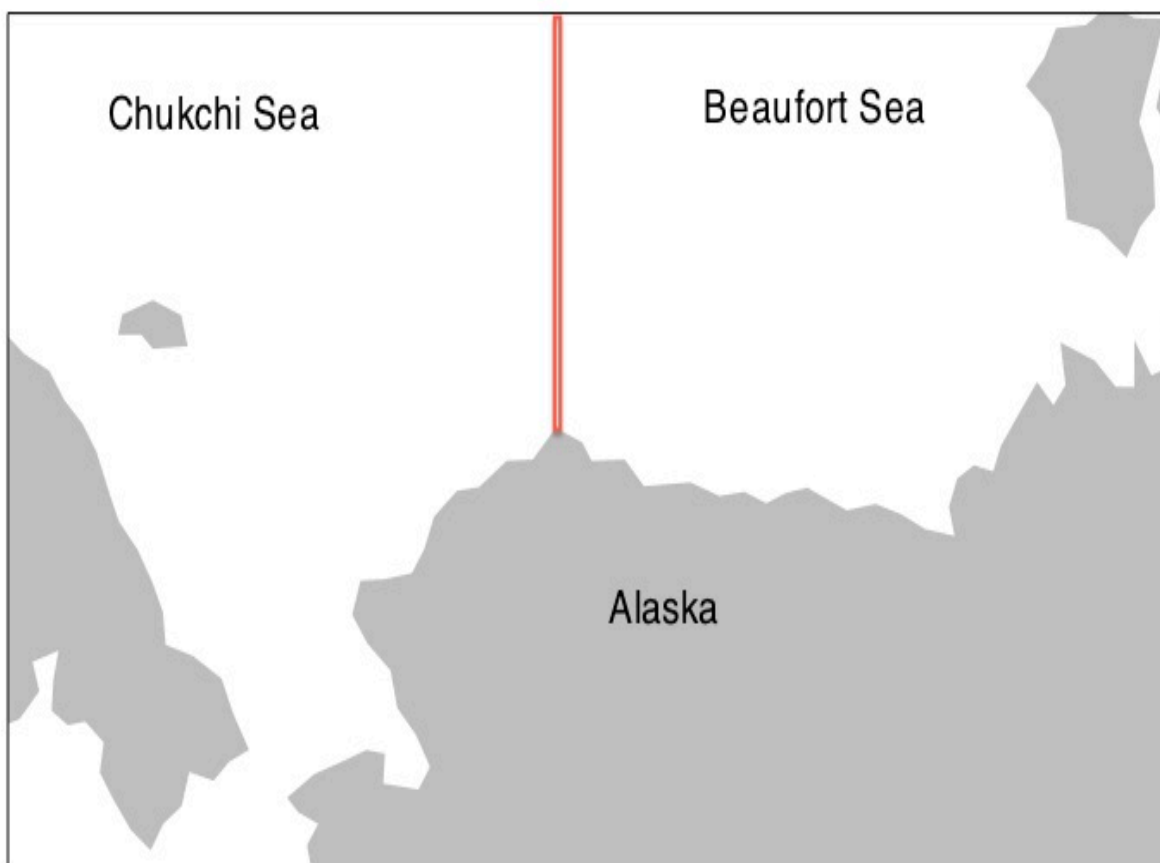


*Figure 53*. Illistration of Chukchi Sea region vs. the Beaufort region. The two regions are separated by the 203° E longitude extending north from Point Barrow Alaska.

In this way the trends specific to each region can be explored separately. Figure 54 and Figure 55 show the trends of wind speed and 95th-percentile wind speed, respectively, for each of the two zones. It is immediately apparent that the Chukchi Sea wind speeds are, on average, higher than the Beaufort Sea wind speeds for each month. Reasons for this difference could be the presence of greater storm activity over the Chukchi and/or stronger storms that first pass over the Chukchi Sea before weakening as they move over the Beaufort. Consistent with the trend analysis discussed above, October shows the largest increase in wind speeds, with the two regions displaying similar increasing trends for this month. As with the mean wind speeds, the Chukchi Sea 95th percentile wind speeds are consistently higher than those over the Beaufort, and October again shows the largest increasing trend. However, in this case, the Beaufort Sea winds are increasing at a faster rate than the Chukchi winds for October. The faster winds in the Chukchi Sea should be the result of more open ocean than in the Beaufort Sea. The big difference in wind speeds in November reflects this difference in sea ice cover. By now the Beaufort Sea has much more sea ice than the Chukchi Sea. Another difference between the two regions is that the Chukchi winds are increasing more in February than those over the Beaufort for both mean and 95th-percentile wind speeds. This increase in the Chukchi Sea wind speeds is also present in March and could be a result of either increased storm frequency or intensity, and may be a worthwhile topic for future exploration. Implications here is that with more open ocean, especially in the Chukchi Sea, will have higher wind speeds. Thus for oil spill assessment high winds, especially if there is open water will be a major factor.
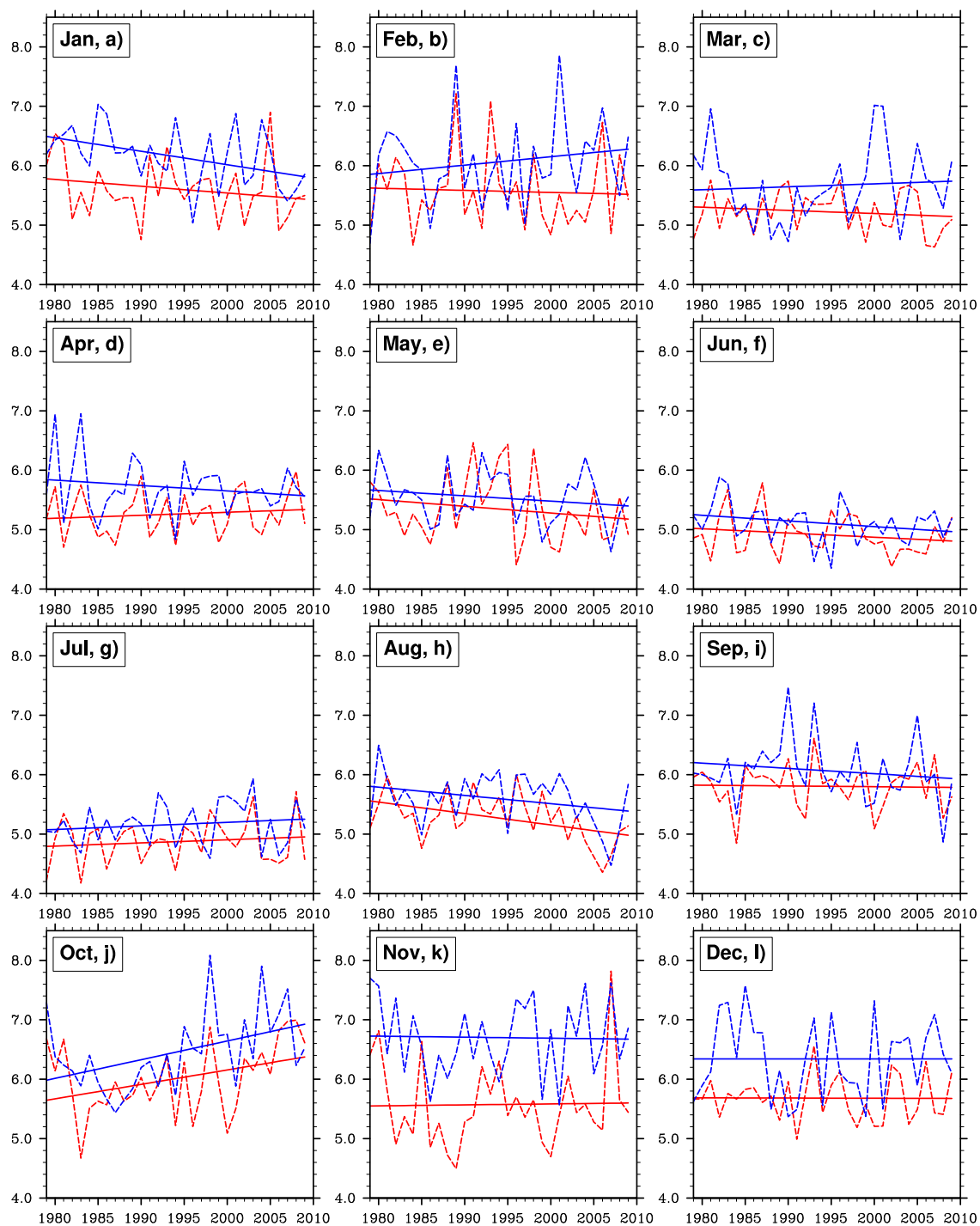
*Figure 54.* Monthly surface wind speeds and their linear trends for the Chukchi Sea (blue) and Beaufort Sea (red). All data is for ocean points only.
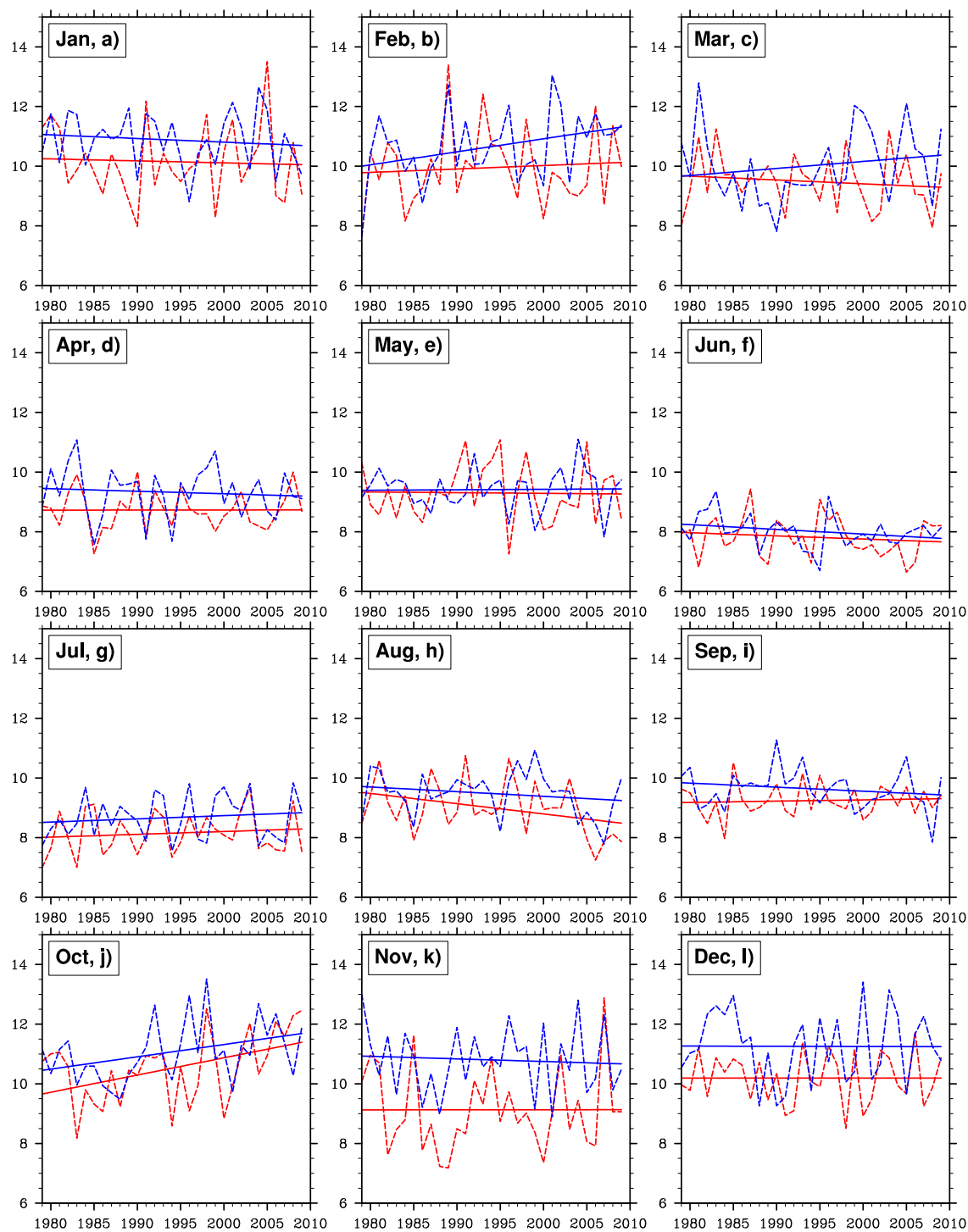
*Figure 55.* Monthly 95<sup>th</sup> Percentile wind speeds and their linear trends over the Chukchi Sea

(blue) and Beaufort Sea (red). All data is for ocean points only.

As with the wind speed analysis, the trends in sea ice extent are divided into Chukchi Sea and Beaufort Sea regions to investigate if differences exist in the trends between the two seas. Figure 56 shows these trends for July through October. Clearly, the Chukchi Sea has a larger decreasing trend than does the Beaufort for each of the four months, particularly in September and October. In September of 2007 and 2008 CBHAR shows nearly 0 km$^2$ in ice extent in the Chukchi, indicative of the record sea ice loss for those years. Lindsay and Zhang (2005) reported that this region is experiencing some of the greatest sea ice thinning of anywhere in the world, along with rising 2m-air temperatures in the autumn. This supports the dramatic sea ice loss shown in the figures here.
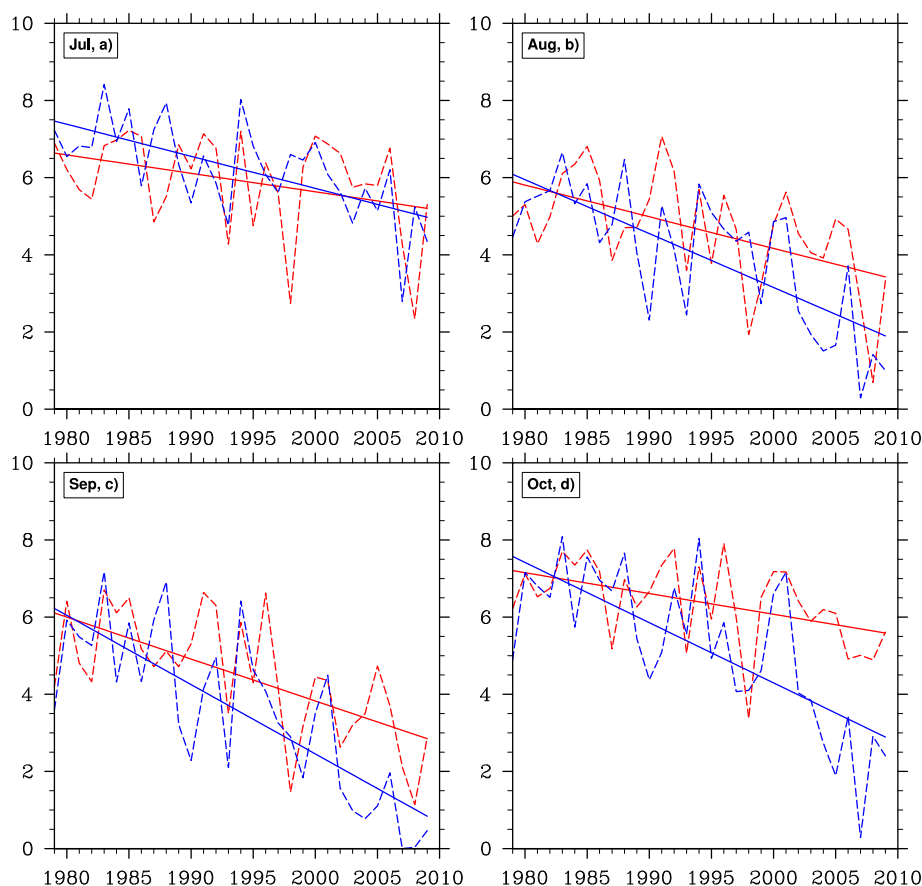


*Figure 56.* Monthly sea ice extents (SIE, X 10$^5$ km$^2$) and their linear trends for the Chukchi Sea (blue) and the Beaufort Sea (red).

Figure 57 shows the area averaged 2m-air temperature trends over the Chukchi and Beaufort Sea regions separately. The summer months (May-August) show little trend for the two regions. For September to December, the Chukchi Sea (blue) shows a larger increase in temperature than the Beaufort Sea (red). The three plots above indicate much warmer air later in the 31-year study period. This warmer air is one potential cause for the substantial sea ice loss in the region. The larger increase in temperature in the Chukchi Sea should and does indicate a larger decrease in sea ice extent in the region relative to the Beaufort Sea.
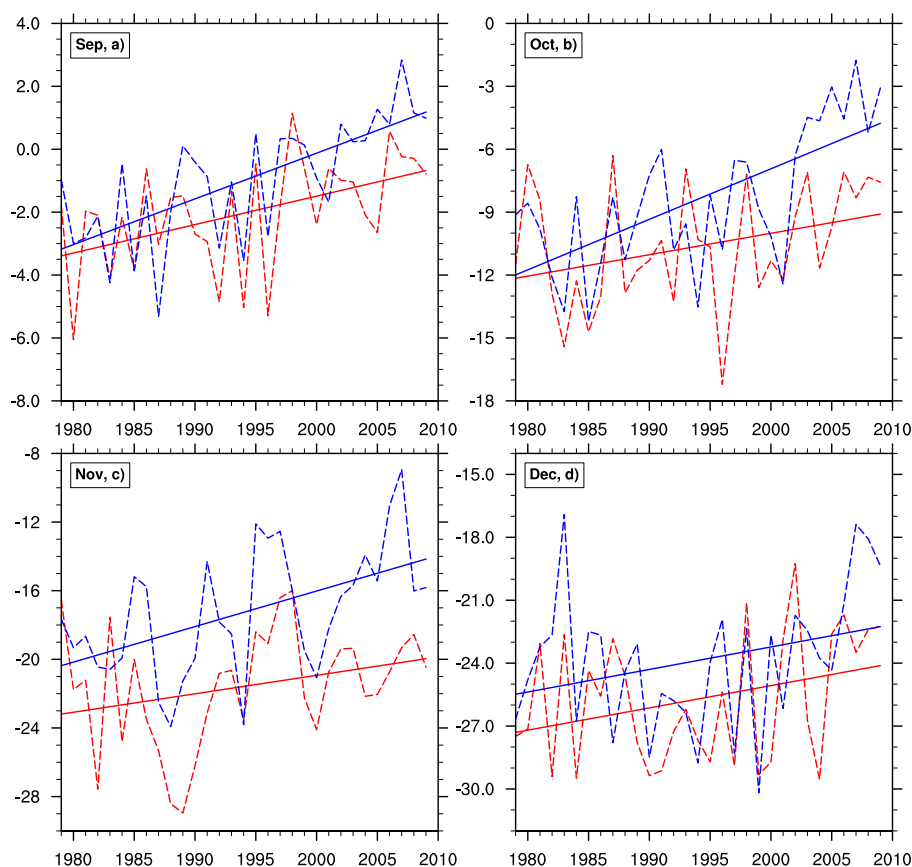


*Figure 57.* Monthly mean 2m-air temperatures and their trends over the Chukchi Sea (blue) and the Beaufort Sea (red) from 1979-2009.

Figure 58 is the trend of SST when the region is divided to the Chukchi Sea and Beaufort Sea, similar to above for the wind speeds and temperatures analyses. When the regions are separated, clearly the Chukchi Sea (blue) has a much larger increasing trend for all four months, with the largest in September. The Beaufort Sea only shows an increasing trend in September; with no real tend in the other months, except a slight decrease in July.
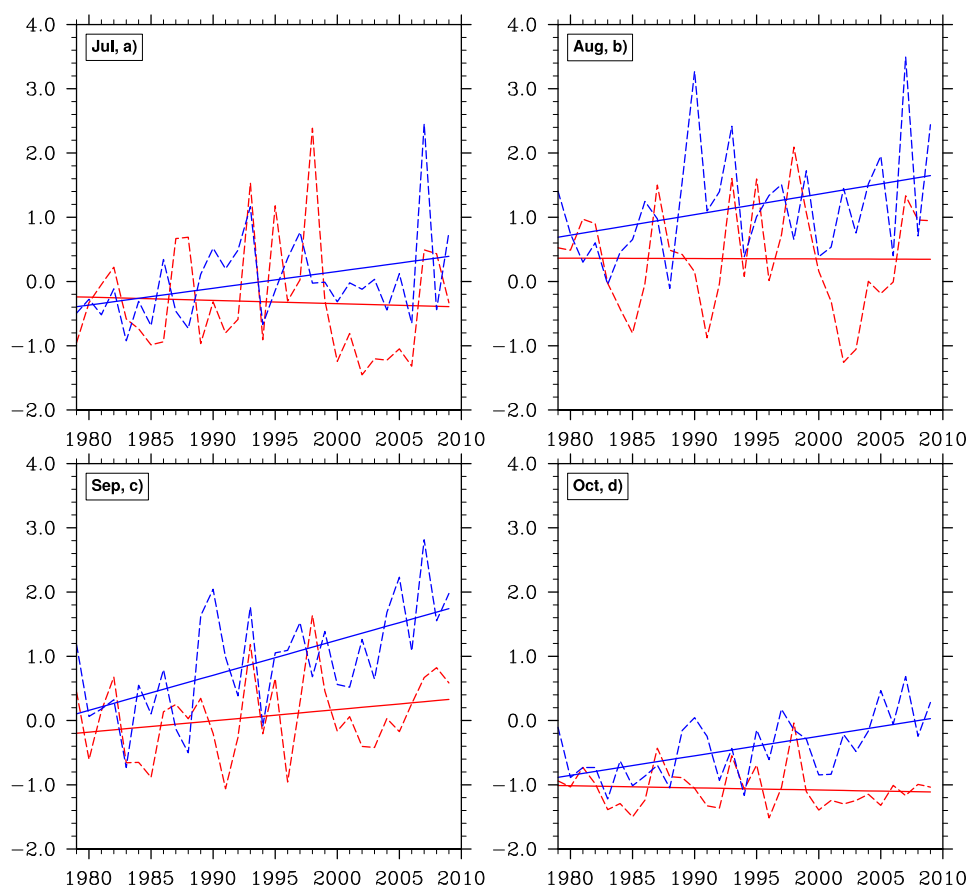


*Figure 58.* Monthly mean SST and its trends from 1979-2009 for the Chukchi Sea (blue), and the Beaufort Sea (red).